Finite Volume and Meshless Algorithms for Ideal Magnetohydrodynamics

A Thesis

submitted in partial fulfillment of the requirements

for the award of the degree

of

Doctor of Philosophy

by

Kalpajyoti Borah

Roll No : 11610314

Department of Mechanical Engineering

Indian Institute of Technology Guwahati

Guwahati - 39, Assam, India

August, 2017

To Ma and Dewta

Certificate

This is to certify that the work presented in the thesis entitled "**Finite Volume and Meshless Algorithms for Ideal Magnetohydrodynamics**" submitted by **Kalpajyoti Borah** to Indian Institute of Technology Guwahati for the award of the degree of **Doctor of Philosophy** in Mechanical Engineering is a bona fide record of research work carried out by the student himself under our supervision and have not been submitted elsewhere for any degree or diploma.

Signature: _____ Date:

Supervisor: Dr. Ganesh Natarajan
Department of Mechanical Engineering,
Indian Institute of Technology Guwahati,
Guwahati-781039, Assam, India.

Signature: _____ Date:

Supervisor: Prof. Anoop K. Dass
Department of Mechanical Engineering,
Indian Institute of Technology Guwahati,
Guwahati-781039, Assam, India.

Acknowledgements

Firstly, I would like to express my sincere gratitude to my supervisors Dr. Ganesh Natarajan and Prof. Anoop K. Dass. They have been tremendous mentors for me, not only in providing direction to scientific research but also giving real life lessons. Without their scientific insight, generous support, and constant motivation this work would not have been possible. I believe, it was a blessing to have them as my Ph.D. supervisors. I would also like to thank my doctoral committee members, Prof. Manmohan Pandey, Prof. Anugrah Singh, and Dr. Amaresh Dalal for serving as my committee members even at hardship. I thank them for their brilliant comments and suggestions. I would especially like to thank Dr. Amaresh Dalal for arranging financial support for the last two years. That was really helpful. I would also like to take this opportunity to thank all the faculty members of the institute who directly or indirectly helped me during my stay at IITG. My sincere thanks goes to all the support staffs of my department and IITG as a whole who have extended their help at difficult times. I would like to extend my gratitude to IITG administration for giving me the opportunity to carry out my research smoothly and arranging such a pleasant and comfortable stay for the last six years. My special thanks goes to my lab mates who helped me in coding, writing and most importantly for all those pleasant moments which will stay forever with me. It would be unfair if I don't mention about my hostel mates, without whom life would have really dull and frustrating. Thanks buddies!!

Now, the final words for the special people of my life. Words cannot express how grateful I am to *Ma* and *Dewta* for all of the sacrifices that they've made on my behalf. Their prayer for me was what sustained me this far. I would also like to express my sincere thanks to all other members of my family who have been standing by my side all through the journey, whether smooth or rough.

Kalpajyoti Borah

Abstract

This thesis is devoted to the development of numerical frameworks for ideal magnetohydrodynamics (MHD) based on the finite volume and meshfree approaches. The principal contribution is a new flux splitting scheme based on wave-particle behaviour for solving compressible ideal MHD equations in one and two dimensions. This scheme referred to as Magneto-acoustic Wave Particle Splitting (MWPS) scheme exploits the idea that while ideal MHD equations are non-convex with non-homogeneous fluxes as opposed to their hydrodynamic counterparts, they exhibit an overall wave-like structure. The proposed approach therefore splits the flux vector into three distinct parts: the particle-like transport part and the wave-like pressure and magnetic parts. The pressure part of the fluxes satisfy homogeneity property and the split flux Jacobians are constructed with a provision to regulate the numerical dissipation. The magnetic part of the fluxes however is non-homogeneous and is treated using a central scheme with artificial viscosity. This tripartite treatment of the total flux vector results in a scheme with a central-upwind like character and in one-dimension has been extended to second-order spatial accuracy through the solution-dependent weighted least-squares approach for gradient calculations. The use of solution-dependent weights incorporates the effects of limiting and results in a bounded and higher-order accurate flux scheme. Unlike the one-dimensional (1D) finite volume flow solver, the development of two-dimensional (2D) MHD code is fraught with two challenges. These are consequence of the additional equation for the x-component of the magnetic field in two-dimensions where there are eight conserved variables as opposed to seven in 1D MHD flows. Firstly, the MWPS scheme does not extend "naturally" from one to two dimensions, requiring the use of a further splitting of the magnetic flux vector with the split magnetic fluxes treated using a central scheme with artificial dissipation. Secondly, the multi-dimensionality requires that the solenoidality condition on the magnetic field $\nabla \cdot \mathbf{B} = 0$ be numerically enforced for physically consistent solutions. The latter issue has been dealt with using an approach analogous to the artificial compressibility method used to enforce the incompressibility constraint. Aptly known as Artificial Compressibility Analogy (ACA) approach, it employs an additional equation for a scalar potential whose solution allows the numerical divergence errors in the magnetic field to be radiated away. The equation for the scalar potential is clearly not a "physical" conservation law and is therefore solved using the Local Lax-Friedrichs scheme

(LLF) as opposed to the remaining equations which employs the MWPS scheme. The time-stepping is explicit with the divergence errors dictated by the residual convergence for steady-state MHD flows. However, for most MHD problems, which are inherently unsteady, a dual time-stepping approach is incorporated in order to ensure that the solenoidality constraint is satisfied at every physical timestep. A second-order accurate version of the MWPS scheme is also realised by employing a limited linear reconstruction scheme where the Green-Gauss reconstruction is used for gradients and Venkatakrishnan limiter enforces the monotonicity. The 1D finite volume solver is tested on several benchmark problems where the MWPS scheme is compared with other flux schemes. The numerical results show that while the MWPS scheme is at least as accurate as the AUSM (Advection Upstream Splitting Method) and even outperforms it in some scenarios. The MWPS scheme captures isolated discontinuities with acceptably low numerical diffusion while remaining stable, as opposed to the Central Rankine-Hugoniot (CRH) scheme which fails for problems with low pressures/densities despite exact resolution of isolated shocks and contacts. The numerical investigations with the 2D MWPS scheme also highlight the robustness and accuracy of the wave-particle splitting method. Importantly, we categorically demonstrate the need to numerically enforce the solenoidality constraint for magnetic field in multi-dimensions. It is shown that the use of sufficient number of sub-iterations in the dual-time-stepping framework leads to divergence errors which are acceptable and the use of fewer or no sub-iterations could lead to anomalous solutions that violate the flow physics. Several 2D problems including the Orszag-Tang vortex and cloud-shock interaction are simulated using the proposed flow solver both on structured and unstructured meshes. While the divergence errors are higher on unstructured grids as opposed to the structured counterparts, the MWPS scheme in conjunction with ACA is found to be a stable and reasonably accurate approach for multi-dimensional MHD simulations. The development of a 1D MHD solver in a meshfree framework is also explored in this thesis. The governing equations for ideal MHD in the strong form are solved on a cloud of points using the Upwind Least-Squares based Finite Difference (LSFD-U) method. The meshless and finite volume solvers are shown to be identical on a uniform point distribution with a symmetric neighbourhood of points. On non-uniform point distributions, the meshfree solver is found to result in inaccurate wave speeds and shock locations and the reasons as well as remedies for this issue are investigated. We outline a set of conditions defining a discretely conservative scheme and show that the meshless solvers, unlike their finite volume counterparts, do not satisfy the discrete conservation property, in general. A symmetric neighbourhood is shown to be necessary but not sufficient for effecting conservation at the discrete level. However, the use of geometric weights in the LSFD-U approach which are inverse-distances from the point to its neighbours along with neighbourhood symmetry is proved to satisfy the conditions for a conservative scheme. Numerical experiments on different MHD problems and arbitrary but representative point

distributions lend evidence in support of the arguments and result in a conservative meshfree solver for 1D ideal MHD. The developments, both on the finite volume and meshfree fronts, discussed in the thesis points to an indigenous, accurate and robust numerical framework for simulations of compressible ideal MHD flows.

Nomenclature

Symbols

$\mathbf{B}$	Magnetic Field
B_x	x-Component of Magnetic Field
B_y	y-Component of Magnetic Field
B_z	z-Component of Magnetic Field
c_a	Alfvenic Characteristic Speed
c_f	Fast Characteristic Speed
c_s	Slow Characteristic Speed
E	Total Energy
$\mathbf{I}$	Identity Matrix
$\mathbf{J}$	Current Density
M	Mach Number
M_a	Alfvenic-Mach Number
M_f	Fast-Mach Number
M_s	Slow-Mach Number
P	Thermal Pressure
P_t	Total Pressure
s	Entropy
$\mathbf{V}$	Velocity Field
V_{ref}	Reference Speed
ρ	Mass Density
σ	Electrical Conductivity
ν	Kinematic Viscosity

Abbreviations

ACA	Artificial Compressibility Analogy.
AFVS	Acoustic Flux Vector Splitting.
AUSM	Advection Upwind Split Method.
BC	Boundary Condition.
BDF	Backward Differencing Formula.
C	Contact Discontinuity.

CRH	Central Rankine-Hugoniot.
CT	Constrained Transport.
CUSP	Convective Upstream Split Pressure.
EFG	Element-Free Galerkin.
FLIP	Fluid-Implicit-Particle Method.
FR	Fast Rarefaction.
FS	Fast Shock.
FVM	Finite Volume Methods.
GLM	Generalized Lagrange Multiplier.
HDC	Hyperbolic Divergence Cleaning.
LBIE	Local Boundary Integral Equation.
LLF	Local Lax-Friedrichs.
LSFD-U	Least-Squares-based Upwind Finite Difference.
MHD	Magnetohydrodynamics.
MLPG	Meshless Local Petrov-Galerkin.
MPACT	Magnetic Potential Advection Constrained Transport.
MPCM	Meshless Point Collocation Method.
MWPS	Magneto-acoustic Wave Particle Splitting.
MWS	Meshfree Weak-Strong.
PDE	Partial Differential Equation.
PIC	Particle-in-cell.
RBF	Radial Basis Function.
RD	Rotational Discontinuity.
RJ	Ryu and Jones.
SDWLS	Solution-Dependent Weighted Least-Squares.
SM	Slow Compound Wave.
SPH	Smooth Particle Hydrodynamics.
SR	Slow Rarefaction.
SS	Slow Shock.
TVD	Total Variation Diminishing.
VK	Venkatakrishnan's.
WPS	Wave-Particle Splitting.

Contents

List of Figures

List of Tables

1

Introduction

Many natural and man-made phenomena are influenced by magnetic fields. Solar flares, coronal mass ejections (CMEs), preservation of the terrestrial magnetic field by fluid motion in the Earth's core and the formation of stars from interstellar clouds by the galactic magnetic field are some examples of significant yet complex natural phenomena involving magnetic fields. On the other hand, magnetic fields are commonly employed in industry to heat, pump, stir and levitate liquid metals. The branch of science that deals in the study of flow of electrically conducting fluids interacting with magnetic fields is known as magnetohydrodynamics or MHD in short. In general, MHD finds its application in the fields of astrophysics, aerospace technology, geology, geophysics and medicine.

The mutual interaction of a magnetic field $\mathbf{B}$ and a velocity field $\mathbf{V}$ is a highly nonlinear activity. As the conducting particles move, they create local space charge concentrations and thus produce electric fields. Their motion can also generate electric currents and in turn induce magnetic fields. The induced magnetic field affects the motion of the particles by changing the velocity field. The physics governing this complex situation can be studied by the laws of Faraday and Ampere, and by the Lorentz force experienced by the current-carrying body. According to Faraday's law of induction, the relative movement of a conducting fluid and a magnetic field causes an electro motive force (e.m.f.) of order $|\mathbf{V} \times \mathbf{B}|$. This will give rise to electrical currents with the current density $\mathbf{J} = \sigma(\mathbf{V} \times \mathbf{B})$, where σ is the electrical conductivity. These induced currents produce the induced magnetic field in accordance with Ampere's law. The combined magnetic field (imposed and induced) interacts with the induced current density $\mathbf{J}$ to generate a Lorentz force (per unit volume) equal to $\mathbf{J} \times \mathbf{B}$. This acts on the conducting fluid and is generally directed so as to resist the relative movement between the magnetic field and the fluid. The fluid can "drag" the magnetic field lines and the magnetic field can pull the conducting fluid. This partial "freezing together" of the medium and the magnetic field is a prominent feature in MHD flows.

1.1 A brief history of MHD

MHD was not considered a fully fledged subject before the twentieth century, although the laws of magnetism and fluid flow were already known. Only a few isolated experiments were carried out by the nineteenth century physicists to answer some natural MHD phenomena. However, the subject did not grow further in the nineteenth century probably due to the fact that the many commonly used fluids were not very good conductors of electricity. Things started to change only in the late 1930s or early 1940s when astrophysicists realised the existence of magnetic fields and plasma throughout the universe. The most significant event in MHD was the discovery of the Alfvén waves by engineer-astrophysicist Hannes Alfvén in 1942. It was due to Alfvén that MHD became a fully-fledged subject and the term 'magnetohydrodynamics' came into existence. Alfvén waves are transverse inertial waves that can be transmitted by the magnetic field lines that are under the electromagnetic forces opposing the relative motion of the fluid and the field, and have the inertia of the fluid frozen to them. Around the same time, geophysicists began to investigate the Earth's magnetic field which is generated by dynamo action within the liquid-metal of its core, an hypothesis introduced in 1919 by Larmor in the context of the sun's magnetic field. A period of intense research followed afterwards in the fields of solar magnetic activity, planetary magnetospheres, stellar winds, interstellar medium, accretion disks of compact objects and more. Plasma physicists, on the other hand, acquired interest in MHD after the second World War as they studied the stability, or lack of stability of plasma confined by magnetic fields in controlled thermonuclear fusion.

The application of MHD in engineering was relatively slow and did not really get going until the 1960s. However, there were some early pioneering works such as the invention of the electromagnetic pump by Hartmann in 1918 and invention of the MHD generator by Petersen in 1919. Despite these early works, it was only in the early 1960s that MHD was begun to be exploited in engineering. The quest for the change came as a result of the interests related to acquiring nuclear technology in the cold war period. Magnetic fields were used in pumping liquid sodium in fast-breeder reactors and confining hot plasma away from material surfaces in controlled thermonuclear fusion. Another important innovation, although failed, was MHD power generation in which ionised gas was propelled through a magnetic field. Gradually, the interest in MHD applications shifted from power generation to metallurgy. Two decades later, it has become a common practice to use magnetic fields to heat, pump, stir and levitate liquid metals in the metallurgical industries. As of today, MHD finds place in a vast range of applications spanning aerospace to medical industry.

1.2 Literature review on MHD

The vast range of different engineering applications based on MHD motivate the understanding of complex flow phenomena in a quest for continued improvement. However, it is not possible to conduct experiments in many cases (such as astrophysical applications) and theoretical approaches are difficult owing to the highly non-linear system of vector conservation laws. Clearly, the increase in computing power means that numerical approaches are the only viable means to uncover the complex flow physics in MHD problems and several numerical frameworks have been developed for MHD simulations. The present work is mainly concerned with the development of numerical algorithms and their application to ideal compressible MHD flows. We therefore carry out a comprehensive survey of the state-of-art in numerical methods for compressible ideal MHD focussing on various developments and challenges.

1.2.1 Numerical schemes for MHD and challenges

The numerical simulation of MHD flows assumes significance in the light of its potential applications and has been the subject of several investigations in the past. While it may appear that compressible MHD simulations are a mere extension of ideas involved in simulating the compressible Euler equations for hydrodynamics by accounting for the magnetic field, the mathematical nature of the equations and the underlying physics pose a greater challenge. The primary difference between MHD flows and their hydrodynamic counterparts physically arises in the existence of a magnetic field-velocity field coupling in the former, with the Lorentz force appearing as an additional term in the momentum equation thereby influencing the velocity field. A striking difference between the two flows, even in one-dimension, is the complex wave-structure in MHD. While one observes only shocks, contacts and expansions in Euler hydrodynamics, MHD flows allow for several additional flow features such as switch-on and switch-off shocks, tangential and rotational discontinuities as well as compound waves. From a mathematical perspective, while the one-dimensional (1D) Euler equations admit two acoustic waves and one entropy wave (corresponding to three real eigenvalues), MHD equations allow for seven distinct waves which consist of slow and fast magnetosonic waves, Alfvén waves and entropy wave which can be related to the seven distinct wave speeds. Put differently, the role that acoustic speed plays in hydrodynamics is replaced by fast and slow magnetosonic wave speeds as well as the Alfvén wave speed in MHD, all of which depend on the magnitude of the magnetic field. From a numerical viewpoint, Euler and MHD equations are both hyperbolic systems but the latter does not share the convexity and homogeneity property of the Euler fluxes. The lack of convexity manifests in the presence of compound waves in the solutions to MHD problems, while the absence of homogeneity makes it difficult to envisage MHD analogues of hydrodynamic flux-splitting schemes such as

Steger-Warming scheme and the Roe scheme. Clearly, the mathematical nature of the MHD equations have a profound influence on the solution spectrum with the attendant difficulties in devising numerical flux schemes.

Despite the differences highlighted earlier, most of the flux formulations developed for MHD flows draw heavily from those developed for Euler hydrodynamics. The first significant effort was made by Brio and Wu [5], who developed an approximate Roe-like solver for MHD under the condition that the ratio of specific heats was equal to 2. Subsequently, more generic approximate Riemann solvers were developed by several other researchers such as Zachary and Colella [6], Dai and Woodward [7], Ryu and Jones [8], Roe and Balsara [9], Cargo and Gallice [10] and Balsara [11]. Roe solvers based on the eigen-structure and calculation of the right eigenvectors of the Jacobian matrix is a tedious effort on the numerical front. There have also been efforts to develop inexpensive approximate Riemann solvers, notably of the Harten-Lax-van Leer class. Honkkila and Janhunen [12] developed a HLLC scheme for ideal relativistic MHD, Gurski [13] devised an accurate extension of the HLLC solver for Euler equations for MHD and a different variant of the HLLC for MHD was investigated by Li in [14]. These HLLC solvers however could not exactly resolve isolated discontinuities which was made possible by the efforts of Miyoshi and Kusano [2] who constructed a multi-state HLL solver for ideal MHD. There have also been extensive efforts to implement genuinely multidimensional MHD Riemann solvers, most notably the works of Balsara [15–18]. Interestingly, the flux-vector splitting schemes for Euler equations are more difficult to adapt to MHD, precisely due to the lack of flux homogeneity in MHD flows. A very recent study by Balsara and co-workers [19] has analyzed the strengths and weaknesses of different flux vector splitting schemes for ideal MHD equations.

A different class of approaches in hydrodynamics that attracted immense interest in the nineties was the wave-particle splitting techniques. These methods, which choose to split the flux vector into wave-like and particle-like contributions were found to be quite robust, with the accuracy dependent on the choice of splitting. Among the schemes that belong to this class, some of the notable ones include Advection Upstream Splitting Method (AUSM) and its variants [20], Zha-Bilgen scheme [21], Wave-Particle Splitting scheme (WPS) [22], Convective Upstream Split Pressure (CUSP) [23] scheme and the Acoustic Flux Vector Splitting (AFVS) scheme [24]. The attractive feature common to this class of schemes was that they did not involve any knowledge or use of the eigenvalues and eigenvectors of the Jacobian matrix and were easily amenable to extension and implementation for MHD flows. Agarwal et al. [25] examined the AUSM and WPS schemes for the Brio-Wu shock tube problem and concluded that the performance of the schemes were comparable in 1D MHD. Han and co-workers [26] proposed a AUSM-MHD scheme based on AUSMPW+ and M-AUSMPW+ methods by combining them with multidimensional limiting to achieve higher order accuracy.

Their work was an improvement upon the approach by Kim et al. [27], with the pressure-based weight functions modified in order to account for the magnetic pressure. A pressure-based method for MHD flows using AUSM flux formulae was devised and investigated in [3] for 2D complex MHD interactions. Shen et al. [28] developed an E-CUSP scheme for MHD system and demonstrated its efficacy for a range of 1D and 2D MHD problems employing a WENO reconstruction for higher-order accuracy.

Another class of schemes that have received attention, particularly for Euler flows, is the central-upwind schemes [29] that lead to quite simple flux formulae which require some amount of added dissipation for stability. Susanto and co-workers [30] have attempted the development of a high-order central ENO scheme for MHD flows with adaptive refinement. Their results indicate that adaptive time-dependent simulations with their proposed scheme is capable of resolving the small-scale features to unprecedented resolution while remaining stable. Jaisankar and Rao [31] have also proposed a second-order accurate central Rankine-Hugoniot solver (CRH) for hyperbolic systems and have shown that their scheme is robust and accurate for benchmark 1D and 2D MHD problems.

One of the major challenges in developing a numerical scheme for compressible MHD is satisfying the divergence-free constraint for the magnetic field, $\nabla \cdot \mathbf{B} = 0$ at all time steps in unsteady numerical simulations. While the constraint gets trivially satisfied in 1D where B_x is assumed constant and no variations in y- and z-directions exist, the problem becomes non-trivial in higher dimensions. A lack of satisfaction of this constraint in multi-dimensional MHD simulations leads to growth of truncation errors corresponding to $\nabla \cdot \mathbf{B}$ term with time evolution and consequently produces non-physical solutions. Several methods have been proposed to counter the growth of these errors and satisfy the solenoidality constraint. The classical projection scheme [32] where the magnetic field is projected to a space in which the solenoidality constraint is satisfied and the constrained transport method [33] where a staggered mesh is utilised are two of the earlier approaches in this direction. The eight-wave source term method developed by Powell [34] attempts to enforce the constraint by modifying the hyperbolic system into a non-conservative system by adding source terms that are proportional to $\nabla \cdot \mathbf{B}$ in the momentum, energy and induction equations. The Hyperbolic Divergence Cleaning (HDC) [35] method was introduced by Dedner et al. where a generalized Lagrange multiplier is used to couple the solenoidality constraint with the ideal MHD equations by means of introducing an additional equation. Yalim et al. [1] developed a variant of the HDC approach which is analogous to Chorin's artificial compressibility approach [36] for incompressible flows. The issue of numerically enforcing the solenoidality constraint is critical for robust and physically consistent multi-dimensional MHD simulations and shall be discussed in greater detail in Chapter 2.

1.2.2 *Meshfree frameworks for MHD*

Although application of meshfree methods for solving different hydrodynamical problems is not uncommon, research works using meshless methods for solving MHD flow problems have been very limited. In typical meshfree approaches, the domain is represented by a cloud of points and discrete operators are defined employing this point distribution. Though the use of arbitrary point distributions may increase the computational effort compared to the routine structured mesh calculations, the ever-increasing speed of the computers has made these techniques promising. Among different meshfree methods, Brackbill [37] extended the fluid-implicit-particle (FLIP) method to MHD and solved high magnetic Reynold's number flow problems. Jiang et al. [38] have used smoothed particle hydrodynamics (SPH) for MHD simulations and studied flows subjected to a streamwise magnetic field during transition to turbulence. Element-Free Galerkin (EFG) method was also used by several authors [39, 40] for solving MHD flow problems. Verardi et al. [39] proposed an interpolatory formulation for moving least-squares approximations which allows direct introduction of boundary conditions, whereas Bhargava and Singh [40] used this approach to investigate unsteady MHD flow and heat transfer of non-Newtonian fluids. Bourantas et al. [41] used the meshless point collocation method (MPCM) to solve MHD flows in channels with fully or partially insulating and partially conducting walls having arbitrary cross-sections. Dehghan and Mirzaei employed the local boundary integral equation (LBIE) meshless method [42] and the meshless local Petrov-Galerkin (MLPG) method [43] to obtain numerical solutions for unsteady MHD flows through pipes with different cross sections and arbitrary wall conductivity. Recently, Deghan and Salehi [44] used a meshfree weak-strong (MWS) form technique based on a combined collocation and MLPG method to solve unsteady flow through a pipe with arbitrary wall conductivity. One of the striking drawbacks of meshfree methods is that they lack conservation at the discrete level. Most importantly, non-conservation may lead to inaccurate wave speeds in compressible flows. Considering the severity of the issue, it is surprising that the issue has not received the attention it deserves. The most notable work in this direction was carried out by Chiu et al. [45] where they analysed the conditions for a meshfree method to be discretely conservative and discussed a novel conservative meshfree approach through careful construction of a discrete derivative operator. More recently, a flux-conserving meshfree finite difference approach was proposed by Suchde et al. [46] by combining ideas of Delaunay tessellation and moving least-squares method. This method was investigated on typical convective-diffusive equations and incompressible Navier-Stokes equations and showed improved mass preservation at the discrete level. However, neither Suchde's approach [46] nor Chiu's methodology [45] have been employed for MHD flows.

1.2.3 Numerical Codes for MHD

Unlike traditional fields in fluid mechanics, compressible MHD is arguably a highly specialised field of study and there have only been far fewer numerical efforts to tackle specific problems of interest in this area. We review briefly some of the well-known numerical codes for compressible MHD in this section. Among the earliest notable efforts is the ZEUS code developed by Stone and co-workers [47, 48]. It is a multi-dimensional flow solver that employs a flux splitting scheme and higher-order upwinding in conjunction with artificial viscosity for shock capturing. It utilises the idea of operator-split methods and solves the system of equations in non-conservation form. In order to equip the MHD solvers with adaptive refinement, Stone and co-workers devised a new solver named ATHENA [49] based on directionally unsplit, higher-order Godunov methods. The constrained transport (CT) technique is used to enforce the divergence-free constraint of the magnetic field and discretisation is based on cell-centered volume-averages for mass, momentum, and energy, and face-centered area-averages for the magnetic field. These codes have been widely used by the astrophysics community to study natural flow problems like accretion disks, interstellar shocks and MHD turbulence in molecular clouds. Another important contribution towards MHD solvers is the RIEMANN code due to Balsara [50], which is based on a monotonicity preserving weighted essentially non-oscillatory (MPWENO) scheme. This code has been applied to problems such as simulations of turbulence in interstellar medium (ISM) driven by supernova explosion, physics of accretion disk boundary layers, star formation and planet formation studies. Yet another significant contribution is the COOLFluid (Computational Object Oriented Library for Fluid Dynamics) code [51, 52], which is a state-of-the-art C++ framework for multi-physics simulations on unstructured grids. Some of the other efforts in developing in-house solvers for MHD include AMRVAC [53], BATS-R-US [54], Nirvana [55], and CERANS [56, 57]. The numerical code CERANS (Compressible Euler/Reynolds Averaged Navier-Stokes) solver is a general-purpose CFD code developed at DRDL, Hyderabad, India for solving the RANS equations in cell-centered finite volume framework on sequential and parallel computers. The code can handle flow regimes from low subsonic to hypersonic Mach numbers and can tackle complex geometries involving both structured and unstructured meshes. This code has been extended to study MHD flows and referred to as CERANS-MHD code, which is devised with AUSM-PW+ flux splitting scheme and artificial compressibility analogy approach and Powell's source term method to satisfy the divergence-free magnetic field constraint. It has been mainly utilised in MHD flow control such as mitigation of shock-induced flow separation and heat transfer for a blunt body in hypersonic flow [58, 59]. To the best of the author's knowledge, CERANS-MHD is the only indigenous multi-

dimensional numerical code for ideal MHD in the country and the present work must be viewed as a modest effort towards developing a robust and accurate in-house numerical framework in this direction.

1.3 Objectives of the thesis

The broad objective of this thesis is the the development of a simple, robust, accurate and computationally efficient framework for numerical computations of ideal MHD flows. Inspired by the AFVS scheme which employs an unique physics-based splitting approach for Euler hydrodynamics, we explore the possibility of devising a new robust and accurate flux scheme for MHD flows in one and two dimensions. This scheme is then employed in conjunction with an unstructured finite volume framework to develop a numerical solver for MHD flows. Preliminary studies on a meshless framework for MHD problems are also carried out with an emphasis on the need and means for enforcing discrete conservation on arbitrary point distributions. The specific aims of this thesis may be summarised as follows.

1. Development of a new wave-particle splitting scheme based on the AFVS philosophy for MHD flows, referred to as the Magneto-acoustic Wave Particle Splitting (MWPS) scheme.

2. Investigating diffusion-regulation mechanisms inherent in the MWPS scheme and extending the MWPS scheme to high-order accuracy. The latter is achieved by using the idea of limited linear reconstruction and for 1D ideal MHD, we make use of the Solution Dependent Weighted Least Squares (SDWLS) approach to obtain a second-order accurate MWPS scheme.

3. Development of a two-dimensional MHD solver based on the MWPS scheme with specific emphasis on enforcing the solenoidality criterion. It is shown that the extension of 1D MWPS to 2D is not relatively straightforward and that neglecting the solenoidality constraint could lead to anomalous solutions. We employ the artificial compressibility analogy (ACA) approach in conjunction with dual time-stepping to minimise magnetic divergence errors on structured and unstructured meshes.

4. Investigating the meshfree LSFD-U framework for MHD flows. While the LSFD-U method was originally studied for Euler and Navier-Stokes equations in compressible aerodynamics, we attempt to extend this framework to 1D ideal MHD. We focus on the importance of discrete conservation and the role of weights in the least-squares approach and the choice of neighbourhood in achieving a conservative scheme and physically consistent solutions.

The finite volume MHD solver in one and two dimensions are extensively validated using several benchmark problems of varying levels of complexity. Comparative studies of MWPS with flux schemes on several canonical problems are carried out with the 1D solver and the 2D solver with MWPS scheme has been employed on both structured and unstructured meshes for complex and genuinely two-dimensional MHD problems. The meshfree solver for MHD, while limited to 1D, is also tested on select canonical problems and highlights the importance of weighted least-squares approach on discrete conservation. The numerical experiments provide solid evidence that the proposed MWPS scheme, in conjunction with the ACA approach in multi-dimensions, leads to a numerical flow solver which is robust, accurate and versatile in predicting complex MHD flow phenomena.

1.4 Outline of the thesis

The governing compressible ideal MHD equations along with waves and discontinuities associated with the system are presented in Chapter 2. The significance of enforcing the solenoidality constraint and means to achieve this in a numerical framework are also discussed. The details of the development of the proposed MWPS scheme for 1D ideal MHD is presented in Chapter 3. Extension of the scheme to higher-order accuracy and the dissipation regulation mechanisms are also discussed. The performance of the proposed scheme in a finite-volume framework for 1D MHD problems including isolated discontinuities are investigated in this chapter. Comparisons are made with reference solutions and AUSM scheme to highlight the advantages/limitations of the proposed scheme. The extension of MWPS scheme to two-dimensions is the focus of Chapter 4, where the differences in treatment of the magnetic flux vector and limited linear reconstruction for second-order spatial accuracy are detailed. The specific implementation of divergence cleaning approaches for numerically enforcing the solenoidality constraint is described and several MHD test cases are simulated to assess the performance of the MWPS scheme and the divergence cleaning approach. Chapter 5 gives an overview of the meshfree LSFD-U framework and discusses the issue of discrete conservation, in the MHD context, and the role of neighbourhood stencil and geometric weights in achieving conservation. Canonical 1D test problems are solved on non-uniform point distributions to demonstrate how discrete conservation may be realised and why it is indeed important. We conclude the thesis by summarizing the salient contributions and giving some future directions in Chapter 6. Supplementary information are provided in Appendices A.1-A.7, including a sample MATHEMATICA script for interested readers.

2

Mathematical preliminaries and governing equations

In this chapter, the governing equations of compressible ideal MHD and different types of waves associated with the system are presented. A number of complex discontinuities in addition to shocks, contacts and expansion fans are found corresponding to some typical waves in MHD and their interactions. The possible discontinuities arising in MHD flows are discussed in some detail. One of the major challenges in numerical simulations of MHD flows is controlling the growth of truncation errors corresponding to $\nabla \cdot \mathbf{B}$ term over the evolution of the flow. Measures available in the literature to deal with this issue are also reviewed.

2.1 Ideal MHD equations

The MHD equations combine the equations of fluid dynamics (Euler equations, in the present study) with the Maxwell's equations of electrodynamics. The ideal MHD equations given below are obtained by neglecting displacement current, electrostatic forces, effects of viscosity, electrical resistivity and heat conduction [60].

$$\frac{\partial \rho}{\partial t} + \nabla \cdot (\rho \mathbf{V}) = 0 \tag{2.1}$$

$$\frac{\partial (\rho \mathbf{V})}{\partial t} + \nabla \cdot (\rho \mathbf{V}\mathbf{V} + \mathbf{I}P_t - \mathbf{B}\mathbf{B}) = 0 \tag{2.2}$$

$$\frac{\partial \mathbf{B}}{\partial t} + \nabla \cdot (\mathbf{V}\mathbf{B} - \mathbf{B}\mathbf{V}) = 0 \tag{2.3}$$

$$\frac{\partial E}{\partial t} + \nabla \cdot \big((E + P_t)\mathbf{V} - \mathbf{B}(\mathbf{B} \cdot \mathbf{V})\big) = 0 \tag{2.4}$$

$$\nabla \cdot \mathbf{B} = 0 \tag{2.5}$$

The induction equation Eq. (2.3) implies the solenoidality constraint if a divergence-free magnetic field is imposed initially. Eqs. (2.1-2.4) together with Eq. (2.5) present the conservative form of compressible ideal MHD equations. In the above equations ρ denotes density, $\mathbf{V}$ the velocity field, $\mathbf{B}$ the magnetic field, P_t the total pressure, and E denotes the total energy. The total pressure and energy are defined by

$$P_t = P + \frac{1}{2}B^2 \tag{2.6}$$

$$E = \frac{P}{(\gamma - 1)} + \frac{1}{2}\rho V^2 + \frac{1}{2}B^2 \tag{2.7}$$

where,

$$V^2 = u^2 + v^2 + w^2 \tag{2.8}$$

$$B^2 = B_x^2 + B_y^2 + B_z^2 \tag{2.9}$$

Here, P denotes the thermal pressure, u, v, and w are the three components of the velocity field $\mathbf{V}$, and B_x, B_y and B_z represent the components of the magnetic field $\mathbf{B}$. The above system of equations is non-strictly hyperbolic in nature since its Jacobian has real but non-distinct eigenvalues and a complete set of right eigenvectors. Unlike the system of hydrodynamic equations, which they reduce to in the case of $\mathbf{B} = 0$, this system is non-convex due to fields which cannot be characterised as either linearly degenerate or genuinely nonlinear [5]. The Eqs. (2.1-2.4) can be cast in the vector conservation form as given below.

$$\frac{\partial}{\partial t}\begin{pmatrix} \rho \\ \rho\mathbf{V} \\ \mathbf{B} \\ E \end{pmatrix} + \nabla \cdot \begin{pmatrix} \rho\mathbf{V} \\ \rho\mathbf{V}\mathbf{V} + \mathbf{I}P_t - \mathbf{B}\mathbf{B} \\ \mathbf{V}\mathbf{B} - \mathbf{B}\mathbf{V} \\ (E + P_t)\mathbf{V} - \mathbf{B}(\mathbf{B}\cdot\mathbf{V}) \end{pmatrix} = 0 \tag{2.10}$$

The equations for 2D MHD can be easily obtained from Eq. (2.10) by retaining the changes only with respect to x, y and t. The resulting equations in the conservative form can be written as,

$$\frac{\partial \mathbf{U}}{\partial t} + \frac{\partial \mathbf{F}}{\partial x} + \frac{\partial \mathbf{G}}{\partial y} = 0 \tag{2.11}$$

where the vector of conservative variables $\mathbf{U}$, and the flux vectors $\mathbf{F}$ and $\mathbf{G}$ in x- and y-directions, respectively are written as

$$\mathbf{U} = \begin{bmatrix} \rho \\ \rho u \\ \rho v \\ \rho w \\ B_x \\ B_y \\ B_z \\ E \end{bmatrix}, \qquad \mathbf{F} = \begin{bmatrix} \rho u \\ P + \rho u^2 + \frac{1}{2}B^2 - B_x^2 \\ \rho uv - B_x B_y \\ \rho uw - B_x B_z \\ 0 \\ uB_y - vB_x \\ uB_z - wB_x \\ (E + P + \frac{1}{2}B^2)u - B_x(uB_x + vB_y + wB_z) \end{bmatrix}, \tag{2.12}$$

$$\mathbf{G} = \begin{bmatrix} \rho v \\ \rho uv - B_x B_y \\ P + \rho v^2 + \frac{1}{2}B^2 - B_y^2 \\ \rho vw - B_y B_z \\ vB_x - uB_y \\ 0 \\ vB_z - wB_y \\ (E + P + \frac{1}{2}B^2)v - B_y(uB_x + vB_y + wB_z) \end{bmatrix}.$$

It must be emphasised that the governing equations for 2D flows contain the z-component of momentum and magnetic field which are non-zero in general. This is because 2D flows are defined as those in which the flux derivatives are prominent only in two directions, which are chosen herein as the x and y directions. Consequently, the equations corresponding to the z-component of magnetic field and momentum are retained, although there are no flux derivatives in the z-direction. This explanation applies to 1D MHD flows as well where the resulting conservation laws may be written in a compact form as,

$$\frac{\partial \mathbf{U}}{\partial t} + \frac{\partial \mathbf{F}}{\partial x} = 0 \tag{2.13}$$

where the vector of conservative variables $\mathbf{U}$ and the flux vector $\mathbf{F}$ in x-direction are as given in Eq. (2.12).

2.2 Waves in 1D ideal MHD

As mentioned in the previous section, the ideal MHD equations are more complex than the Euler equations. This is due to the existence of a number of complex waves and their interactions in the MHD system. These waves can be divided into four families, namely entropy waves, Alfvén waves, and fast and slow magnetoacoustic waves.

Entropy waves neither propagate nor involve any mass flow, but initiate a change in the entropy (or density and internal energy). All other properties including magnetic field remain continuous across an entropy wave. There is one entropy wave in the ideal MHD system. Alfvén waves are driven by the magnetic tension force. They are transverse and incompressible and therefore there is no perturbations in density and pressure. There are two Alfvén waves in ideal MHD system. Fast and slow magnetoacoustic waves are compressible waves. They are driven by both magnetic tension and pressure forces. There are two fast and two slow magnetoacoustic waves in the ideal MHD system.

Mathematically, the ideal MHD system is non-strictly hyperbolic since the Jacobian matrix of the system has real but non-distinct eigenvalues. Each eigenvalue is associated with a wave that travels at the characteristic speed. The seven eigenvalues for 1D case in non-decreasing order are

$$\begin{aligned} \lambda_1 &= u - c_f \\ \lambda_2 &= u - c_a \\ \lambda_3 &= u - c_s \\ \lambda_4 &= u \\ \lambda_5 &= u + c_s \\ \lambda_6 &= u + c_a \\ \lambda_7 &= u + c_f \end{aligned} \tag{2.14}$$

The quantities λ_i $(i = 1, 2, ..., 7)$ represent the seven speeds at which the information is propagated locally by the four wave families as mentioned above. Thus λ_4 is associated with the entropy wave, λ_1 and λ_7 are associated with fast magnetoacoustic waves, λ_2 and λ_6 are associated with Alfvén waves and, λ_3 and λ_5 are related to slow magnetoacoustic waves. In the above equations c_f, c_a and c_s are the fast, Alfvén and slow characteristic speeds respectively which are expressed as,

$$c_a = \sqrt{\frac{B_x^2}{\rho}} \tag{2.15}$$

$$c_f = \left[\frac{1}{2} \left\{ a^2 + \frac{B_x^2 + B_y^2 + B_z^2}{\rho} + \sqrt{\left(a^2 + \frac{B_x^2 + B_y^2 + B_z^2}{\rho} \right)^2 - 4a^2 \frac{B_x^2}{\rho}} \right\} \right]^{1/2} \tag{2.16}$$

$$c_s = \left[\frac{1}{2} \left\{ a^2 + \frac{B_x^2 + B_y^2 + B_z^2}{\rho} - \sqrt{\left(a^2 + \frac{B_x^2 + B_y^2 + B_z^2}{\rho} \right)^2 - 4a^2 \frac{B_x^2}{\rho}} \right\} \right]^{1/2} \tag{2.17}$$

where a is the acoustic speed given by

$$a = \sqrt{\frac{\gamma P}{\rho}} \tag{2.18}$$

The non-distinctness of eigenvalues can be explained by citing the following two instances.

(1) If $B_x = 0$, $c_s = c_a = 0$, thus $\lambda_2 = \lambda_3 = \lambda_4 = \lambda_5 = \lambda_6 = u$.

(2) If $B_y^2 + B_z^2 = 0$, $c_f^2 = \max(a^2, c_a^2)$ and $c_s^2 = \min(a^2, c_a^2)$. Therefore, when $a^2 \neq c_a^2$, either $c_f^2 = c_a^2$ implying $\lambda_1 = \lambda_2$ and $\lambda_7 = \lambda_6$ or, $c_s^2 = c_a^2$ implying $\lambda_3 = \lambda_2$ and $\lambda_5 = \lambda_6$. When $a^2 = c_a^2$, $c_f^2 = c_s^2 = c_a^2$, thus $\lambda_1 = \lambda_2 = \lambda_3$ and $\lambda_5 = \lambda_6 = \lambda_7$.

2.3 Flow features in ideal MHD

Discontinuities in ideal MHD can be divided mainly into three categories: shocks, contacts and rotational discontinuities. Let us suppose that x-axis and y-axis are normal and parallel to the surface of the discontinuity, respectively. A general property of MHD is that the normal component of the magnetic field B_x remains continuous across a discontinuity. In case of a shock, entropy $s = P/\rho^\gamma$ increases with a possible transfer of mass across the surface. Across contacts entropy jumps, but there is no mass flow. Entropy remains constant across a rotational discontinuity although mass flow can occur.

Shocks can be further subdivided into three categories: fast, slow and intermediate shocks. To understand the properties of these shocks we refer to the Figure 2.1 as shown in [61], where four plasma states are defined based on increasing entropy. State 1 (S1) has the lowest entropy and is referred to as superfast state. In a frame moving with the shock, the normal plasma velocity $u^1 > c_f^1$ and the normal fast-Mach number $M_f^1 = u^1/c_f^1$, the Alfvénic-Mach number $M_a^1 = u^1/c_a^1$ and the slow-Mach number $M_s^1 = u^1/c_s^1$ are all greater than unity. Note that here the superscripts are used to represent the states. State 2 (S2) is referred to as super-Alfvénic (it is also subfast and superslow) since $c_f^2 > u^2 > c_a^2, c_s^2$ and $M_f^2 < 1$ but $M_a^2, M_s^2 > 1$. State 3 (S3) is superslow (also subfast and sub-Alfvénic) as $c_f^3, c_a^3 > u^3 > c_s^3$ and $M_f^3, M_a^3 < 1$ but $M_s^3 > 1$. And finally State 4 (S4) is denoted as subslow (also subfast and sub-Alfvénic) since $c_f^4, c_a^4, c_s^4 > u^4$ and $M_f^4, M_a^4, M_s^4 < 1$. It is clear from the above discussion that there are six possible entropy satisfying shock transitions, noted as S1→S2, S1→S3, S1→S4, S2→S3, S2→S4 and S3→S4. The definitions of different kinds of shocks are based on

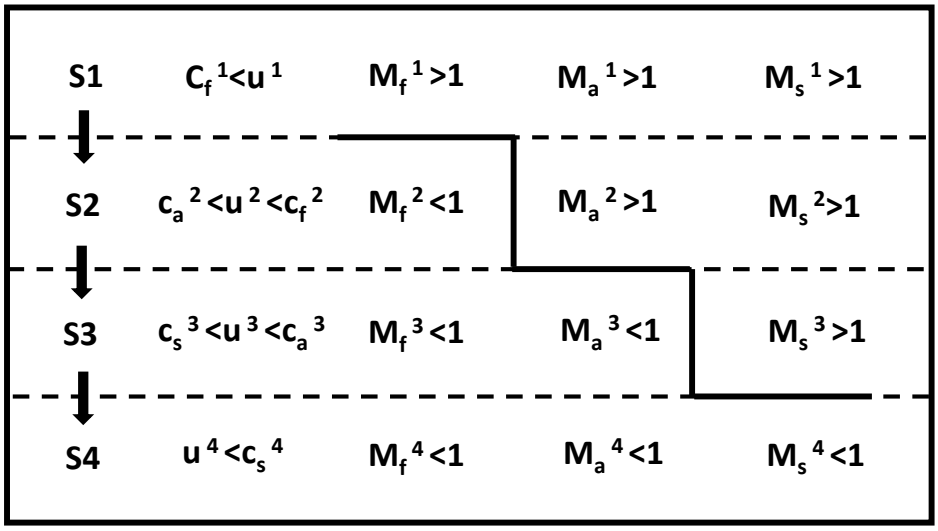

Figure 2.1. Possible states (represented by the superscripts) that can be connected through a MHD shock

these transitions of states and are explained below.

Fast shock (S1→S2): The plasma is superfast upstream and subfast (but super-Alfvénic) downstream. A fast shock increases B_y such that magnetic field lines are refracted away from the shock normal.

Slow shock (S3→S4): The plasma is superslow upstream and subslow downstream. A slow shock decreases B_y such that magnetic field lines are refracted towards the shock normal.

Intermediate shocks (S1→S3, S1→S4, S2→S3 and S2→S4): The plasma is super-Alfvénic upstream and sub-Alfvénic downstream. An intermediate shock changes the sign of B_y such that magnetic field lines are flipped over the shock normal.

Some of the limiting cases of the shock types mentioned above are also available. These are discussed below.

Switch-on fast shock (S1→(S2=S3)): It is a limiting case of a fast shock in which the upstream tangential magnetic field component B_y is zero, whereas the same component in the downstream of the shock is nonzero. The downstream normal Alfvénic-Mach number M_a becomes equal to one. Two conditions have

to be satisfied in the upstream flow for a fast switch-on shock to occur:

$$\beta < \frac{2}{\gamma}$$

$$1 < M_a < \sqrt{\frac{\gamma(1-\beta)+1}{\gamma-1}}$$

where $\beta = 2P/B^2$ is the ratio between the thermal pressure and the magnetic pressure.

Switch-off slow shock ((S2=S3)→S4): It is a limiting case of a slow shock where the tangential magnetic field B_y is nonzero upstream but becomes zero downstream. For this type of shocks the upstream normal Alfvénic-Mach number M_a is exactly equal to one.

Hydrodynamic (parallel) shock (S1→S4): It is a limiting case of an intermediate shock where the magnetic field does not change across the shock. The value of B_y both upstream and downstream of the shock are identically zero.

Apart from shocks, one also encounters other types of discontinuities like contact, tangential and rotational discontinuities. In addition, it is also possible to find rarefaction waves and a typical wave known as compound wave in MHD. The characteristics of these discontinuities and waves are explained below.

Contact discontinuity: It occurs only when the normal component of the magnetic field B_x is nonzero. Density and entropy jump across a contact while all other quantities remain continuous.

Tangential discontinuity: If the normal component of the velocity field u and the magnetic field B_x are zero, then the discontinuity is referred to as tangential discontinuity. Density ρ, thermal pressure P, tangential velocity v and tangential magnetic field B_y are discontinuous while the total pressure $P_t = P + B^2/2$ remains continuous. This discontinuity is known as tangential discontinuity because the plasma flow and the magnetic field remain tangential to the discontinuity surface while being discontinuous across it.

Rotational discontinuity: A rotational discontinuity rotates the magnetic field around the normal of the discontinuity surface over an angle of 180 degrees, without a jump in entropy. The magnitude of the magnetic field remains equal on both sides of the discontinuity. A rotational discontinuity propagates with Alfvénic speed c_a as the normal Alfvénic-Mach number is one on both sides of the discontinuity.

Rarefaction wave: There are two types of rarefaction/expansion waves in MHD referred to as fast rarefaction and slow rarefaction. The magnitude of the tangential magnetic field B_y decreases across a fast rarefaction while it increases across a slow rarefaction.

Compound wave: A compound wave is basically a shock followed immediately by a rarefaction wave. This is not unusual to find such waves in MHD flows and their occurrence maybe attributed to the non-convexity of the system.

A comprehensive overview of the various possible discontinuities in MHD flows and the jumps of different primitive variables across them are summarised in Appendix A.3.

2.4 Solenoidality constraint

In Section 2.1 we have discussed the system of ideal MHD equations. To understand the solenoidality constraint and its significance let us first recall the induction equation Eq. (2.3) which reads,

$$\frac{\partial \mathbf{B}}{\partial t} = -\nabla \cdot (\mathbf{VB} - \mathbf{BV})$$

Using the vector identity $\nabla \times (\mathbf{a} \times \mathbf{b}) = \nabla \cdot (\mathbf{ba} - \mathbf{ab})$ one can write the above equation as,

$$\frac{\partial \mathbf{B}}{\partial t} = \nabla \times (\mathbf{V} \times \mathbf{B}) \tag{2.19}$$

Taking divergence of the above equation, we have

$$\frac{\partial}{\partial t}(\nabla \cdot \mathbf{B}) = \nabla \cdot [\nabla \times (\mathbf{V} \times \mathbf{B})] = 0 \tag{2.20}$$

Eq. (2.20) indicates that if $\nabla \cdot \mathbf{B} = 0$ is satisfied initially, it will always be satisfied automatically at all times. At the level of the PDE, there is no problem since Eq. (2.5) is a part of the ideal MHD system (as described in Section 2.1) which always guarantees the satisfaction of Eq. (2.20). However, this is not true at the discrete level and poses issues in numerical simulations. Since the operator $\nabla \cdot \big[\nabla \times (\cdot)\big]$ is not exactly zero in numerical discretisations, truncation errors in $\nabla \cdot \mathbf{B}$ are generated. These errors get accumulated with time and may destabilise the numerical simulation. The lack of mimetic operators for the divergence and curl means that Eq. (2.5) cannot be numerically satisfied exactly and it is regarded as a constraint called the "solenoidality constraint".

To understand the effect of nonzero $\nabla \cdot \mathbf{B}$, let us consider the momentum equation Eq. (2.2),

$$\frac{\partial(\rho\mathbf{V})}{\partial t} + \nabla \cdot (\rho\mathbf{V}\mathbf{V} + \mathbf{I}P_t - \mathbf{B}\mathbf{B}) = 0$$

After expanding the last term of the above equation, we get

$$\frac{\partial(\rho\mathbf{V})}{\partial t} + \nabla \cdot (\rho\mathbf{V}\mathbf{V}) + \nabla(P + \frac{1}{2}B^2) - (\mathbf{B} \cdot \nabla)\mathbf{B} - \mathbf{B}(\underline{\nabla \cdot \mathbf{B}}) = 0 \qquad (2.21)$$

The underlined term in the above equation should be equal to zero according to Eq. (2.5). However, if $\nabla \cdot \mathbf{B} \neq 0$, the last term of the Eq. (2.21) can act as an extra unphysical force parallel to the magnetic field. This extra force leads to unphysical magnetic field topologies causing plasma transport orthogonal to the magnetic field which violates the fundamental assumption of the ideal MHD system, which says (from [62]), "*In ideal MHD, the magnetic field lines move with the plasma; in other words, they are frozen into the fluid*".

In another consequence, the conservative property of momentum, magnetic field and energy are not valid if $\nabla \cdot \mathbf{B} \neq 0$. This will cause the violation of Rankine-Hugoniot (RH) jump condition and can lead to incorrect shock capturing. On the other hand, a nonzero $\nabla \cdot \mathbf{B}$ may also lead to the existence of an extra compressive component in the magnetic field. This will cause an unphysical decrease in the thermal pressure P, since the magnetic energy is subtracted from the total energy in computing the pressure as shown in Eq. (2.7). Furthermore, this decrease can be up to such an extent that eventually the pressure becomes negative and the numerical simulation leads to non-physical solutions.

It is clear from the above discussion that generation of nonzero $\nabla \cdot \mathbf{B}$ is one of the major challenges in developing a numerical framework for ideal MHD. Several techniques have been developed to specifically deal with this issue. Some of these techniques of interest are discussed in the following section.

2.5 Solenoidality constraint-satisfying techniques

In order to satisfy the condition of a divergence-free magnetic field all through the temporal evolution, several methods of "divergence cleaning" have been proposed in literature. These include the classical projection scheme [32], the constrained transport method [33], eight-wave source term method [34], the Hyperbolic Divergence Cleaning (HDC) [35] and the Artificial Compressibility Analogy (ACA) method [1]. These methods are discussed below.

2.5.1 Projection scheme

This method was proposed by Brackbill and Barnes [32] where the magnetic field is modified as,

$$\mathbf{B}^* = \mathbf{B} + \nabla\xi \qquad (2.22)$$

so that,

$$\nabla \cdot \mathbf{B}^* = 0 \tag{2.23}$$

where ξ is an unknown potential function. To update the magnetic field, a Poisson equation has to be solved for the potential function ξ as given below.

$$\nabla^2 \xi = -\nabla \cdot \mathbf{B} \tag{2.24}$$

Thus, the calculated value of ξ is used to find $\nabla\xi$, which in turn used in Eq. (2.22) to project $\mathbf{B}^*$. It should be noted that the magnitude of the $\nabla \cdot \mathbf{B}$ errors depends on how accurately this Poisson equation is solved. Furthermore, obtaining the solution of this elliptic equation together with the hyperbolic ideal MHD equations is computationally expensive.

2.5.2 Constrained transport technique

Constrained transport (CT) technique [33] is developed to mimic the analytical property that the divergence of a curl operator $\nabla \cdot \left[\nabla \times (\cdot)\right]$ is zero. In this method a staggered mesh is typically used, where the hydrodynamic state variables are evaluated at the cell centers whereas the magnetic field is evaluated at the cell faces. This method is an extension of the staggered divergence-free scheme formulated for electromagnetism by Yee in [63]. CT techniques have been extensively used in the literature such as [14, 64–66] but the name "constrained transport" was given by Evans and Hawley [33]. It should be noted that employing staggered grids make this technique computationally expensive and complex especially on unstructured grids.

An unstaggered constraint transport method was also developed by Rossmanith in [67]. This scheme was referred to as magnetic potential advection constrained transport (MPACT) where all quantities, including the components of magnetic field are treated as cell-centered quantities.

2.5.3 Powell's source-term approach

In the previous section, it was shown by expanding the terms of the momentum equation that an extra unphysical force parallel to the magnetic field appears when $\nabla \cdot \mathbf{B} \neq 0$. In order to nullify this unphysical force term, Powell [34] recast the momentum equation in a different form as,

$$\frac{\partial(\rho \mathbf{V})}{\partial t} + \nabla \cdot (\rho \mathbf{V}\mathbf{V}) + \nabla(P + \frac{1}{2}B^2) - (\mathbf{B} \cdot \nabla)\mathbf{B} - \underline{\mathbf{B}(\nabla \cdot \mathbf{B})} = -\mathbf{B}(\nabla \cdot \mathbf{B}) \tag{2.25}$$

Powell tried to suppress the effect of the unphysical force by adding an extra term proportional to $\nabla \cdot \mathbf{B}$ (equal to the underlined term on LHS). The same

procedure was applied to the induction and the energy equations as well which results in the following non-conservative form of the ideal MHD equations,

$$\frac{\partial}{\partial t}\begin{bmatrix}\rho\\ \rho\mathbf{V}\\ \mathbf{B}\\ E\end{bmatrix}+\nabla\cdot\begin{bmatrix}\rho\mathbf{V}\\ \rho\mathbf{V}\mathbf{V}+\mathbf{I}P_t-\mathbf{B}\mathbf{B}\\ \mathbf{V}\mathbf{B}-\mathbf{B}\mathbf{V}\\ (E+P_t)\mathbf{V}-\mathbf{B}(\mathbf{B}\cdot\mathbf{V})\end{bmatrix}=-\nabla\cdot\mathbf{B}\begin{bmatrix}0\\ \mathbf{B}\\ \mathbf{V}\\ \mathbf{V}\cdot\mathbf{B}\end{bmatrix} \tag{2.26}$$

$$\nabla\cdot\mathbf{B}=0$$

The magnetic induction equation can now be expressed as,

$$\frac{\partial\mathbf{B}}{\partial t}+(\mathbf{V}\cdot\nabla)\mathbf{B}+\mathbf{B}(\nabla\cdot\mathbf{V})-(\mathbf{B}\cdot\nabla)\mathbf{V}=0 \tag{2.27}$$

Taking divergence of the above equation gives,

$$\frac{\partial}{\partial t}(\nabla\cdot\mathbf{B})+\nabla\cdot(\mathbf{V}\nabla\cdot\mathbf{B})=0 \tag{2.28}$$

Thus, any local value of $\nabla\cdot\mathbf{B}$ generated is convected away with the speed of $\mathbf{V}$. In other words, a partially conservative form of the multi-dimensional equations obtained by adding terms proportional to $\nabla\cdot\mathbf{B}$ adds an extra wave (eighth wave) that advects $\frac{\nabla\cdot\mathbf{B}}{\rho}$ as a passive scalar. It was later shown by Janhunen [68] that when the contribution to the total energy from the thermal pressure is small in comparison to the magnetic and kinetic energies, this approach could lead to unphysical negative thermal pressure. Janhunen [68] showed that this problem can be overcome by discarding the source terms in the energy and the momentum equations, so that Eq. 2.26 becomes,

$$\frac{\partial}{\partial t}\begin{bmatrix}\rho\\ \rho\mathbf{V}\\ \mathbf{B}\\ E\end{bmatrix}+\nabla\cdot\begin{bmatrix}\rho\mathbf{V}\\ \rho\mathbf{V}\mathbf{V}+\mathbf{I}P_t-\mathbf{B}\mathbf{B}\\ \mathbf{V}\mathbf{B}-\mathbf{B}\mathbf{V}\\ (E+P_t)\mathbf{V}-\mathbf{B}(\mathbf{B}\cdot\mathbf{V})\end{bmatrix}=-\nabla\cdot\mathbf{B}\begin{bmatrix}0\\ 0\\ \mathbf{V}\\ 0\end{bmatrix} \tag{2.29}$$

2.5.4 Hyperbolic divergence-cleaning approach

Dedner and his colleagues [35] developed the hyperbolic divergence-cleaning (HDC) approach which is based on introducing a generalized Lagrange multiplier to couple the solenoidality constraint with the ideal MHD equations by adding an extra equation. Different types of Lagrange multipliers were investigated and accordingly the additional equation was obtained in different forms: elliptic (equivalent to the projection scheme), parabolic (local $\nabla\cdot\mathbf{B}$ errors are dissipated and smoothed out), hyperbolic (local $\nabla\cdot\mathbf{B}$ errors are propagated to the boundary with a user-defined finite speed) or mixed hyperbolic-parabolic (local $\nabla\cdot\mathbf{B}$ errors

are both propagated and dissipated).

In this method, the solenoidality constraint is coupled to the hyperbolic system by introducing an unknown variable ψ and rewriting the induction equation Eq. (2.3) and the solenoidality constraint Eq. (2.5) in the following form.

$$\frac{\partial \mathbf{B}}{\partial t} + \nabla \cdot (\mathbf{VB} - \mathbf{BV}) + \nabla\psi = 0 \tag{2.30}$$

$$D(\psi) + \nabla \cdot \mathbf{B} = 0 \tag{2.31}$$

where D is a linear differential operator. For sufficiently smooth solutions Eq. (2.31) is written as [35]

$$\frac{\partial D(\psi)}{\partial t} - \nabla^2\psi = 0 \tag{2.32}$$

The differential operator D, the initial and the boundary conditions for ψ are chosen in such a way that the numerical approximation to the Eqs. (2.30) and (2.31) are good approximation to the original induction equation and the solenoidality constraint, respectively. For this reason, different choices for D have been proposed in [35] which are summarised below.

(1) Elliptic correction: In this case

$$D(\psi) = 0 \tag{2.33}$$

which reduces the method to the classical projection scheme.

(2) Parabolic correction: The choice of operator in this case is

$$D(\psi) = \frac{\psi}{c_p^2} \tag{2.34}$$

where, $0 < c_p < \infty$. Substituting Eq. (2.34) in Eq. (2.32) we get,

$$\frac{\partial \psi}{\partial t} - c_p^2 \nabla^2 \psi = 0 \tag{2.35}$$

which is analogous to the heat equation. Thus, local $\nabla \cdot \mathbf{B}$ errors are dissipated and smoothed out if suitable boundary conditions are provided.

(3) Hyperbolic correction: In this correction technique one assumes,

$$D(\psi) = \frac{1}{c_h^2}\frac{\partial \psi}{\partial t} \tag{2.36}$$

where, $0 < c_h < \infty$. Substituting Eq. (2.36) in Eq. (2.32) gives,

$$\frac{\partial^2 \psi}{\partial t^2} - c_h^2 \nabla^2 \psi = 0 \tag{2.37}$$

which is similar to the wave equation, implying the propagation of $\nabla \cdot \mathbf{B}$ errors to boundaries with the speed c_h. With this correction the generalized Lagrange multiplier (GLM) formulation (as mentioned in [35]) of the MHD equations becomes,

$$\frac{\partial}{\partial t}\begin{bmatrix} \rho \\ \rho\mathbf{V} \\ \mathbf{B} \\ E \\ \psi \end{bmatrix} + \nabla \cdot \begin{bmatrix} \rho\mathbf{V} \\ \rho\mathbf{V}\mathbf{V} + \mathbf{I}P_t - \mathbf{B}\mathbf{B} \\ \mathbf{V}\mathbf{B} - \mathbf{B}\mathbf{V} + \mathbf{I}\psi \\ (E + P_t)\mathbf{V} - \mathbf{B}(\mathbf{B} \cdot \mathbf{V}) \\ c_h^2 \mathbf{B} \end{bmatrix} = 0 \tag{2.38}$$

which is a hyperbolic system and ρ, $\rho\mathbf{V}$, $\mathbf{B}$ and E are still conserved as in the original ideal MHD system.

(4) Mixed correction: Combining the ideas of parabolic and hyperbolic corrections, one can also choose,

$$D(\psi) = \frac{\psi}{c_p^2} + \frac{1}{c_h^2}\frac{\partial \psi}{\partial t} \tag{2.39}$$

Substituting Eq. (2.39) in Eq. (2.32) gives the following telegraph equation.

$$\frac{\partial^2 \psi}{\partial t^2} + \frac{c_h^2}{c_p^2}\frac{\partial \psi}{\partial t} - c_h^2 \nabla^2 \psi = 0 \tag{2.40}$$

This renders both dissipation and propagation of $\nabla \cdot \mathbf{B}$ errors. As $c_p \to \infty$ this correction technique reduces to the hyperbolic correction. Now substituting Eq. (2.39) into Eq. (2.31) we get the modified solenoidality constraint, which is

$$\frac{\partial \psi}{\partial t} + c_h^2 \nabla \cdot \mathbf{B} = -\frac{c_h^2}{c_p^2}\psi \tag{2.41}$$

It can be observed from the above equation that the damping is now achieved by a source term instead of an explicit dissipation, eliminating restrictions on c_p otherwise imposed by the stability condition. It must be noted that all the equations for the physical variables are still conserved, while the only source term appearing corresponds to the unphysical variable ψ.

2.5.5 Artificial compressibility-analogy approach

The Artificial Compressibility-Analogy (ACA) method due to Yalim [1] is similar to Chorin's artificial compressibility method [36] for incompressible viscous

flows for ensuring a divergence-free velocity field. Yalim draws an analogy between the incompressibility condition $\nabla \cdot \mathbf{V}$ for incompressible viscous flows and the solenoidality constraint $\nabla \cdot \mathbf{B}$ for MHD flows. In Yalim's ACA method the solenoidality constraint is coupled to the induction equation in a way similar to the coupling of the incompressibility condition to the momentum equation in Chorin's method.

To discuss the method in some detail, first consider the equations of motion of an incompressible viscous fluid as given below:

$$\begin{aligned} \frac{\partial \mathbf{V}}{\partial t} + (\mathbf{V} \cdot \nabla)\mathbf{V} &= -\frac{\nabla P}{\rho} + \nu \nabla^2 \mathbf{V} + \mathbf{F} \\ \nabla \cdot \mathbf{V} &= 0 \end{aligned} \tag{2.42}$$

where ρ is the fluid density, $\mathbf{V}$ is the velocity vector, ν is the kinematic viscosity, P is the static pressure and $\mathbf{F}$ is the specific external force vector. Chorin modified the above equations by introducing an auxiliary term as given below:

$$\begin{aligned} \frac{\partial \mathbf{V}}{\partial t} + (\mathbf{V} \cdot \nabla)\mathbf{V} &= -\frac{\nabla P}{\rho} + \nu \nabla^2 \mathbf{V} + \mathbf{F} \\ \underline{\delta \frac{\partial P}{\partial t}} + \nabla \cdot \mathbf{V} &= 0 \end{aligned} \tag{2.43}$$

The extra (underlined) term is referred to as the artificial compressibility term which makes the time-marching technique possible by providing a direct means for updating pressure in order to find a steady state solution. The newly added time derivative term of pressure is suitably scaled by δ to make the time-marching system non-singular. Now let us recall the induction equation and the solenoidality constraint from the ideal MHD equations.

$$\begin{aligned} \frac{\partial \mathbf{B}}{\partial t} &= -\nabla \cdot (\mathbf{VB} - \mathbf{BV}) \\ \nabla \cdot \mathbf{B} &= 0 \end{aligned} \tag{2.44}$$

Drawing an analogy from Eq. (2.43) Yalim recast the above system as,

$$\begin{aligned} \frac{\partial \mathbf{B}}{\partial t} &= \underline{-\nabla \phi} - \nabla \cdot (\mathbf{VB} - \mathbf{BV}) \\ \underline{\frac{1}{V_{ref}^2} \frac{\partial \phi}{\partial t}} + \nabla \cdot \mathbf{B} &= 0 \end{aligned} \tag{2.45}$$

with two additional (underlined) terms that include a scalar potential function ϕ and a constant reference speed V_{ref}. The idea was to use the scalar potential ϕ to constrain the magnetic field to the space of divergence-free vector fields, just as P constrains the velocity to the space of divergence-free vector fields in the

incompressible flow equations.

The modified system of ideal MHD equations with the additional wave equation for solving the solenoidality constraint can then be obtained as below.

$$\frac{\partial}{\partial t}\begin{bmatrix}\rho\\ \rho\mathbf{V}\\ \mathbf{B}\\ E\\ \phi\end{bmatrix}+\nabla\cdot\begin{bmatrix}\rho\mathbf{V}\\ \rho\mathbf{V}\mathbf{V}+\mathbf{I}P_t-\mathbf{B}\mathbf{B}\\ \mathbf{V}\mathbf{B}-\mathbf{B}\mathbf{V}+\mathbf{I}\phi\\ (E+P_t)\mathbf{V}-\mathbf{B}(\mathbf{B}\cdot\mathbf{V})\\ V_{ref}^2\mathbf{B}\end{bmatrix}=0 \tag{2.46}$$

The above system of equations is hyperbolic in nature and is similar to Eq. (2.38) obtained in HDC approach [35]. Thus, ACA approach is a special variant of the HDC method with the hyperbolic Lagrange multiplier which is purely hyperbolic, fully conservative, and easy to implement. A major advantage of the ACA method is that it radiates away the divergence errors rapidly in all directions with the speed of V_{ref}, even in the vicinity of stagnation regions. Thus the solution is sensitive to the choice of V_{ref} which is kept constant globally over the whole computational domain. According to Yalim [1] this method is robust and quite accurate when V_{ref} is taken as the freestream flow speed for the whole domain. We shall largely employ this approach for 2D MHD simulations in this thesis where the satisfaction of the solenoidality constraint is paramount.

3

Wave-particle splitting for one-dimensional ideal MHD

In this chapter we describe the development of a novel flux splitting scheme based on the wave-particle behaviour to solve the ideal MHD equations. The scheme is motivated by the wave-particle class of schemes for the Euler equations. Here we describe the new scheme for one-dimensional MHD to begin with and its non-trivial extension to higher dimensions is discussed in the following chapter.

3.1 Acoustic Flux Vector Splitting

The Acoustic Flux Vector Splitting (AFVS) scheme [24] belongs to a class of wave-particle splitting schemes which includes AUSM [20] and CUSP [23] among others. The scheme exploits the fact that the inviscid fluxes can be split into convective and pressure parts, which may be handled separately. For the one-dimensional Euler equations, this splitting gives,

$$\mathbf{F} = \underbrace{\begin{bmatrix} \rho u \\ \rho u^2 \\ Eu \end{bmatrix}}_{\mathbf{F}^c} + \underbrace{\begin{bmatrix} 0 \\ P \\ Pu \end{bmatrix}}_{\mathbf{F}^p} \tag{3.1}$$

The convective fluxes $\mathbf{F}^c$ may be numerically evaluated using an upwind scheme as,

$$\mathbf{F}^c = M^{\pm}_{1/2} \begin{bmatrix} \rho a \\ \rho u a \\ E a \end{bmatrix}_{\mathrm{L/R}} \tag{3.2}$$

where the subscript L and R refer to the left and right states. The interfacial Mach number that determines the upwind direction is calculated as,

$$M^{\pm}_{1/2} = \frac{1}{2}(M_{\mathrm{L/R}} \pm |M_{\mathrm{L/R}}|) \tag{3.3}$$

and the Mach number is defined as

$$M = \frac{u}{a} \tag{3.4}$$

where a is the speed of sound.

The pressure fluxes $\mathbf{F}^p$ are however handled in a different manner. The specific form of pressure fluxes in AFVS scheme ensures that these fluxes are homogeneous of degree one and therefore one can write,

$$\mathbf{F}^p = \mathbf{A}^p\mathbf{U} \tag{3.5}$$

where $\mathbf{A}^p$ refers to the Jacobian of the pressure fluxes. Following the philosophy of flux splitting schemes, one can find the split pressure fluxes as

$$\mathbf{F}^{p\pm} = \mathbf{A}^{p\pm}\mathbf{U} \tag{3.6}$$

where the split flux Jacobians need to be suitably defined. This is made easier by the fact that $\mathbf{A}^p$ is a diagonalisable matrix with three eigenvalues 0 and $\pm(\sqrt{(\gamma-1)/\gamma})a$. The key idea behind the AFVS scheme is to split the zero eigenvalue as sum of ϕa and $-\phi a$, where $\phi > 0$ is a positive parameter that can be controlled to adjust the numerical dissipation of the scheme. Employing this idea to complete the split flux Jacobians leads to the final form of the split pressure fluxes, which reads,

$$\mathbf{F}^{p\pm} = \begin{bmatrix} \pm\sqrt{\frac{\gamma-1}{\gamma}}\phi a\rho \\ \frac{P}{2} \pm \sqrt{\frac{\gamma-1}{\gamma}}\phi a\rho u \\ \frac{Pu}{2} \pm \frac{Pa}{2\sqrt{\gamma(\gamma-1)}} \pm \sqrt{\frac{\gamma-1}{\gamma}}\phi a\frac{\rho u^2}{2} \end{bmatrix} \tag{3.7}$$

The idea behind the wave-particle splitting is inspired by the dynamics of the inviscid fluid which is due partly to wave motion and partly to the motion of the fluid particles [24]. This idea is also supported by the fact that the rate of change of a conserved quantity (momentum or energy) in a control volume is due to the change caused by the transport of fluid particle and the change caused by the pressure acting on the control volume. In other words, the dynamics of fluid can be regarded as a combined effect of the advection of fluid elements along particle paths and dilatation or contraction of the fluid elements emitting pressure waves into the domain. Thus it is physically meaningful to consider the fluid motion as partly particle-like and partly as wave-like and subsequently extend the idea to split the numerical fluxes into a transport-part and a pressure-part.

3.2 The flux vector decomposition for MHD

We discuss the decomposition of the flux vector for one-dimensional ideal MHD problems in this section. The governing equations for ideal MHD may be written in conservative form as,

$$\frac{\partial \mathbf{U}}{\partial t} + \frac{\partial \mathbf{F}}{\partial x} = 0 \tag{3.8}$$

where $\mathbf{U}$ is the vector of conservative variables and $\mathbf{F}$ is the flux vector in x-direction. Recall that the flux vector $\mathbf{F}$ reads,

$$\mathbf{F} = \begin{bmatrix} \rho u \\ P + \rho u^2 + \frac{1}{2}B^2 - B_x^2 \\ \rho uv - B_x B_y \\ \rho uw - B_x B_z \\ 0 \\ uB_y - vB_x \\ uB_z - wB_x \\ (E + P + \frac{1}{2}B^2)u - B_x(uB_x + vB_y + wB_z) \end{bmatrix}. \tag{3.9}$$

In 1D ideal MHD, it can be seen that the flux component corresponding to the conservative variable B_x is equal to zero and since there are no variations in the y and z directions, it follows that the fifth equation corresponding to B_x may be dropped without any loss of generality. Inspired by the splitting in AFVS scheme, we now split this flux vector $\mathbf{F}$ into three distinct parts as described below.

$$\mathbf{F} = \begin{bmatrix} \rho u \\ \rho u^2 \\ \rho uv \\ \rho uw \\ B_y u \\ B_z u \\ Eu \end{bmatrix} + \begin{bmatrix} 0 \\ P \\ 0 \\ 0 \\ 0 \\ 0 \\ Pu \end{bmatrix} + \begin{bmatrix} 0 \\ \frac{1}{2}B^2 - B_x^2 \\ -B_x B_y \\ -B_x B_z \\ -vB_x \\ -wB_x \\ \frac{1}{2}uB^2 - B_x(uB_x + vB_y + wB_z) \end{bmatrix} \tag{3.10}$$

From Eq. (2.7), we can also write

$$P = (\gamma - 1)[E - \frac{1}{2}\rho V^2 - \frac{1}{2}B^2] = (\gamma - 1)[E - \frac{1}{2}\rho V^2] - \frac{\gamma - 1}{2}B^2 \tag{3.11}$$

Using Eq. (3.11) in the definition of the flux vector and subsequent rearrangement gives,

$$\mathbf{F} = \mathbf{F}^t + \mathbf{F}^p + \mathbf{F}^m \tag{3.12}$$

$$\mathbf{F} = \underbrace{\begin{bmatrix} \rho u \\ \rho u^2 \\ \rho uv \\ \rho uw \\ B_y u \\ B_z u \\ Eu \end{bmatrix}}_{\mathbf{F}^t} + \underbrace{\begin{bmatrix} 0 \\ (\gamma - 1)[E - \frac{1}{2}\rho V^2] \\ 0 \\ 0 \\ 0 \\ 0 \\ (\gamma - 1)[E - \frac{1}{2}\rho V^2]u \end{bmatrix}}_{\mathbf{F}^p} + \underbrace{\begin{bmatrix} 0 \\ (1 - \frac{\gamma}{2})B^2 - B_x^2 \\ -B_x B_y \\ -B_x B_z \\ -vB_x \\ -wB_x \\ (1 - \frac{\gamma}{2})uB^2 - B_x(uB_x + vB_y + wB_z) \end{bmatrix}}_{\mathbf{F}^m} \tag{3.13}$$

The first part is called the transport part, denoted by $\mathbf{F}^t$ since it denotes the convection or transport of quantities by the flow velocity. The second part, $\mathbf{F}^p$ is the pressure part since it contains terms pertaining to the thermal pressure. The third part, represented as $\mathbf{F}^m$ is called the magnetic part since it consists of the remaining terms which correspond to the magnetic field components. The present splitting therefore separately categorises the non-transport part of the flux vector into two parts - the pressure part and the magnetic part. It must be realised that the pressure part of the flux vector still contains both the thermal and magnetic pressures and their effects do not appear in isolation. This is because the definition of total energy E contains contributions from both hydrodynamic and magnetic pressures (See Eq. (2.7)). For a purely hydrodynamic case ($\mathbf{B} = 0$), the pressure fluxes $\mathbf{F}^p$ would involve only thermal pressure and $\mathbf{F}^m$ would identically vanish rendering the splitting identical to that of AFVS scheme. The proposed decomposition of the MHD flux vector may therefore be considered as a generalisation of the idea of AFVS splitting to ideal MHD flows and the resulting scheme is aptly referred to as Magneto-acoustic Wave-Particle Splitting (MWPS) scheme. In the following sections, we discuss in detail the treatment of each of these individual flux vectors.

3.3 Treatment of the transport flux vector

The transport or convective fluxes represent the transport of the conserved variables by the flow velocity. From the viewpoint of wave-particle description, these transport fluxes exhibit a directional particle-like behaviour. The calculation of the fluxes at the control-volume faces is therefore based on the idea of upwinding and exploits the sign of the Mach number M. The discrete fluxes for the transport part may then be computed as,

$$\mathbf{F}^t = \begin{bmatrix} \rho u \\ \rho u^2 \\ \rho uv \\ \rho uw \\ B_y u \\ B_z u \\ Eu \end{bmatrix} = M^{\pm}_{1/2} \begin{bmatrix} \rho a_0 \\ \rho u a_0 \\ \rho v a_0 \\ \rho w a_0 \\ B_y a_0 \\ B_z a_0 \\ E a_0 \end{bmatrix}_{\mathrm{L/R}} \tag{3.14}$$

where the subscript L/R refers to the left/right state when the interfacial Mach number is positive/negative. The interfacial Mach number is calculated as,

$$M^{\pm}_{1/2} = \frac{1}{2}(M_{\mathrm{L/R}} \pm |M_{\mathrm{L/R}}|) \tag{3.15}$$

In case of MWPS scheme the Mach number is defined as

$$M = \frac{u}{a_0} \tag{3.16}$$

where,

$$a_0 = \sqrt{a^2 + b^2} \tag{3.17}$$

$$a^2 = \frac{\gamma P}{\rho} \tag{3.18}$$

$$b^2 = \frac{B^2}{\rho} \tag{3.19}$$

3.4 Treatment of the pressure flux vector

The construction of the pressure flux vector and consequently its numerical treatment is similar to that for the AFVS scheme. The pressure fluxes, as has already been stated, consist of both the thermal and magnetic pressures and show a wave-like behaviour as can be observed from the eigenvalues of the pressure flux Jacobian (See Appendix A.1). The seven eigenvalues are 0 (with multiplicity of 5) and $\pm\sqrt{\frac{\gamma-1}{\gamma}}a^*$, where a^* denotes the magneto-acoustic speed and is defined by,

$$a^* = \sqrt{a^2 + \frac{\gamma(\gamma-1)}{2}b^2} \tag{3.20}$$

Clearly, the magneto-acoustic waves are so called because the wave speed a^* depends both on thermal pressure and the magnetic pressure. Since these waves travel in all directions rather than a defined one, the corresponding fluxes exhibit a wave-like character. Nevertheless, the fluxes can be split into left-running and right-running waves, and this is made possible because of the diagonalisability of the Jacobian $\mathbf{A}^p$. The Jacobian matrix can be diagonalised as,

$$\mathbf{A}^p = \mathbf{R}\mathbf{\Lambda}^p\mathbf{R}^{-1} \tag{3.21}$$

where $\mathbf{R}$ is the matrix of right eigenvectors and $\mathbf{\Lambda}^p$ is the matrix of the eigenvalues. We then split the Jacobian into two parts, one consisting of positive eigenvalues and the other consisting of negative eigenvalues by splitting the eigenvalue matrix as,

$$\mathbf{\Lambda}^{p\pm} = \frac{\mathbf{\Lambda}^p \pm |\mathbf{\Lambda}^p|}{2} \tag{3.22}$$

where $\mathbf{\Lambda}^{p\pm}$ are given by,

$$\mathbf{\Lambda}^{p+} = \sqrt{\frac{\gamma-1}{\gamma}} \begin{bmatrix} \phi a^* & 0 & 0 & 0 & 0 & 0 & 0 \\ 0 & \phi a^* & 0 & 0 & 0 & 0 & 0 \\ 0 & 0 & \phi a^* & 0 & 0 & 0 & 0 \\ 0 & 0 & 0 & \phi a^* & 0 & 0 & 0 \\ 0 & 0 & 0 & 0 & \phi a^* & 0 & 0 \\ 0 & 0 & 0 & 0 & 0 & 0 & 0 \\ 0 & 0 & 0 & 0 & 0 & 0 & a^* \end{bmatrix} \tag{3.23}$$

$$\mathbf{\Lambda}^{p-} = \sqrt{\frac{\gamma-1}{\gamma}} \begin{bmatrix} -\phi a^* & 0 & 0 & 0 & 0 & 0 & 0 \\ 0 & -\phi a^* & 0 & 0 & 0 & 0 & 0 \\ 0 & 0 & -\phi a^* & 0 & 0 & 0 & 0 \\ 0 & 0 & 0 & -\phi a^* & 0 & 0 & 0 \\ 0 & 0 & 0 & 0 & -\phi a^* & 0 & 0 \\ 0 & 0 & 0 & 0 & 0 & -a^* & 0 \\ 0 & 0 & 0 & 0 & 0 & 0 & 0 \end{bmatrix} \tag{3.24}$$

The key feature of the splitting, clearly motivated by the AFVS scheme, is that all zero eigenvalues of the flux Jacobian are written as the sum of ϕa^* and $-\phi a^*$. Although the splitting of the zero eigenvalue appears arbitrary, the inclusion of parameter ϕ allows for an effective means to control dissipation. We discuss the regulation of numerical dissipation in Section 3.6.3. The split Jacobians are then easily derived as,

$$\mathbf{A}^{p\pm} = \mathbf{R}\mathbf{\Lambda}^{p\pm}\mathbf{R}^{-1} \tag{3.25}$$

The fluxes $\mathbf{F}^{p+}$ and $\mathbf{F}^{p-}$ are then constructed based on the homogeneity property as,

$$\mathbf{F}^{p\pm} = \mathbf{A}^{p\pm}\mathbf{U} = (\mathbf{R}\mathbf{\Lambda}^{p\pm}\mathbf{R}^{-1})\mathbf{U} \tag{3.26}$$

The components of $\mathbf{F}^{p+}$ are backward differenced and those of $\mathbf{F}^{p-}$ are forward differenced. The final expression for the split fluxes of the pressure flux vector reads,

$$\mathbf{F}^{p\pm} = \begin{bmatrix} \pm\sqrt{\frac{\gamma-1}{\gamma}}\phi a^*\rho \\ \frac{P}{2} + \frac{\gamma-1}{4}B^2 \pm \sqrt{\frac{\gamma-1}{\gamma}}\phi a^*\rho u \\ \pm\sqrt{\frac{\gamma-1}{\gamma}}\phi a^*\rho v \\ \pm\sqrt{\frac{\gamma-1}{\gamma}}\phi a^*\rho w \\ \pm\sqrt{\frac{\gamma-1}{\gamma}}\phi a^* B_y \\ \pm\sqrt{\frac{\gamma-1}{\gamma}}\phi a^* B_z \\ \frac{Pu}{2} + \frac{\gamma-1}{4}uB^2 \pm \frac{Pa^*}{2\sqrt{\gamma(\gamma-1)}} \pm \sqrt{\frac{\gamma-1}{\gamma}}\phi a^*\frac{\rho V^2}{2} \pm \sqrt{\frac{\gamma-1}{\gamma}}\frac{B^2 a^*}{4} \end{bmatrix} \tag{3.27}$$

3.5 Treatment of the magnetic flux vector

The treatment of the magnetic flux vector is done differently to those of pressure fluxes, despite the two parts being non-transport components of the total flux vector. The flux Jacobian for the magnetic flux vector $\mathbf{A}^m$ has three eigenvalues that are real and show multiplicity, with the wave speeds predictably being a function of the magnetic field. The full flux Jacobian for the magnetic flux vector and its eigenvalue matrix can be found in Appendix A.2. Unfortunately, the magnetic flux Jacobian is defective and therefore non-diagonalisable. In addition,

the magnetic flux vector is not homogeneous either and consequently it is not possible to evolve a flux splitting approach for the magnetic flux vector. These observations which are specific to MHD flows make it further challenging to extend the wave-particle splitting approach to MHD. The differences in the nature of pressure and magnetic flux Jacobians as well as the need to keep the new scheme simple yet robust and accurate, motivates the choice of a central scheme with scalar dissipation to treat the magnetic flux vector along the lines proposed by Jaisankar and Rao [31]. The magnetic flux vector may therefore be evaluated as,

$$\mathbf{F}^m = \frac{1}{2}(\mathbf{F}^m_{\mathrm{L}} + \mathbf{F}^m_{\mathrm{R}}) - \frac{1}{2}\mathbf{S}(\mathbf{U}_{\mathrm{R}} - \mathbf{U}_{\mathrm{L}})$$

where L and R represent the left and right states at the interface and $\mathbf{S}$ represents the diagonal matrix of wave speeds obtained from Rankine-Hugoniot (RH) jump condition. The matrix $\mathbf{S}$ can be determined from the RH jump condition defined by,

$$\begin{bmatrix} \Delta\mathbf{F}^m_1 \\ \Delta\mathbf{F}^m_2 \\ \cdot \\ \cdot \\ \cdot \\ \cdot \\ \Delta\mathbf{F}^m_7 \end{bmatrix} = \begin{bmatrix} S_{1,I} & 0 & 0 & 0 & 0 & 0 & 0 \\ 0 & S_{2,I} & 0 & 0 & 0 & 0 & 0 \\ 0 & 0 & \cdot & 0 & 0 & 0 & 0 \\ 0 & 0 & 0 & \cdot & 0 & 0 & 0 \\ 0 & 0 & 0 & 0 & \cdot & 0 & 0 \\ 0 & 0 & 0 & 0 & 0 & \cdot & 0 \\ 0 & 0 & 0 & 0 & 0 & 0 & S_{7,I} \end{bmatrix} \begin{bmatrix} \Delta\mathbf{U}_1 \\ \Delta\mathbf{U}_2 \\ \cdot \\ \cdot \\ \cdot \\ \cdot \\ \Delta\mathbf{U}_7 \end{bmatrix}$$

The wave speeds can then be evaluated as,

$$\begin{bmatrix} S_{1,I} \\ S_{2,I} \\ \cdot \\ \cdot \\ \cdot \\ \cdot \\ S_{7,I} \end{bmatrix} = \begin{bmatrix} \frac{(\mathbf{F}^m_1)_{\mathrm{R}} - (\mathbf{F}^m_1)_{\mathrm{L}}}{(\mathbf{U}_1)_{\mathrm{R}} - (\mathbf{U}_1)_{\mathrm{L}}} \\ \frac{(\mathbf{F}^m_2)_{\mathrm{R}} - (\mathbf{F}^m_2)_{\mathrm{L}}}{(\mathbf{U}_2)_{\mathrm{R}} - (\mathbf{U}_2)_{\mathrm{L}}} \\ \cdot \\ \cdot \\ \cdot \\ \cdot \\ \frac{(\mathbf{F}^m_7)_{\mathrm{R}} - (\mathbf{F}^m_7)_{\mathrm{L}}}{(\mathbf{U}_7)_{\mathrm{R}} - (\mathbf{U}_7)_{\mathrm{L}}} \end{bmatrix}$$

However, from the perspective of numerical implementation, the diagonal elements of $\mathbf{S}$ can become non-physically high when the denominator $\Delta\mathbf{U}$ is very small. Following [31], we employ a wave-speed limiter to restrict these speeds to physically admissible values. The idea is to simply keep the absolute values of discrete wave speed within the spectrum of the characteristic values (eigenvalues) of the system while retaining the direction of the computed wave speed. The expression for the wave speeds that are employed in the central scheme then become,

$$S_{i,I} = \begin{cases} \left| \frac{(\mathbf{F}_i^m)_{\mathrm{R}} - (\mathbf{F}_i^m)_{\mathrm{L}}}{(\mathbf{U}_i)_{\mathrm{R}} - (\mathbf{U}_i)_{\mathrm{L}}} \right|, & \text{if } \mathbf{U}_{\mathrm{L}} \neq \mathbf{U}_{\mathrm{R}} \\ \lambda_{min}, & \text{otherwise} \end{cases}$$

$$S_{i,I} = \begin{cases} \lambda_{max}, & \text{if } |S_{i,I}| \geqslant \lambda_{max} \\ \lambda_{min}, & \text{if } |S_{i,I}| \leqslant \lambda_{min} \end{cases}$$

where λ_{max} and λ_{min} are the absolute values of the largest and smallest eigenvalues of the flux Jacobian matrix $\mathbf{A}^m$, which are $\frac{B_x}{\sqrt{\rho}}$ and 0 respectively. Furthermore, we need to ensure that the scheme does not detect rarefactions as jumps (since the flux calculations are based solely on RH condition) for which we modify the wave speeds obtained above using a blending function [31] as,

$$\tilde{S}_{i,I} = S_{i,I} + \psi\Big(\lambda_{max} - S_{i,I}\Big)$$

where ψ is calculated as,

$$\psi = 1 - \frac{|\rho_{i+1} - 2\rho_i + \rho_{i-1}|}{|\rho_{i+1} + 2\rho_i + \rho_{i-1}|}$$

The specific choice of ψ (which is bounded between 0 and 1) is inspired by the JST scheme [69] and it acts as an indicator to detect discontinuities in the flow. The quantities that jump across various discontinuities in MHD flows is detailed in Appendix A.3 and it is easy to see that a density jump is common to all discontinuities except the rotational discontinuity. Clearly, in the regions where the flow is discontinuous, ψ is negligibly small and the wave speeds in the central scheme come from the RH condition. In smooth flow regions, ψ approaches unity, and the central scheme merely reduces to the more diffusive local Lax-Friedrichs (LLF) scheme. This blending function used in computing the wave speeds in the central scheme also works as an entropy fix, providing the requisite numerical diffusion to the central scheme for accurately capturing the discontinuities and avoiding expansion shocks.

3.6 Higher-order accuracy and regulating dissipation

The numerical simulations of engineering problem require accurate solutions at reasonable computational cost, which suggests controlling the numerical dissipation. This problem is not straightforward and achieving an "optimally-dissipative" numerical scheme remains an open research topic. We shall however discuss aspects of obtaining higher-order accuracy and controlling numerical dissipation in the proposed MWPS scheme and investigate the robustness and accuracy of schemes for several canonical problems in MHD.

3.6.1 Second-order accurate schemes and solution-dependent weighted least-squares approach

Numerical schemes which are first-order accurate are easy to implement and stable but introduce significant numerical diffusion. The design of higher-order schemes while desirable is made difficult by the need to overcome the Godunov barrier. This follows from the barrier theorem which states that, "Linear numerical schemes for solving partial differential equations, having the property of not generating new extrema (a monotone scheme), can be at most first-order accurate". Consequently, one has to introduce suitable non-linear fixes in a linear reconstruction to obtain "limited" fluxes. The states (primitive variables) on each face that defines the Riemann problem in a second-order scheme can thus be obtained as,

$$u_{i\pm\frac{1}{2}} = u_i + \left(\frac{du}{dx}\right)_i \Delta x_{i\pm\frac{1}{2}} \tag{3.28}$$

where $\Delta x_{i\pm\frac{1}{2}}$ is the distance between the interface $i \pm \frac{1}{2}$ and the cell centroid i. The gradients appearing in Eq. (3.28) are modified using a suitable limiter parameter $\phi \in [0, 1]$ so that the the reconstructed states do not violate monotonicity constraints. While several classical slope limiters can be implemented with ease, we adopt to implement the limited linear reconstruction by determining the gradients using a solution-dependent weighted reconstruction approach discussed in the following section.

3.6.2 Solution-dependent weighted least-squares reconstruction

The calculation of gradients in control volumes (or cells) in a finite volume framework can be achieved using either least-squares or Green-Gauss techniques. For the one-dimensional studies in this work, we adopt the former class of approaches where the gradients are estimated by a linear least-squares approach. We restrict our discussions herein to the role of solution-dependent weights while describing the least-squares approach in greater detail in the context of meshfree methods in Chapter 5. The least-squares reconstruction for gradients in a given cell i would require at least two neighbouring cells. The expression for the gradient for a uniform one-dimensional mesh with grid spacing Δx reads,

$$\left(\frac{du}{dx}\right)_i = \frac{w_1 \Delta u_1 + w_2 \Delta u_2}{(w_1 + w_2)\Delta x} \tag{3.29}$$

where u denotes any primitive variable, $\Delta u_1 = u_{i-1} - u_i$, $\Delta u_2 = u_{i+1} - u_i$ and w_1 and w_2 are the weight functions. Typically, the weights w_1 and w_2 are chosen as inverse-distances with the closer neighbours favoured more than the farther neighbours. The fundamental idea behind solution-dependent weighted least-squares approach is that it is possible to choose weights that are functions of the solution

itself that can automatically accommodate the effect of limiters. In other words, the use of solution-dependent weights as opposed to geometry-dependent weights results in "limited" gradients directly without the need to employ a separate limiting step. This idea, abbreviated as SDWLS, was proposed by Mandal and Subramanian [70] and can mimic the effects of several classical limiters and can be extended to non-uniform meshes and higher dimensions. In the present study, we consider uniform meshes unless otherwise specified and choose $w_1 = \Delta u_2^2$ and $w_2 = \Delta u_1^2$ which is equivalent to the van Albada limiter. The reconstructed states obtained by using the gradients in Eq. (3.29) in Eq. (3.28) are then used to obtain the fluxes using MWPS scheme and leads to nominally second-order accurate solutions and a stable solution procedure, as shall be demonstrated in Section 3.7.

3.6.3 Mechanisms for dissipation regulation

An important aspect of design of numerical schemes is the trade-off between solution accuracy and scheme robustness. While the use of SDWLS for gradient estimation and higher-order accuracy has already been discussed, the role of numerical diffusion and its effect on accuracy and numerical stability also needs to be looked into. One of the reasons why the AFVS scheme (discussed in Section 3.1) did not become popular was the excessive numerical diffusion and ad-hoc nature of dissipation control. We have attempted in the present study, albeit in a limited manner, to arrive at a more objective manner of regulating numerical diffusion.

The MWPS scheme clearly allows for an explicit control of numerical diffusion, first in the choice of ϕ and to a certain extent in the choice of ψ employed for the calculations of pressure fluxes and magnetic fluxes, respectively. Unlike the original AFVS scheme that employed ad-hoc Mach-polynomials in different regimes for the parameter ϕ, we adopt the diffusion regulation parameter approach of Jaisankar and Rao [71] in this work. The key idea of their approach is to vary the numerical diffusion, making it proportional to strength of the discontinuities and resorting to full numerical diffusion only in the proximity of strong discontinuities. The choice of ϕ thus depends on the jump in Mach number as opposed to the absolute values of the Mach number itself and can be determined as,

$$\phi = \begin{cases} \dfrac{|\Delta M|^2 + \delta^2}{2\delta}, & \text{if } |\Delta M| \leq \delta \\ |\Delta M|, & \text{if } \delta < |\Delta M| \leq 1.0 \\ 1, & \text{otherwise} \end{cases}$$

where, $\Delta M = M_{\mathrm{L}} - M_{\mathrm{R}}$ is the jump in the Mach number across the interface and δ is chosen as 0.25. The Mach number is defined in Eq. (3.16). While the choice of δ appears arbitrary, it has been arrived at by conducting extensive numerical

studies and was found to be sufficient in all cases considered in this work. The choice of ψ has been discussed earlier in Section 3.5 and partly plays a role in ensuring differential numerical diffusion at discontinuities and smooth flow regions. This combined regulation using ϕ and ψ parameters appearing in the flux formulae as discussed decreases the numerical diffusion considerably for first-order implementation of the MWPS. Reverting to a local Lax-Fredrich (LLF) scheme for magnetic part ($\psi = 1$) and employing ad-hoc polynomials for ϕ as suggested in [24] would clearly lead to excessive diffusion and would be detrimental to MHD studies which consist of one or more of several distinct flow features, which have been detailed in Appendix A.3.

The second-order MWPS scheme introduces much lesser numerical diffusion through upwinding and the use of the same expressions for computing ϕ and ψ could then prove to be detrimental to the overall stability of the algorithm. This was indeed confirmed in some of our numerical experiments, where the choice of ϕ and ψ described earlier led to non-physical oscillations. The studies seem to indicate that the second-order scheme works best in conjunction with ϕ and ψ values both equal to unity, which means that the maximum possible numerical diffusion is introduced in the pressure and magnetic flux calculations with the central scheme for the latter essentially reducing to the LLF scheme. While not necessarily optimal, it may be hypothesised that the second-order accurate treatment through limited linear reconstruction suffices to bring about a balance between robustness and accuracy in the higher-order implementation. On the other hand, choosing ϕ and ψ locally as functions of the Mach number and density respectively is the only means to achieve this delicate trade-off between stability and accuracy for the first-order implementation. We therefore present results using the second-order MWPS scheme, unless otherwise specified, with a constant value of unity for ϕ and ψ everywhere in the domain and discuss the need for and possibility of optimally diffusive schemes later in this chapter.

3.7 Results and discussion

The proposed MWPS scheme is tested on a spectrum of challenging benchmark one-dimensional problems to evaluate its ability to handle discontinuities and their interactions in MHD flows. Uniform meshes are employed for all tests with the initial conditions summarised in Table 3.1. We employ a first-order Euler explicit time-stepping scheme for all numerical simulations with a fixed time-step that satisfies the CFL condition. The MWPS scheme is also compared with the AUSM scheme to highlight the ability and advantage of the proposed flux splitting scheme to efficiently compute ideal MHD flows.

Test case	Left state							Right state						
	ρ	u	v	w	B_y	B_z	P	ρ	u	v	w	B_y	B_z	P
Sod [72]	1	0	0	0	0	0	1	0.125	0	0	0	0	0	0.1
Brio-Wu [5]	1	0	0	0	1	0	1	0.125	0	0	0	-1	0	0.1
Ryu-Jones 2a [8]	1.08	1.2	0.01	0.5	$\frac{3.6}{\sqrt{4\pi}}$	$\frac{2}{\sqrt{4\pi}}$	0.95	1	0	0	0	$\frac{4}{\sqrt{4\pi}}$	$\frac{2}{\sqrt{4\pi}}$	1
Ryu-Jones 4a [8]	1	0	0	0	1	0	1	0.2	0	0	0	0	0	0.1
Ryu-Jones 4c [8]	0.65	0.667	-0.257	0	0.55	0	0.5	1	0.4	-0.94	0	0	0	0.75
Near-vacuum [73]	10^{-6}	0	0	0	0	0	10^{-6}	1	0	0	0	1	0	0.5
Superfast Expansion [2]	1	-3.1	0	0	0.5	0	0.45	1	3.1	0	0	0.5	0	0.45
Low β [73]	1	-3.1	0	0	0.5	0	0.45	1	3.1	0	0	0.5	0	0.45
MHD Shu-Osher [4]	3.5	5.8846	0	1.1198	0	3.6359	42.0267	1	0	0	0	0	1	1
High-Mach MHD [28]	1	0	0	0	1	0	1000	0.125	0	0	0	-1	0	0.1
Stationary contact [19]	1	0	0	0	0	0	1	0.1	0	0	0	0	0	1
Stationary Alfvén wave [19]	$\frac{1}{4\pi}$	-1	1	-1	$\frac{-1}{\sqrt{4\pi}}$	$\frac{1}{\sqrt{4\pi}}$	1	$\frac{1}{4\pi}$	-1	-1	-1	$\frac{1}{\sqrt{4\pi}}$	$\frac{1}{\sqrt{4\pi}}$	1

Table 3.1. Initial left and right states of the test problems

3.7.1 Accuracy study

We begin our studies by investigating the implementation of the solution-dependent weighted least-squares approach and the overall global order of accuracy through a discontinuity-free MHD problem [74]. The exact solution for the problem is $\rho = 1 + 0.2\sin(\pi x - \pi t)$ with $u = 1$, $B_y = 1$, $P = 1$ everywhere in a [0,1] domain. The simulations are carried out up to a final time of $t = 1$ with a sufficiently small timestep of 10^{-5} using periodic boundary conditions on four progressively refined meshes having 200, 400, 800 and 1600 points, respectively. The specific heat ratio γ is taken as 1.4. The 1-norm of the error vector, which is the difference between the exact and numerical solution is calculated based on density and its variation with the grid spacing is shown in Figure 3.1. The error decreases with grid refinement and the slope of the error curve is 1.93, which is close to the theoretically expected rate of convergence of 2. This implies that the scheme shows nearly second-order accuracy numerically on uniform meshes although the rate of convergence is likely to decrease slightly in the presence of discontinuities and limiting [75]. This study conclusively proves that the proposed MWPS scheme with the SDWLS reconstruction is a second-order accurate approach for MHD flows. This nominally-second order accurate scheme is now employed in all the following test cases.

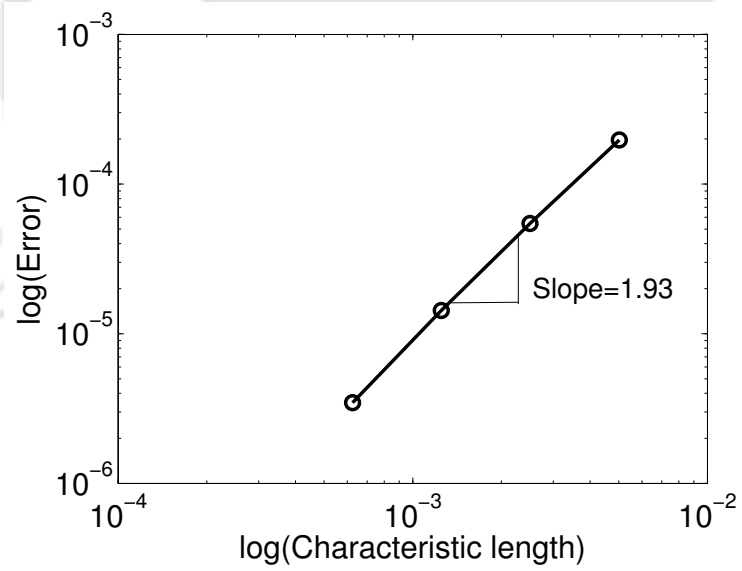

Figure 3.1. Variation of L_1-norm of density error with grid spacing

3.7.2 Sod shock tube problem

The Sod shock-tube problem is a benchmark problem in hydrodynamics with an analytical solution that can be used to compare several flux schemes. We

employ this test problem to compare the first and second-order MWPS schemes and highlight the need for a second-order accurate scheme. This study also helps to evaluate the ability of the MWPS scheme to resolve discontinuities accurately. Simulations are carried out on a [0,1] domain with 400 points using a timestep of 10^{-4} to a final time of 0.1. The comparison of the numerical solutions with the analytical solution in Figure 3.2 shows that the second-order accurate MWPS scheme is superior to its first-order counterpart as it captures the discontinuities as well as the expansion more sharply, thus bringing it closer to the exact solution. The MWPS scheme for this case actually reduces to the AFVS scheme except that the dissipation regulation is effected in a more objective manner in the present scheme. It must also be recalled that the implementation of dissipation regulation is done differently for the first and second-order MWPS schemes and this experiment serves to underscore the need for higher-order upwinding.

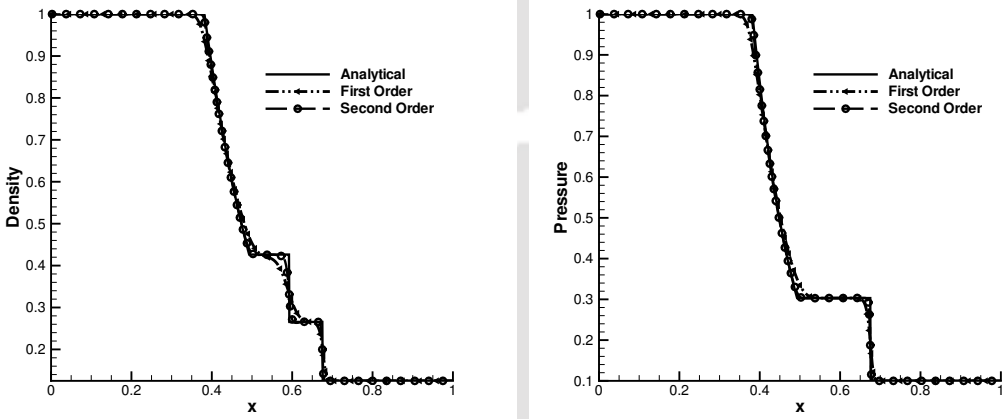

Figure 3.2. Solutions for Sod shock tube problem

3.7.3 Brio and Wu problem

The Brio and Wu problem is a MHD analogue of the Sod shock tube problem and is the first genuine test of the MWPS scheme. The solution consists of five distinct waves separated by constant states. The waves moving to the left are fast rarefaction wave (FR), and a slow compound wave denoted by SM. The waves moving to the right include a contact discontinuity (C), a slow shock (SS), and a fast rarefaction wave (FR). This coplanar MHD Riemann problem is solved on the same domain and grid as in the Sod test case, with a timestep of 10^{-4} to a final time of 0.1 with $B_x = 0.75$ and $\gamma = 1.4$. The numerical solutions obtained using MWPS and AUSM schemes on the same mesh of 400 points are compared in Figure 3.3. The non-convexity of the MHD system is evident in the density plot, which shows a compound wave (SM) that contains a slow shock

attached to a slow rarefaction moving towards the left. While the solutions from the two schemes show gross agreement, a closer inspection indicates that AUSM scheme produces spurious oscillations downstream of the compound wave, while also causing a minor overshoot at it as evidenced in the profile of y-magnetic field. The solutions from the MWPS scheme is devoid of these anomalies and captures all five waves accurately, thus demonstrating that the scheme works equally well for MHD flows.

For the purposes of examining grid independence, a reference solution is computed on a finer uniform mesh of 1600 points using the same flux scheme. The density and magnetic field profiles shown in Figure 3.4 show a good agreement between the reference solution and the solution computed on the coarser mesh (of 400 points). This may be construed as a demonstration of grid independence and the solution on grid with 400 points may be treated as being mesh-independent.

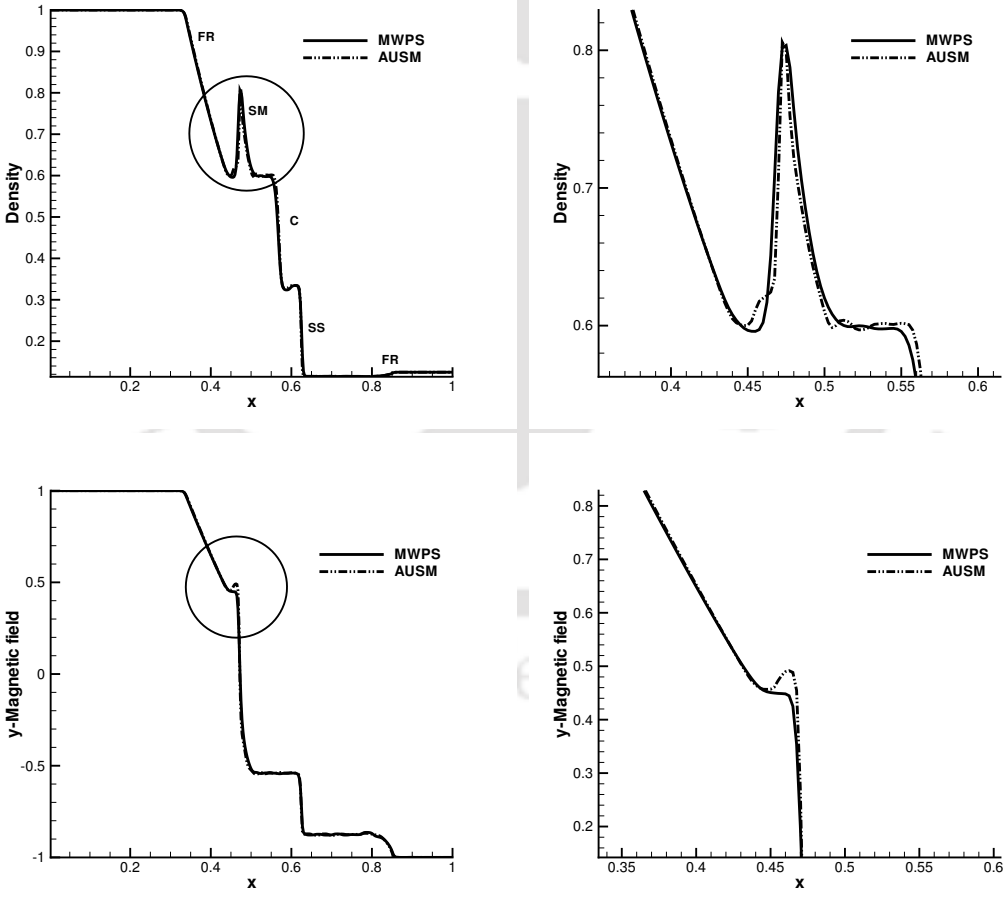

Figure 3.3. Solutions for Brio Wu shock tube problem (MWPS vs AUSM)

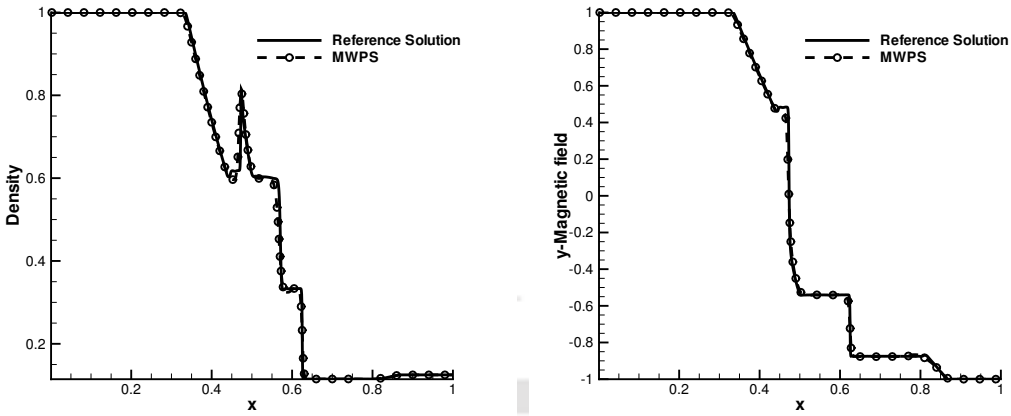

Figure 3.4. Solutions for Brio Wu shock tube problem (MWPS vs Reference)

3.7.4 *Ryu and Jones problem RJ-2a*

This MHD shock tube problem was first suggested by Dai and Woodward [7] and later solved by Ryu and Jones [8] and involves rotation of the magnetic field plane. Simulations are carried out on a [0,1] domain with 512 grid points with and a timestep of 10^{-5}, $B_x = 2.0/\sqrt{(4\pi)}$ and $\gamma = 5/3$ up to a final time $t = 0.2$. The numerical solutions contain seven discontinuities that include two rotational discontinuities (RD) which propagate to each side of the contact discontinuity (C). As in the previous test case a grid independence study has been carried out for this test case as well. Figure 3.5 shows the plots of density, y-magnetic field, x-velocity and y-velocity compared with the reference solution. The latter has been obtained on a grid with spacing four times smaller than the present one. It is clear that the discontinuities are correctly captured for both the finer and coarser grids, although some diffusion in the peaks of the rotational discontinuities are evident in case of the solutions on the coarser grid. Figure 3.6 compares the solutions from the MWPS and AUSM schemes for this problem. It can be observed that solutions from the AUSM scheme show an appreciable overshoot at the left fast shock and spurious oscillations downstream of it (observed in the density plot). The MWPS scheme does not cause either, although the rotational discontinuities seem to have been marginally damped by the numerical diffusion in the scheme (observed in the y-magnetic field). This test case also shows that the MWPS scheme does not necessarily have an "optimal" diffusion and numerically illustrates the difficulties of constructing schemes that optimally trade-off between accuracy and stability, in the MHD context.

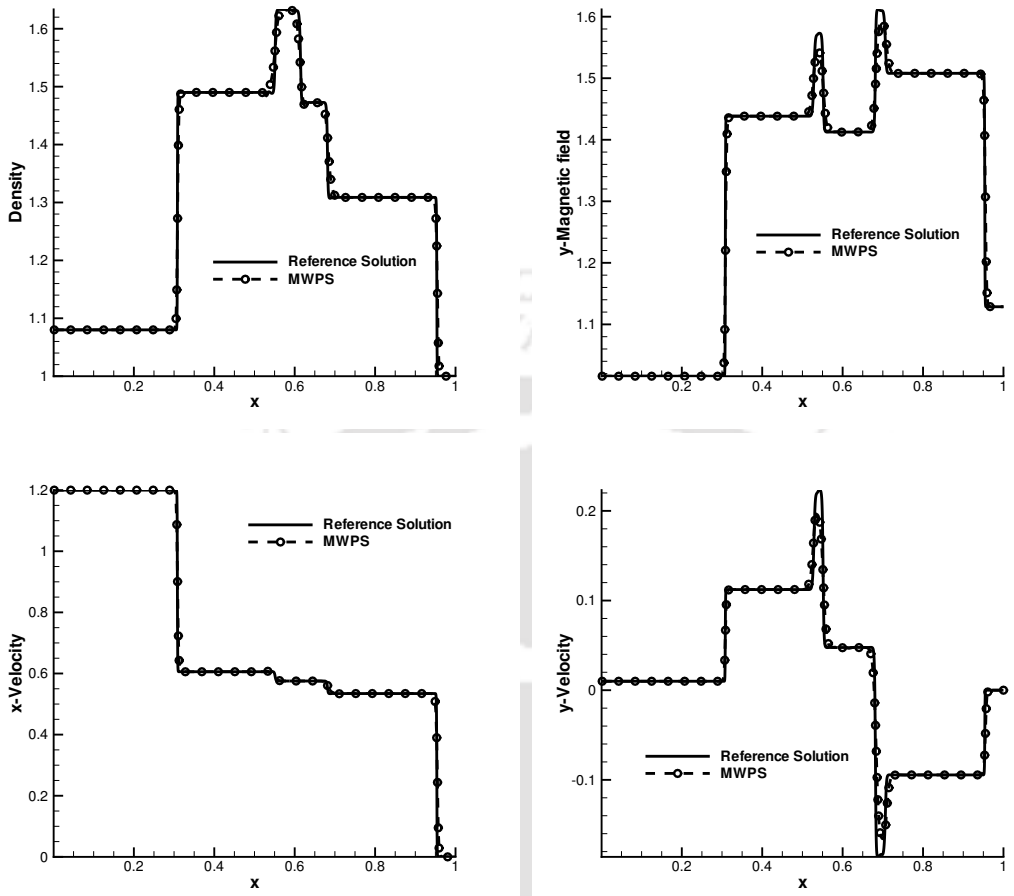

Figure 3.5. Solutions for Ryu and Jones problem 2a (MWPS vs Reference solution)

3.7.5 *Ryu and Jones problem RJ-4a*

The fourth test case, proposed by Ryu and Jones [8] is used to examine the ability of the schemes to resolve switch-on structures in the flow. These are differentiated from other discontinuities based on the fact that the tangential magnetic field turns-on in the region behind switch-on fast shocks. This test case is solved on the same domain and grid with the same timestep as in RJ-2a, but up to a final time of $t = 0.15$ with $B_x = 1.0$ and $\gamma = 5/3$. The plots of in-plane velocity in Figure 3.7 show that while there are minor differences between the MWPS and AUSM scheme in resolving the slow rarefaction (SR), MWPS does not suffer from non-physical oscillations at the slow shock (SS), which is also evident in the profile of the y-magnetic field. Both schemes do however lead to a zero value of y-magnetic field in the pre-shock region for the switch-on fast shock at the extreme right.

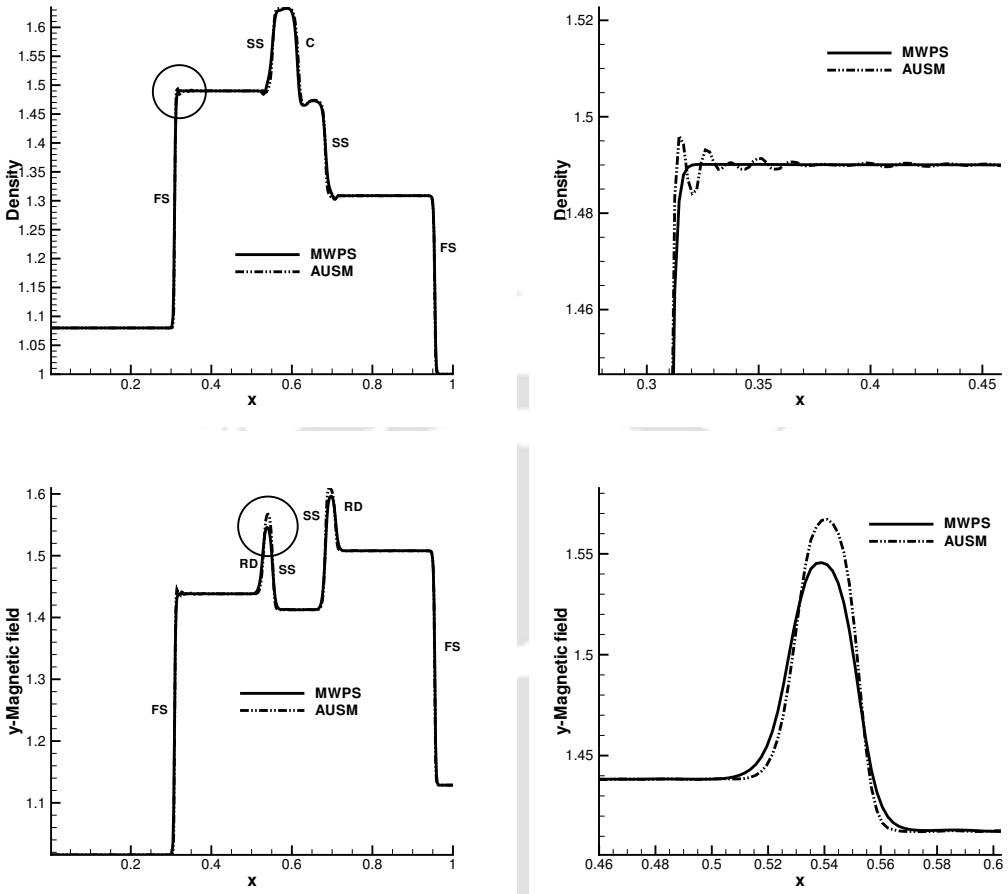

Figure 3.6. Solutions for Ryu and Jones problem 2a (MWPS vs AUSM)

3.7.6 *Ryu and Jones problem RJ-4c*

This test case taken from [8], evaluates the ability of the numerical schemes to deal with switch-off structures, which can be distinguished by the fact that the tangential part of the magnetic field is non-zero in the pre-shock state but vanishes in the post-shock state. Except for the initial conditions, the simulations are carried out in identical conditions as in the RJ-4a case with the exceptions that $B_x = 0.75$ and $\gamma = 5/3$. Not surprisingly, the flow features that appear in the solutions shown in Figure 3.8 are different to that in RJ-4a case, with the appearance of a hydro-shock across which the tangential magnetic fields are negligibly small. It is interesting to see that the location of the weak fast shock seems to be predicted differently by the two schemes as shown in the density plot (zoomed view) which otherwise show excellent agreement in resolving all other flow features, except for a minor undershoot displayed by the AUSM scheme in the y-magnetic field (zoomed view) at the switch-off shock.

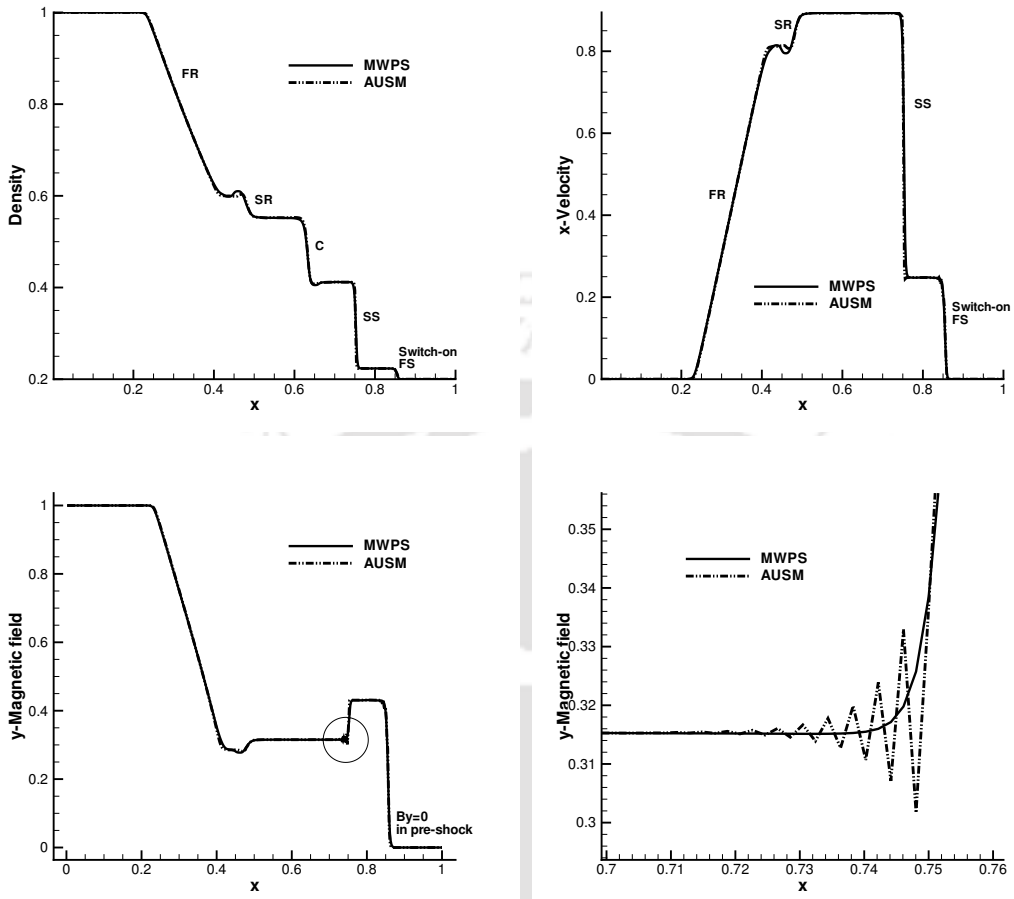

Figure 3.7. Solutions for Ryu and Jones problem 4a

3.7.7 Near-vacuum shock tube problem

The ability of the proposed scheme to handle vacuum data is investigated using this test case, which is quite similar to that in [73]. A grid with 400 points in [0,1] domain is used for the simulations that are carried out till $t = 0.05$ with a timestep of 10^{-5}, $B_x = 0$ and $\gamma = 2$. The density profiles obtained using both MWPS and AUSM are compared with the analytical solution [76] in Figure 3.9. The agreement between the numerical results and the analytical solution is good for both schemes, which shows that these higher-order accurate flux schemes lead to non-negative pressure and densities for this test case.

3.7.8 Superfast expansion problem

The choice of this MHD shock tube problem [2] is motivated by the need to further study positivity preservation for one-dimensional MHD solvers. The choice of

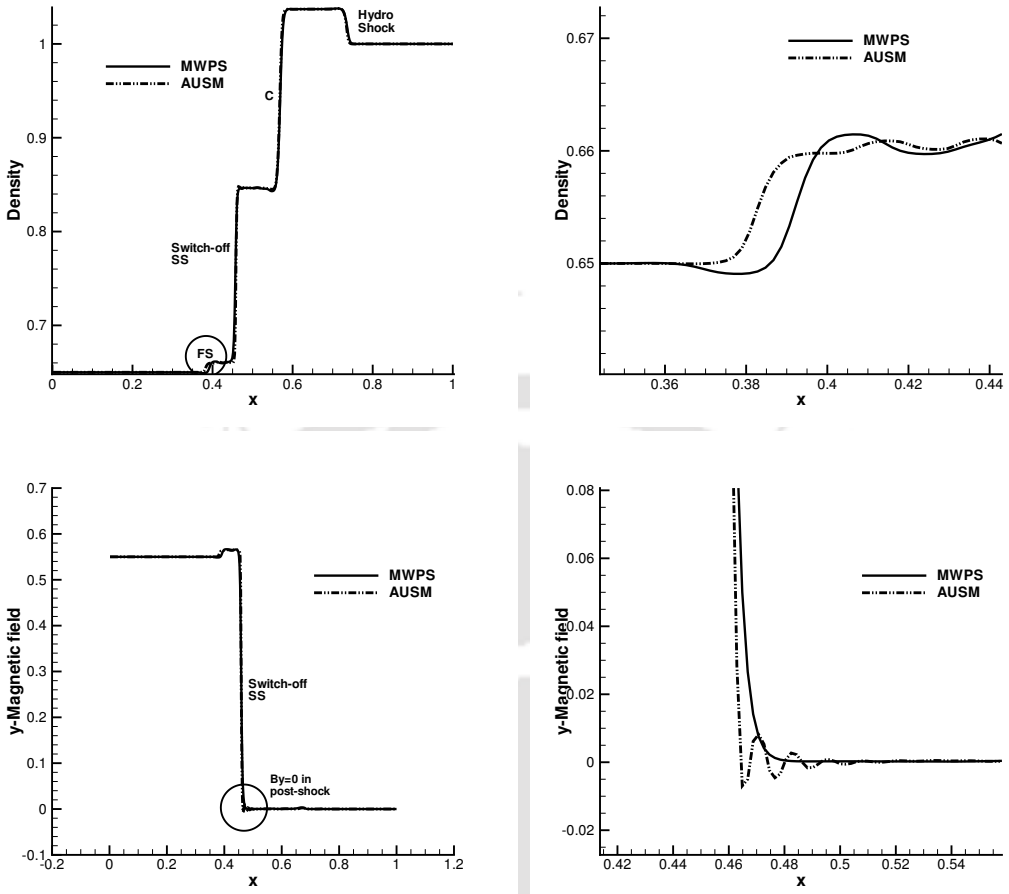

Figure 3.8. Solutions for Ryu and Jones problem 4c

initial conditions are such that the exact solution consists of two fast-moving expansions with a Mach number of 3.1, subsequently leading to a very low-pressure, low-density region at the location of the initial discontinuity. The numerical simulations are performed on a unit length domain with 800 grid points up to $t = 0.05$ using a constant time-step of 10^{-5} with $B_x = 0$ and $\gamma = 1.4$. The plots of pressure and density in Figure 3.10 along the length of the tube show that the AUSM scheme leads to completely non-physical solutions although pressure and density remain non-negative whereas the MWPS scheme computes an accurate and smooth solution.

3.7.9 Low β problem

This test case adopted from [73] is a variant of the test problem discussed above in Section 3.7.8, with a non-zero B_x which presents an additional challenge for MHD flux schemes. A grid with 400 points in [0,2] domain is used for the simulations

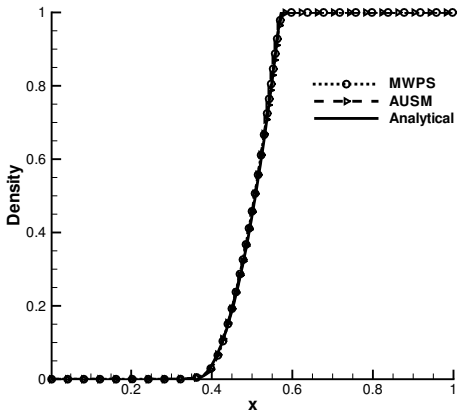

Figure 3.9. Density profile of near-vacuum shock tube problem

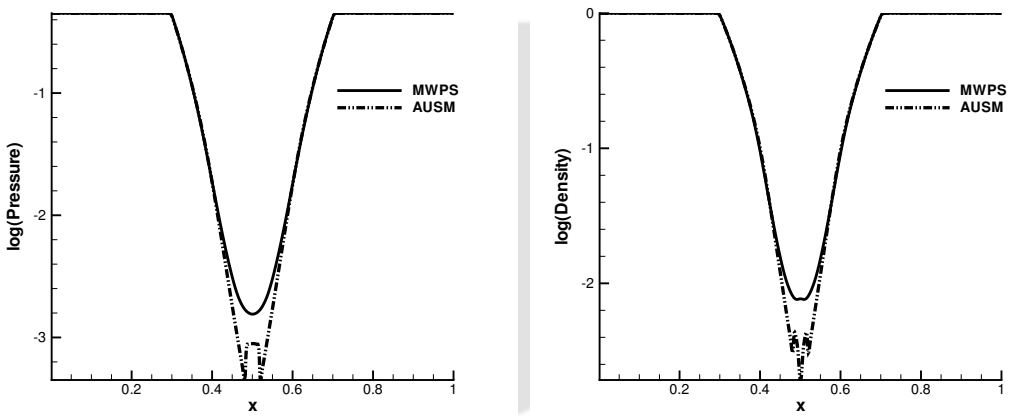

Figure 3.10. Solutions for superfast expansion test

that are carried out till $t = 0.15$ with a timestep of 10^{-6}, $B_x = 1.0$ and $\gamma = 5/3$. The density as well as $\beta = \frac{2P}{B^2}$ (ratio of thermal and magnetic pressures) obtained using MWPS are compared with the reference solution in Figure 3.11, the latter simulated using a grid four times finer than that used in the study. The results indicate that the MWPS scheme works well even for this challenging test problem and maintains the positivity of pressure and density. It is interesting to note that for the same set of simulation parameters the AUSM scheme failed to produce physically meaningful solutions.

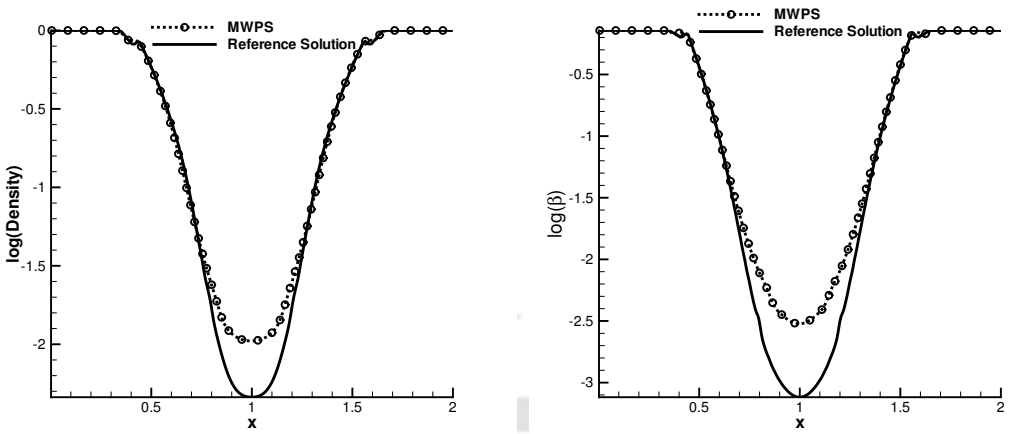

Figure 3.11. Solutions for low β problem

3.7.10 Shu-Osher MHD problem

This is a MHD version of the Shu-Osher shock tube problem from [4] and helps to investigate the ability of higher-order numerical schemes to resolve small-scale flow features in the presence of shocks in a magnetic field. A sinusoidal density perturbation of 0.2 $\sin(5x)$ is added downstream of a purely advecting supersonic shock wave, which gives rise to fast oscillations and complex flow features downstream of the shock. A grid with 3000 points in [-5,5] domain is used for the simulations that are carried out till $t = 0.6909$ with a timestep of 10^{-4}, $B_x = 1.0$ and $\gamma = 5/3$. The density profile along the length of the tube obtained using MWPS is shown in Figure 3.12. The MWPS scheme resolves the complex and small-scale flow features quite well and the results from the present simulation are in good agreement with the second-order numerical results from [4].

3.7.11 High-Mach MHD problem

The high-Mach MHD test case is a shock-tube problem involving very high Mach numbers and is adapted from [28]. Simulations are carried out on a grid with 400 points with a timestep of 10^{-6} on a [0,2] domain with $B_x = 0$ and $\gamma = 2$. The results plotted in Figure 3.13 at $t = 0.012$ show that the second-order accurate MWPS scheme does well to resolve the discontinuities at Mach numbers as high as 15, underlining the ability of the scheme to remain stable without unduly compromising on the solution accuracy.

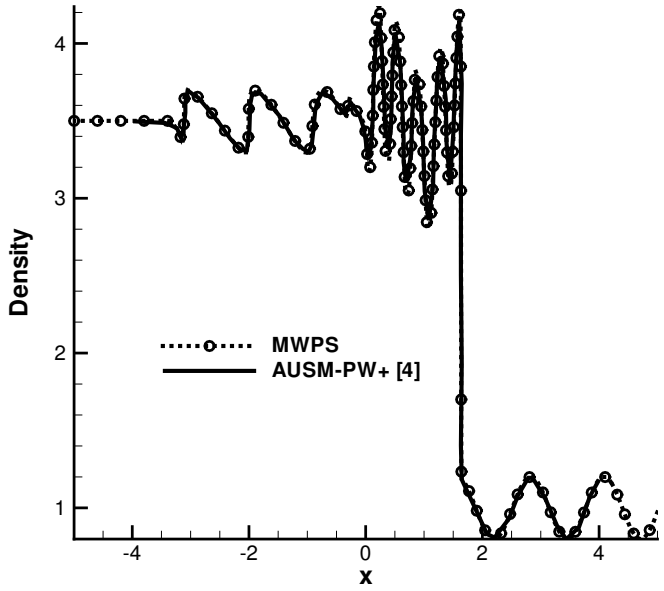

Figure 3.12. Density profile of MHD variant of Shu-Osher test

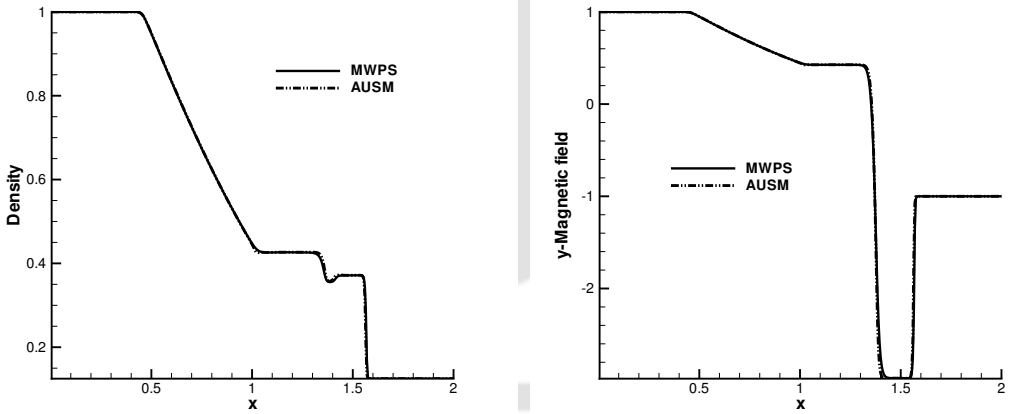

Figure 3.13. Solutions for high-Mach MHD test

3.8 Resolution of isolated stationary discontinuities

One of the important and desirable properties of new flux schemes is their ability to accurately resolve isolated discontinuities. We test the ability of the new flux splitting scheme to resolve stationary discontinuities by considering two different problems, originally proposed in [19]. For both problems a grid with 400 points in [0,1] domain is used for the simulations that are carried out till $t = 0.25$

with a timestep of 10^{-4}, $B_x = 1.0/\sqrt{4\pi}$ and $\gamma = 5/3$. The first test problem consists of an isolated stationary contact discontinuity across which only the density experiences a jump, while the second problem involves an isolated Alfvén wave discontinuity across which the y-component of velocity and magnetic field are discontinuous. Figure 3.14 shows the density and magnetic field profiles for the stationary contact and Alfvén wave discontinuity respectively. Unlike the HLLD solver in [13], the present scheme does not *exactly* resolve the isolated stationary discontinuities. Nevertheless, the results show that the smearing of the discontinuities with the second-order MWPS scheme are not significant and is lesser in comparison to the first-order MWPS scheme. This inability of the MWPS scheme to exactly capture the discontinuities is owing to the structure of the numerical diffusion term (See Appendix A.4). It must be noted that the first-order MWPS scheme has a solution-dependent diffusion regulation (See Section 3.6.3 and Section 3.10) that improves the resolution of discontinuities considerably as compared to a first-order scheme without any diffusion regulation. These studies indicate that the second-order-accurate MWPS scheme is able to locate stationary isolated discontinuities in the flow correctly with a low and acceptable amount of numerical diffusion. We remark that while linearised Riemann solvers [13] for MHD can exactly capture isolated discontinuities, they are known to result in negative density or pressure even for simple problems.

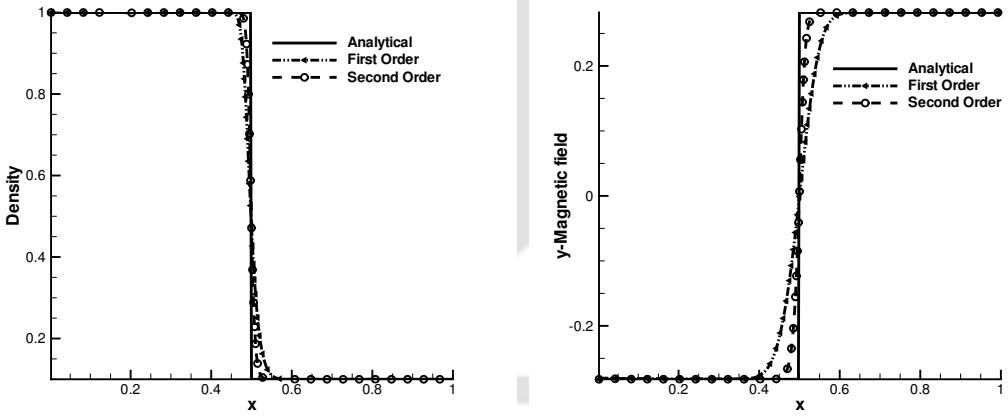

Figure 3.14. Density profile of stationary contact discontinuity (Left) and Magnetic field profile for stationary Alfvén wave discontinuity (Right)

3.9 Comparing MWPS and central Rankine-Hugoniot solvers

The proposed MWPS scheme generalises and improves upon the AFVS scheme for MHD flows and splits the total flux vector into three distinct parts which

are treated differently. It is worthwhile, however, to compare the MWPS scheme with a fully central scheme and investigate the relative advantages and disadvantages. A full central scheme is one where the complete flux vector is treated in a manner analogous to the magnetic flux vector and Jaisankar and Rao [31] have proposed a scheme, referred to as CRH (Central Rankine-Hugoniot), which has been investigated on several hyperbolic problems of interest. A significant advantage of CRH scheme is that it is free of any Jacobian calculations making it a simple approach to implement in finite-volume solvers. However, this scheme has not been thoroughly investigated for challenging MHD problems and it is not possible to arrive at a conclusion on its viability for MHD flows. We attempt to understand the CRH scheme for MHD through a select number of problems which have been discussed earlier in this chapter and compare the solutions with those of MWPS. It must be noted that only the first-order counterparts of both the schemes are used for this analysis.

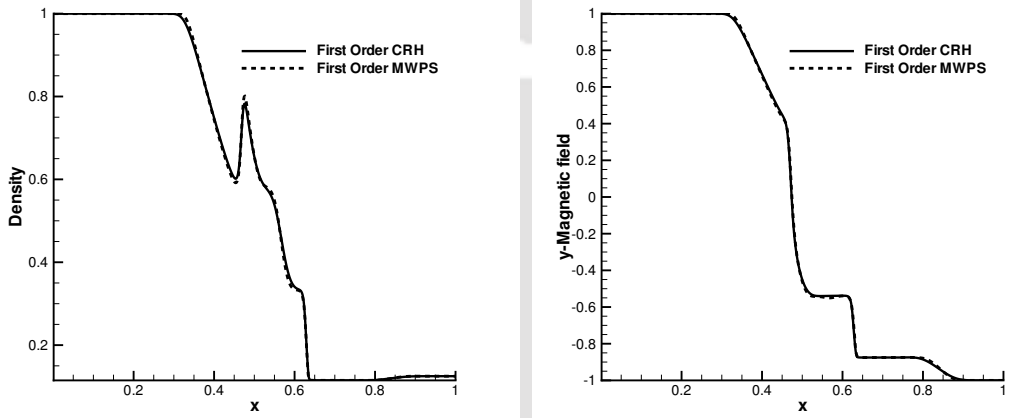

Figure 3.15. Solutions for Brio and Wu (First-order CRH vs first-order MWPS)

We carry out simulations using the first-order MWPS and CRH schemes for five different 1-D problems. Figure 3.15 shows the results for the Brio-Wu shock tube problem, where the first-order MWPS scheme is found to be marginally less diffusive than the CRH scheme with all relevant flow features (including the compound wave) being resolved by both the schemes. The differences between the schemes are relatively more pronounced in the RJ-2a test case, where the CRH scheme exhibits greater diffusion, as the rotational discontinuities are damped more compared with the MWPS scheme. This is evident in the y-magnetic field profiles shown in Figure 3.16. Interestingly, the CRH scheme is superior to the MWPS scheme for the isolated Alfvén wave discontinuity problem and exactly captures the discontinuity, as shown in Figure 3.17. This is not surprising since the exact resolution of discontinuities is built into the CRH scheme, while

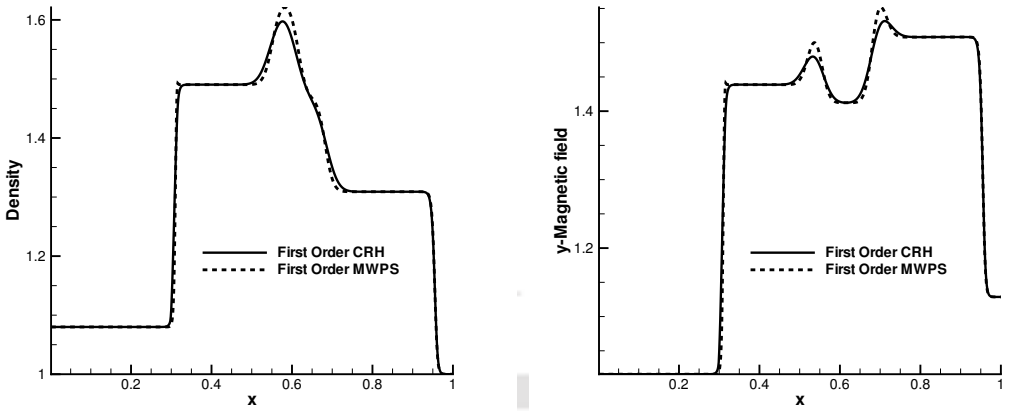

Figure 3.16. Solutions for Ryu and Jones problem 2a (First-order CRH vs first-order MWPS)

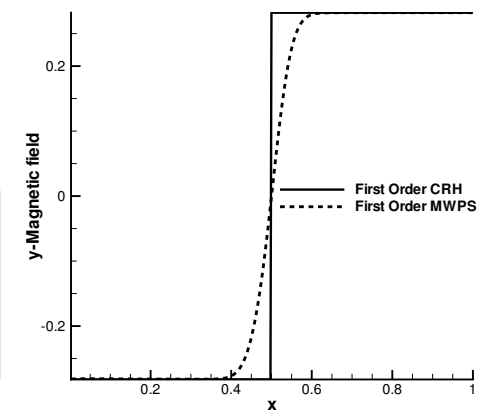

Figure 3.17. Solutions for isolated Alfvén wave discontinuity (First-order CRH vs first-order MWPS)

the MWPS scheme smears the contact wave. However, it may be recalled that the second-order MWPS scheme reduces the numerical diffusion considerably although an exact resolution is still not possible with the MWPS scheme. Our studies with the CRH scheme for low β and superfast expansion tests resulted in failed numerical simulations, signalling that the CRH scheme could not maintain the positivity of pressure and density for these challenging scenarios, despite being first-order accurate. While CRH scheme was only sparingly studied in [31] with respect to two MHD problems and found to perform well, our investigations reveal that the MWPS scheme would indeed be superior to the CRH over a large spectrum of test problems in MHD. We remark that while the CRH scheme in

itself is interesting and has potential drawbacks for MHD, the MWPS scheme which borrows a part of its construction from the CRH scheme is a more robust flux-splitting scheme for MHD applications.

3.10 A case for optimally-dissipative schemes for MHD

The numerical studies on a wide range of one-dimensional MHD problems in the earlier sections conclusively demonstrate that the second-order MWPS scheme is stable and accurate to resolve complex flow features and their interactions in MHD flows. While the investigations so far have concentrated on the second-order MWPS scheme, the need to improve upon the dissipation regulation for first-order MWPS scheme is briefly discussed in this section. It may be recalled that ϕ and ψ are obtained locally in each control volume as functions of the Mach jump and density jump at the interfaces for the first-order MWPS scheme, unlike its second-order counterpart. To understand the need of regulating numerical diffusion let us consider Figures 3.18 and 3.19 where density and y-magnetic field are plotted for the RJ-2a and Brio and Wu problems, respectively. Solutions are obtained using the first-order MWPS scheme with regulated dissipation parameters, and without regulating the dissipation parameters (*i.e.*, keeping $\phi = \psi = 1$). Since, assigning $\phi = \psi = 1$ gives maximum numerical diffusion, the solutions obtained by the first-order MWPS scheme without regulating the parameters produces more diffused solutions compared to the diffusion regulated counterpart of the same scheme. To get a deeper insight of the functioning of the dissipation regulators ϕ and ψ, the reader may refer to the Section 3.6.3 and Section 3.5, respectively.

Figures 3.20 and 3.21 show the density and y-magnetic field plots for the RJ-2a and RJ-4a problems, respectively given by the first-order MWPS scheme with regulated ϕ and ψ, and the AUSM scheme. The results of both the schemes show a good agreement for the RJ-2a test case (despite a minor overshoot for the MWPS scheme), but significant discrepancies can be observed for the RJ-4a test case. In particular, the MWPS scheme smears the slow rarefaction to a considerable extent and diffuses the right-moving slow shock as well, whereas the AUSM scheme resolves these features more accurately. In contrast to the first-order results, computations in Sections 3.7.4 and 3.7.5 clearly indicate that the second-order MWPS scheme is at least as accurate and even superior to the second-order AUSM scheme for these test problems. Clearly, while the second-order MWPS scheme appears to be "quasi-optimal" in terms of numerical dissipation, there exists ample room for reducing the numerical diffusion of the first-order MWPS scheme to acceptable levels. We argue that the existence of multiple dissipation-regulation mechanisms in the MWPS scheme must be construed as an excel-

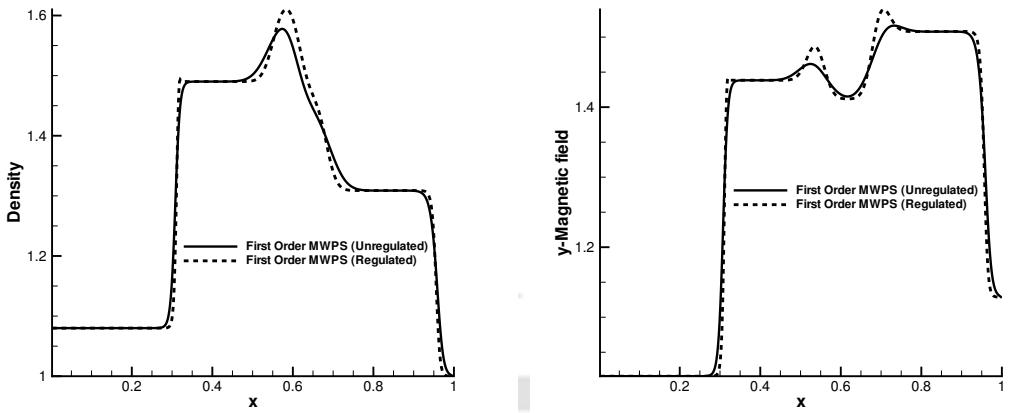

Figure 3.18. Solutions for Ryu and Jones problem 2a (first-order MWPS with regulated ϕ and ψ vs first-order MWPS with $\phi = \psi = 1$)

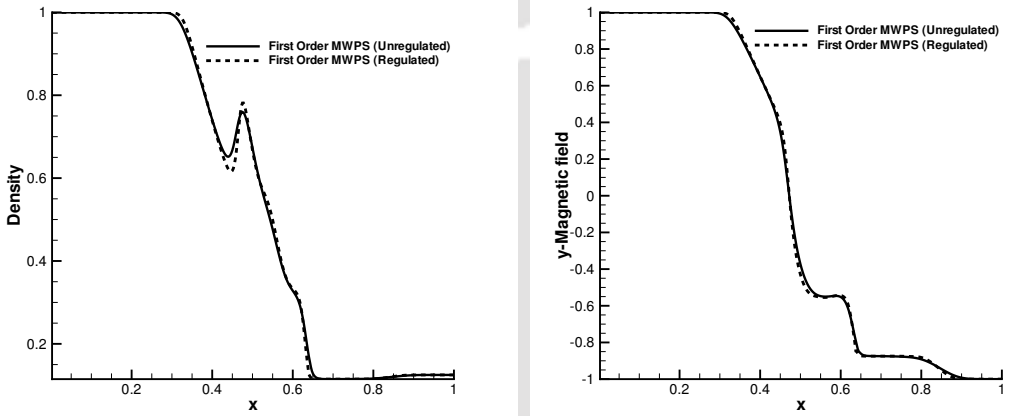

Figure 3.19. Solutions for Brio-Wu problem (first-order MWPS with regulated ϕ and ψ vs first-order MWPS with $\phi = \psi = 1$)

lent opportunity to devise nearly "optimally-dissipative" schemes, particularly for MHD.

To summarise, the MWPS scheme is a wave-particle splitting scheme with a central-upwind character that does not require characteristic decomposition. This leads to simple flux formulae which involve no tedious calculations as in Riemann solvers, and at the same time leaves no room for an explicit regulation of the added numerical dissipation. The three-part flux splitting that forms the basis of the MWPS scheme may be interpreted physically as well. The fluid particles propagate along particle lines with the flow speed (particle-like

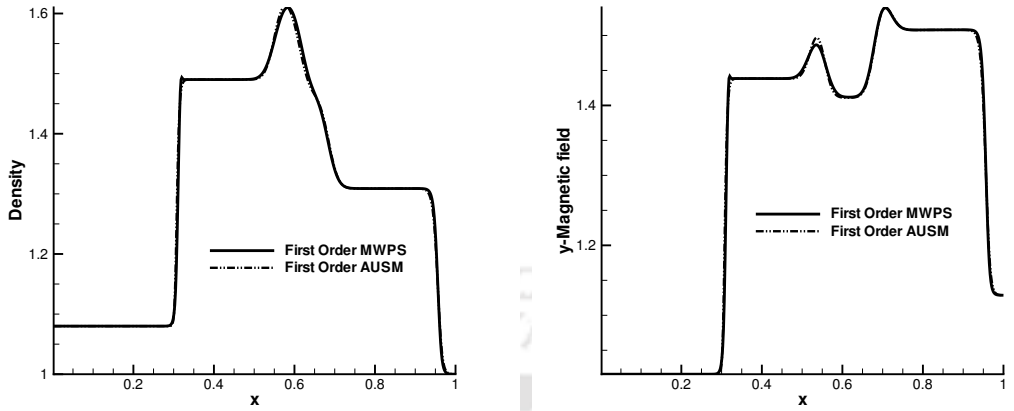

Figure 3.20. Comparison of density and y-magnetic field profiles obtained by first-order MWPS with regulated ϕ and ψ and by first-order AUSM for Ryu and Jones problem 2a

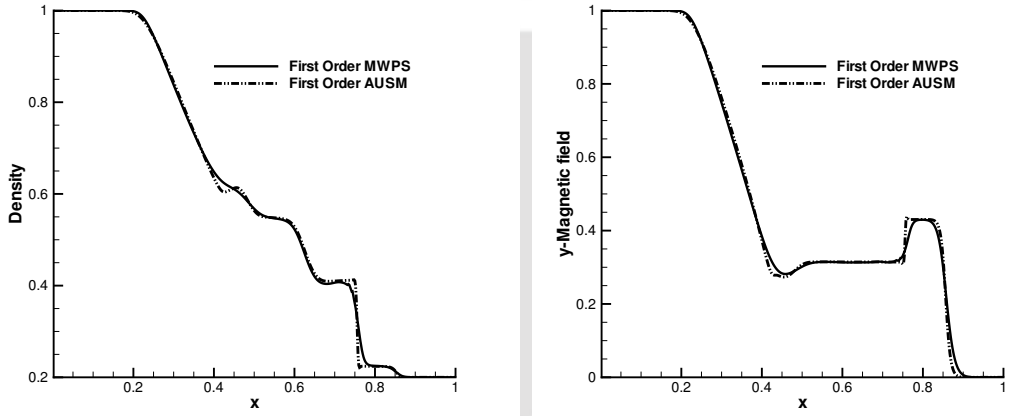

Figure 3.21. Comparison of density and y-magnetic field profiles obtained by first-order MWPS with regulated ϕ and ψ and by first-order AUSM for Ryu and Jones problem 4a

behaviour) while undergoing dilatation in the presence of magnetic field leading to magneto-acoustic and Alfvén waves (wave-like behaviour). By employing a limited least-squares reconstruction and with the additional freedom to control numerical diffusion, the MWPS scheme is a robust and accurate numerical flux scheme for MHD flows. The MWPS scheme is a promising alternative to other flux schemes employed in MHD of the same class such as the AUSM as well as central-upwind schemes and approximate Riemann solvers.

4

Wave-particle splitting for two-dimensional ideal MHD

In this chapter, we attempt to extend the Magneto-acoustic Wave Particle Splitting (MWPS) scheme to two-dimensional (2D) ideal MHD flows. Unlike the one-dimensional (1D) MHD equations where the divergence-free constraint of the magnetic field ($\nabla \cdot \mathbf{B} = 0$) is automatically satisfied, one needs to take special attention to satisfy this constraint in 2D simulations. The effect of non-zero divergence of the magnetic field are highlighted and the Artificial Compressibility Analogy (ACA) method of Yalim [1] is implemented with a dual time-stepping strategy to clean divergence errors. A nominally second-order accurate 2D flow solver for MHD is proposed and its accuracy and robustness for canonical MHD problems in multi-dimensions is demonstrated both on structured and unstructured grids.

4.1 The flux vector decomposition for 2D MWPS

The 2D ideal MHD equations in conservative form can be written as,

$$\frac{\partial \mathbf{U}}{\partial t} + \frac{\partial \mathbf{F}}{\partial x} + \frac{\partial \mathbf{G}}{\partial y} = 0 \tag{4.1}$$

where $\mathbf{U}$ is the vector of conserved variables, $\mathbf{F}$ and $\mathbf{G}$ are flux vectors in x- and y-directions, respectively. On a typical 2D unstructured mesh (See Figure 4.1 for a single volume and notations), the semi-discrete form of the ideal MHD equations in the finite volume framework maybe derived as,

$$\frac{\partial \mathbf{U}_k}{\partial t} = -\frac{1}{\Omega_k} \sum_m \mathbf{F}_\perp^m \Delta s^m \tag{4.2}$$

where k denotes the cell and m the faces (edges in 2D) of the k^{th} cell. The quantities $\mathbf{F}_\perp^m$ and Δs^m are the normal flux and the area of the m^{th} face. For any face the normal flux is calculated as,

$$\mathbf{F}_\perp = n_x \mathbf{F} + n_y \mathbf{G} \tag{4.3}$$

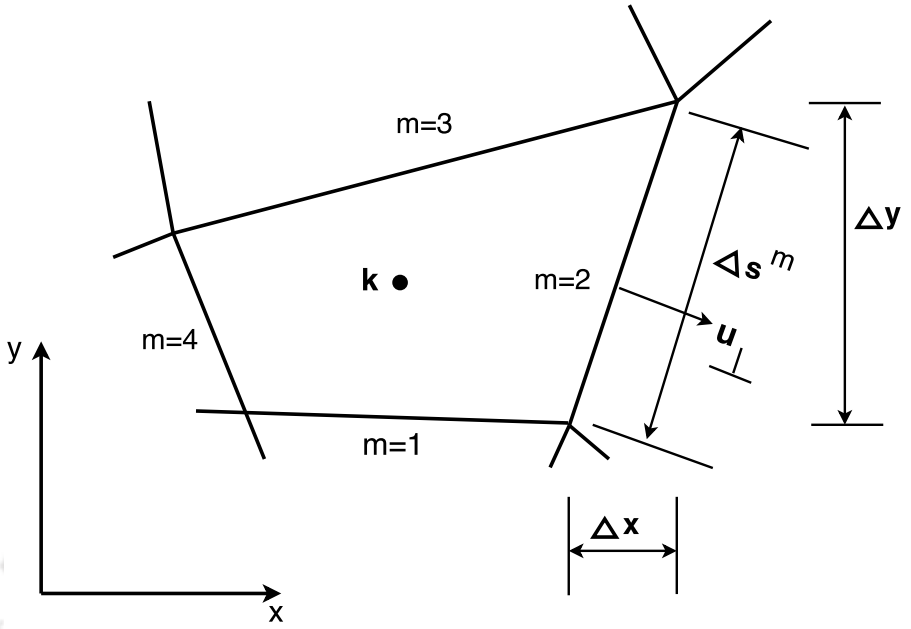

Figure 4.1. A typical two-dimensional finite volume

where $n_x = \frac{\Delta y}{\Delta s}$ and $n_y = -\frac{\Delta x}{\Delta s}$ represent the direction cosines of the unit normal $\hat{n}$ to the interface. The normal flux vector $\mathbf{F}_\perp$ can be cast as,

$$\mathbf{F}_\perp = \begin{bmatrix} \rho u_\perp \\ \rho u u_\perp - B_x B_\perp + n_x(P + \frac{1}{2}B^2) \\ \rho v u_\perp - B_y B_\perp + n_y(P + \frac{1}{2}B^2) \\ \rho w u_\perp - B_z B_\perp \\ B_x u_\perp - u B_\perp \\ B_y u_\perp - v B_\perp \\ B_z u_\perp - w B_\perp \\ (E + P + \frac{1}{2}B^2)u_\perp - B_\perp(uB_x + vB_y + wB_z) \end{bmatrix} \tag{4.4}$$

where $u_\perp$ and $B_\perp$ are the normal components of velocity and magnetic field at the cell face respectively and are given by

$$u_\perp = u n_x + v n_y \tag{4.5}$$

$$B_\perp = B_x n_x + B_y n_y \tag{4.6}$$

Following the MWPS methodology described in the previous chapter, the normal flux vector $\mathbf{F}_\perp$ is split into three distinct parts as follows.

$$\mathbf{F}_\perp = \underbrace{\begin{bmatrix} \rho u_\perp \\ \rho u u_\perp \\ \rho v u_\perp \\ \rho w u_\perp \\ B_x u_\perp \\ B_y u_\perp \\ B_z u_\perp \\ E u_\perp \end{bmatrix}}_{\mathbf{F}^t_\perp} + \underbrace{\begin{bmatrix} 0 \\ (\gamma-1)[E-\frac{1}{2}\rho V^2]n_x \\ (\gamma-1)[E-\frac{1}{2}\rho V^2]n_y \\ 0 \\ 0 \\ 0 \\ 0 \\ (\gamma-1)[E-\frac{1}{2}\rho V^2]u_\perp \end{bmatrix}}_{\mathbf{F}^p_\perp} + \underbrace{\begin{bmatrix} 0 \\ (1-\frac{\gamma}{2})B^2 n_x - B_x B_\perp \\ (1-\frac{\gamma}{2})B^2 n_y - B_y B_\perp \\ -B_z B_\perp \\ -uB_\perp \\ -vB_\perp \\ -wB_\perp \\ (1-\frac{\gamma}{2})B^2 u_\perp - B_\perp(uB_x + vB_y + wB_z) \end{bmatrix}}_{\mathbf{F}^m_\perp} \tag{4.7}$$

The first part called the transport part and denoted by $\mathbf{F}^t_\perp$ represents the convection or transport of quantities by the flow velocity. The second part, $\mathbf{F}^p_\perp$ is the pressure part since it contains terms pertaining to the total pressure. The third part, represented as $\mathbf{F}^m_\perp$ consists of the remaining terms and is called the magnetic part since it contains terms corresponding to the magnetic field components. In the following sections, we describe the treatment of each of these individual flux vectors in two-dimensions.

4.2 Treatment of the transport flux vector

The transport fluxes in two-dimensions are treated similar to the transport fluxes in 1D MWPS. The calculation of the interfacial fluxes is based on the principle of upwinding where the sign of the interfacial Mach number $M_\perp$ is employed. The interfacial Mach number is now calculated based on the normal velocity as,

$$M_\perp = \frac{u_\perp}{a_0} \tag{4.8}$$

where $a_0 = \sqrt{a^2 + b^2}$, $a^2 = \frac{\gamma P}{\rho}$ and, $b^2 = \frac{B^2}{\rho}$. The discrete fluxes for the transport part may then be computed as,

$$\mathbf{F}^t_\perp = \begin{bmatrix} \rho u_\perp \\ \rho u u_\perp \\ \rho v u_\perp \\ \rho w u_\perp \\ B_x u_\perp \\ B_y u_\perp \\ B_z u_\perp \\ E u_\perp \end{bmatrix} = M^\pm_{\perp_{1/2}} \begin{bmatrix} \rho a_0 \\ \rho u a_0 \\ \rho v a_0 \\ \rho w a_0 \\ B_x a_0 \\ B_y a_0 \\ B_z a_0 \\ E a_0 \end{bmatrix}_{\mathrm{L/R}} \tag{4.9}$$

where L and R are the left and right states which are obtained using a constant/linear reconstruction. The interfacial Mach number, that determines the

upwind direction is computed as,

$$M^{\pm}_{\perp_{1/2}} = \frac{1}{2}(M_{\perp_{\mathrm{L/R}}} \pm |M_{\perp_{\mathrm{L/R}}}|) \tag{4.10}$$

4.3 Treatment of the pressure flux vector

The construction of the pressure flux vector also follows the same philosophy as in the 1D case. The pressure fluxes which consist of both the thermal and magnetic pressures show a "wave-like" behaviour as can be observed from the eigenvalues of the flux Jacobian (See Appendix A.5). The eight eigenvalues are 0 (with multiplicity of 6) and $\pm\sqrt{\frac{\gamma-1}{\gamma}}a^*$, where a^* denotes the magneto-acoustic speed defined by,

$$a^* = \sqrt{a^2 + \frac{\gamma(\gamma-1)}{2}b^2} \tag{4.11}$$

We split the fluxes left-running and right-running waves based on the signs of the eigenvalues of the flux Jacobian $\mathbf{A}^p_\perp$. The Jacobian matrix may be diagonalised as,

$$\mathbf{A}^p_\perp = \mathbf{R}_\perp \mathbf{\Lambda}^p_\perp \mathbf{R}^{-1}_\perp \tag{4.12}$$

like in the 1D MWPS, where $\mathbf{R}_\perp$ is the matrix of right eigenvectors and $\mathbf{\Lambda}^p_\perp$ is the matrix of the eigenvalues of the flux Jacobian of $\mathbf{F}^p_\perp$. We then split the Jacobian into two parts, one consisting of positive eigenvalues and the other consisting of negative eigenvalues by splitting the eigenvalue matrix as,

$$\mathbf{\Lambda}^{p\,\pm}_\perp = \frac{\mathbf{\Lambda}^p_\perp \pm |\mathbf{\Lambda}^p_\perp|}{2} \tag{4.13}$$

where $\mathbf{\Lambda}^{p\,\pm}_\perp$ are given by,

$$\mathbf{\Lambda}^{p\,+}_\perp = \sqrt{\frac{\gamma-1}{\gamma}} \begin{bmatrix} \phi a^* & 0 & 0 & 0 & 0 & 0 & 0 & 0 \\ 0 & \phi a^* & 0 & 0 & 0 & 0 & 0 & 0 \\ 0 & 0 & \phi a^* & 0 & 0 & 0 & 0 & 0 \\ 0 & 0 & 0 & \phi a^* & 0 & 0 & 0 & 0 \\ 0 & 0 & 0 & 0 & \phi a^* & 0 & 0 & 0 \\ 0 & 0 & 0 & 0 & 0 & \phi a^* & 0 & 0 \\ 0 & 0 & 0 & 0 & 0 & 0 & 0 & 0 \\ 0 & 0 & 0 & 0 & 0 & 0 & 0 & a^* \end{bmatrix} \tag{4.14}$$

$$\mathbf{\Lambda}^{p\,-}_\perp = \sqrt{\frac{\gamma-1}{\gamma}} \begin{bmatrix} -\phi a^* & 0 & 0 & 0 & 0 & 0 & 0 & 0 \\ 0 & -\phi a^* & 0 & 0 & 0 & 0 & 0 & 0 \\ 0 & 0 & -\phi a^* & 0 & 0 & 0 & 0 & 0 \\ 0 & 0 & 0 & -\phi a^* & 0 & 0 & 0 & 0 \\ 0 & 0 & 0 & 0 & -\phi a^* & 0 & 0 & 0 \\ 0 & 0 & 0 & 0 & 0 & -\phi a^* & 0 & 0 \\ 0 & 0 & 0 & 0 & 0 & 0 & -a^* & 0 \\ 0 & 0 & 0 & 0 & 0 & 0 & 0 & 0 \end{bmatrix} \tag{4.15}$$

where every zero eigenvalue is split as a sum of ϕa^* and $-\phi a^*$. The split Jacobians are then easily derived as,

$$\mathbf{A}_{\perp}^{p\,\pm} = \mathbf{R}_{\perp}\mathbf{\Lambda}_{\perp}^{p\,\pm}\mathbf{R}_{\perp}^{-1} \tag{4.16}$$

The fluxes $\mathbf{F}_{\perp}^{p\,+}$ and $\mathbf{F}_{\perp}^{p\,-}$ are then constructed based on the homogeneity property as,

$$\mathbf{F}_{\perp}^{p\,\pm} = \mathbf{A}_{\perp}^{p\,\pm}\mathbf{U} = (\mathbf{R}_{\perp}\mathbf{\Lambda}_{\perp}^{p\,\pm}\mathbf{R}_{\perp}^{-1})\mathbf{U} \tag{4.17}$$

The components of $\mathbf{F}_{\perp}^{p\,+}$ are backward differenced and those of $\mathbf{F}_{\perp}^{p\,-}$ are forward differenced. The split pressure fluxes read,

$$\mathbf{F}_{\perp}^{p\,\pm} = \begin{bmatrix} \pm\sqrt{\frac{\gamma-1}{\gamma}}\phi a^*\rho \\ \frac{Pn_x}{2} + \frac{\gamma-1}{4}B^2 n_x \pm \sqrt{\frac{\gamma-1}{\gamma}}\phi a^*\rho u \\ \frac{Pn_y}{2} + \frac{\gamma-1}{4}B^2 n_y \pm \sqrt{\frac{\gamma-1}{\gamma}}\phi a^*\rho v \\ \pm\sqrt{\frac{\gamma-1}{\gamma}}\phi a^*\rho w \\ \pm\sqrt{\frac{\gamma-1}{\gamma}}\phi a^* B_x \\ \pm\sqrt{\frac{\gamma-1}{\gamma}}\phi a^* B_y \\ \pm\sqrt{\frac{\gamma-1}{\gamma}}\phi a^* B_z \\ \frac{Pu_{\perp}}{2} + \frac{\gamma-1}{4}u_{\perp}B^2 \pm \frac{Pa^*}{2\sqrt{\gamma(\gamma-1)}} \pm \sqrt{\frac{\gamma-1}{\gamma}}\phi a^*\frac{\rho V^2}{2} \pm \sqrt{\frac{\gamma-1}{\gamma}}\frac{B^2 a^*}{4} \end{bmatrix} \tag{4.18}$$

A sample script (using MATHEMATICA [77]) to calculate the eigen-structure of the flux Jacobian $\mathbf{A}_{\perp}^{p}$ as well as the positive split pressure fluxes $\mathbf{F}_{\perp}^{p\,+}$ are given in Appendix A.7.

4.4 Treatment of the magnetic flux vector

The treatment of the magnetic flux vector in 2D follows, in principle, the ideas from its 1D counterpart. We treat the magnetic flux vector using a central scheme since the flux Jacobian $\mathbf{A}_{\perp}^{m}$ is defective and does not obey homogeneity property. However, the eigenvalues of $\mathbf{A}_{\perp}^{m}$ do not reduce to simplified expressions which makes finding the spectral radius a non-trivial task. We believe that this difficulty stems from the presence of the additional equation for B_x (fifth equation) in two dimensions and resolve this issue by further splitting $\mathbf{F}_{\perp}^{m}$ into two parts as described below.

$$\mathbf{F}_{\perp}^{m} = \underbrace{\begin{bmatrix} 0 \\ (1-\frac{\gamma}{2})B^2 n_x - B_x B_\perp \\ (1-\frac{\gamma}{2})B^2 n_y - B_y B_\perp \\ -B_z B_\perp \\ 0 \\ 0 \\ -wB_\perp \\ (1-\frac{\gamma}{2})B^2 u_\perp - B_\perp(uB_x + vB_y + wB_z) \end{bmatrix}}_{\mathbf{F}_{\perp 1}^{m}} + \underbrace{\begin{bmatrix} 0 \\ 0 \\ 0 \\ 0 \\ -uB_\perp \\ -vB_\perp \\ 0 \\ 0 \end{bmatrix}}_{\mathbf{F}_{\perp 2}^{m}} \tag{4.19}$$

A closer look at the bipartite splitting in Eq. (4.19) shows that only the terms appearing in the B_y and B_z equations (sixth and seventh respectively) have non-zero values in both the parts. The eigen-structure of the flux Jacobians $\mathbf{A}_{\perp 1}^{m} = \frac{\partial \mathbf{F}_{\perp 1}^{m}}{\partial \mathbf{U}}$ and $\mathbf{A}_{\perp 2}^{m} = \frac{\partial \mathbf{F}_{\perp 2}^{m}}{\partial \mathbf{U}}$ are detailed in Appendix A.6. It suffices to mention here that the eight eigenvalues of $\mathbf{A}_{\perp 1}^{m}$ are 0 (with multiplicity of 6) and $\pm\frac{B_\perp}{\sqrt{\rho}}$ and, those of $\mathbf{A}_{\perp 2}^{m}$ are 0 (with multiplicity of 7) and $-u_\perp$. Adopting the local Lax-Friedrichs (LLF) scheme to treat the magnetic flux vector as in the 1D case, we obtain

$$\mathbf{F}_{\perp 1}^{m} = \frac{1}{2}\left(\mathbf{F}_{\perp 1_{\mathrm{L}}}^{m} + \mathbf{F}_{\perp 1_{\mathrm{R}}}^{m}\right) - \frac{1}{2}\lambda_{max1}\left(\mathbf{U}_{\mathrm{R}} - \mathbf{U}_{\mathrm{L}}\right) \tag{4.20}$$

$$\mathbf{F}_{\perp 2}^{m} = \frac{1}{2}\left(\mathbf{F}_{\perp 2_{\mathrm{L}}}^{m} + \mathbf{F}_{\perp 2_{\mathrm{R}}}^{m}\right) - \frac{1}{2}\lambda_{max2}\left(\mathbf{U}_{\mathrm{R}} - \mathbf{U}_{\mathrm{L}}\right) \tag{4.21}$$

where λ_{max1} and λ_{max2} are the largest eigenvalues (spectral radius) of the corresponding flux Jacobians which are respectively $\frac{B_\perp}{\sqrt{\rho}}$ and $u_\perp$.

4.5 Achieving second-order accuracy

While second-order accurate MWPS was realised using SDWLS in 1D (See Chapter 3, Section 3.6.1), we adopt a more traditional approach for 2D MHD. The states ($\mathbf{U}_L$ and $\mathbf{U}_R$) on the left and right side of any interface are obtained from the cell-averaged values in the cells sharing the face. We employ a limited linear reconstruction based on primitive values for this purpose. This means that for a face f shared by cells i and j (as shown in Figure 4.2), one can obtain the reconstructed values of the vector of primitive variables V at the left and right of the face f as,

$$\mathbf{V}_L = \mathbf{V}_i + \phi_i \, \nabla\mathbf{V}_i \cdot (\mathbf{r}_f - \mathbf{r}_i) \tag{4.22}$$

$$\mathbf{V}_R = \mathbf{V}_j + \phi_j \, \nabla\mathbf{V}_j \cdot (\mathbf{r}_f - \mathbf{r}_j) \tag{4.23}$$

where $\mathbf{V} = [\rho \; u \; v \; w \; B_x \; B_y \; B_z \; P]^T$ and the values at i and j must be interpreted as cell-averaged values lumped at the cell centers. Also, the quantities $\mathbf{r}_f$, $\mathbf{r}_i$ and

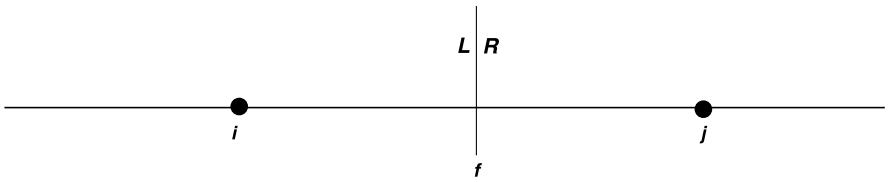

Figure 4.2. Left and right states of a face. The face f is shared by two cells (not shown here) whose centroids are defined by i and j

$\mathbf{r}_j$ denote the position vectors of the face-center and cell-centers of cells i and j respectively. The quantity ϕ appearing in Eqs. (4.22) and (4.23) is referred to as the slope limiter and limits the gradients to enforce monotonicity. In the subsections below, we shall discuss briefly the gradient computation and slope limiting approaches adopted in this work as part of the MHD solver development.

4.5.1 Gradient computation

Unlike the 1D solver where the weighted least-squares approach was adopted, we employ the Green-Gauss reconstruction [78,79] to calculate centroidal gradients. The first derivatives of any primitive variable V at the cell center of any cell c may be found as,

$$(\nabla V)_c = \frac{1}{\Omega_c} \sum_{f \in c} V_f \mathbf{n}_f \Delta S_f \tag{4.24}$$

where V_f is the value at the face center and $\mathbf{n}_f$ represents the unit normal to the face. The summation is over the faces constituting the cell (or volume) c where the gradients are desired. While there are different possible choices for V_f, we obtain the face-center values by simple averaging the cell-center values of the cell c and the considered face-sharing neighbour.

4.5.2 Slope limiting

The gradients obtained using the Green-Gauss reconstruction must be "limited" to ensure a monotone scheme devoid of undershoots/overshoots. This is realised by multiplying the gradients by a parameter ϕ (referred to as the limiting parameter) which is obtained in the following manner.

$$\phi_c = \begin{cases} \psi\left(\dfrac{V_{max,C\&N} - V_c}{\nabla V|_c \cdot (\mathbf{r}_f - \mathbf{r}_c)}\right), & \text{if } \nabla V|_c \cdot (\mathbf{r}_f - \mathbf{r}_c) > 0 \\ \psi\left(\dfrac{V_{min,C\&N} - V_c}{\nabla V|_c \cdot (\mathbf{r}_f - \mathbf{r}_c)}\right), & \text{if } \nabla V|_c \cdot (\mathbf{r}_f - \mathbf{r}_c) < 0 \\ 1, & \text{if } \nabla V|_c \cdot (\mathbf{r}_f - \mathbf{r}_c) = 0 \end{cases}$$

where $V_{max,C\&N}$ and $V_{min,C\&N}$ are the maximum and minimum values of the primitive variable V among cell c and all its neighbours N. It must be emphasised

that N refers to the neighbourhood which consists of the set of all cells that share a face with c. The limiter function ψ is defined by,

$$\psi(y) = \frac{y^2 + 2y}{y^2 + y + 2}.$$

In order to avoid the oscillations in the near-constant regions $\psi(y)$ is modified for the case where $\nabla V|_c \cdot (\mathbf{r}_f - \mathbf{r}_c) > 0$. Defining the terms in the numerator and denominator of the argument of ψ as Δ^+ and Δ^-, respectively, we can recast ψ as

$$\psi\left(\frac{\Delta^+}{\Delta^-}\right) = \frac{(\Delta^+)^2 + 2\Delta^+\Delta^- + \eta}{(\Delta^+)^2 + \Delta^+\Delta^- + 2(\Delta^-)^2 + \eta}$$

The quantity η is chosen equal to 10^{-8} and is a small parameter to avoid division by zero and to prevent the limiter from leading anomalous values in near-constant zones where Δ^+ and Δ^- are very small.

It must be remarked again that the limited reconstruction is carried out on primitive variables and not the conserved variables. Our experience shows that the latter leads to convergence difficulties which have also been previously reported in literature. During our numerical experiments, we also encountered another common problem which is loosely known as "limiter chatter" and refers to the hampering of steady-state convergence with the residual tending to saturate after a certain number of iterations. This occurs mainly in simulations where shocks and discontinuities are present and is clearly unavoidable in compressible MHD flows. To mitigate this problem, we employ the idea of "freezing" the limiter, where the limiter value ϕ (corresponding to all primitive variables for a cell) is frozen after an user-defined iteration. The user has to be careful in selecting the opportune moment to freeze the limiter, since it has to be necessarily before convergence hampering sets in. If at iteration n the simulation is free of convergence hampering, then we can use (corresponding to each primitive variable),

$$\phi_c^{n+i} = \phi_c^n \quad \text{for} \quad i = 1, 2, 3...$$

4.6 Enforcing the solenoidality constraint

As discussed in Chapter 2, one of the major challenges faced in multi-dimensional MHD is the need to satisfy the solenoidality constraint defined by $\nabla \cdot \mathbf{B} = 0$. We employ in this work, the Artificial Compressibility Approach (ACA) proposed by Yalim et al. [1] which may be considered as a special case of the more general hyperbolic divergence cleaning (HDC) methods. The ACA method has been found to perform quite well for MHD flows on structured grids and we attempt to extend this idea with MWPS scheme for two-dimensional MHD on arbitrary

polygonal meshes.

Referring to Section 2.5.5 where the philosophy of ACA is described, it is clear that an additional equation for the scalar potential ϕ needs to be solved. This means that the solution vector now has nine unknowns as opposed to eight and the fluxes for the magnetic field equations are now influenced by this scalar potential. Since the scalar potential for MHD flows is akin to pressure in incompressible flows and is employed to enforce the solenoidality constraint, it does not qualify as a conserved variable. Clearly, the derivation of the scalar potential equation has no truly physical basis and therefore we solve this equation *separately* from the remaining eight equations. In this work, we therefore solve the eight equations using the MWPS scheme with the equation for scalar potential solved using a more diffusive local Lax-Friedrichs scheme (LLF) following the recommendations in [1]. In solving these equations, the temporal discretisation is also equally important. While temporal accuracy holds no significance for steady-state problems, it is quite important in unsteady flows which is encountered for the larger part of the work. Furthermore, for multi-dimensional MHD, one would require the solenoidality constraint to be satisfied only at steady-state for such problems while they need to be enforced at every time step in case of unsteady MHD flows. This constitutes a non-trivial challenge and we shall show later in this chapter that neglecting this aspect could lead to physically anomalous solutions.

For one-dimensional MHD flows, we adopted an explicit Euler time-stepping scheme which is only first-order accurate in time. While higher-order temporal accuracy can be realised in an explicit approach by adopting a multi-stage RK scheme (RK-3 or RK-4), our studies which employed a sufficiently smaller time step showed that the results were quite accurate indicating that the temporal errors were not too large. In the 2-D studies discussed herein, we employ the first-order explicit Euler scheme for steady MHD problems. The discrete form of the governing equations then read,

$$\underbrace{\frac{\mathbf{U}^{n+1}-\mathbf{U}^{n}}{\Delta\tau}}_{\text{Euler explicit}}+\frac{1}{\Omega}\sum_{m}\mathbf{F}_{\perp}^{n}\Delta s=0 \tag{4.25}$$

where, m is the interface index of the cell and n denotes the time step. It must be noted that $\mathbf{U}$ includes all nine variables, including the scalar potential, although the flux scheme for the last equation is different to those of the other eight. Clearly, as the solutions converge to steady-state, the last equation (corresponding to scalar potential) reduces to the solenoidality constraint. For unsteady

problems, we propose the following time discretisation.

$$\underbrace{\frac{\mathbf{U}^{k+1}-\mathbf{U}^{k}}{\Delta\tau}}_{\text{Euler explicit}}+\underbrace{\frac{3\mathbf{U}^{k+1}-4\mathbf{U}^{n}+\mathbf{U}^{n-1}}{\Delta t}}_{\text{BDF}}+\frac{1}{\Omega}\sum_{m}\mathbf{F}_{\perp}^{k}\Delta s=0 \tag{4.26}$$

In this equation k denotes the sub-iteration and n represents the time level. Seen differently, k denotes pseudo-time level and n denotes the physical (or "true") time level and one simply solves a steady-state problem in pseudo-time at each real time step. Thus, one solves the discrete system of equations represented by Eq. (4.26) for a finite number of sub-iterations at the end of which, assuming convergence,

$$\mathbf{U}^{k+1}\approx\mathbf{U}^{k}=\mathbf{U}^{n+1}. \tag{4.27}$$

This idea, referred to as dual-time (or pseudo-time) stepping helps to effectively employ convergence acceleration techniques used for steady flows in an unsteady setting without compromising on the temporal accuracy. In the context of MHD flows, this idea is even more important, since it is critical to preservation of the zero magnetic divergence. This is implemented by assuming $\Delta t\to\infty$ in the ninth equation (for scalar potential) that amounts to only retaining the pseudo-time derivative. With this modification, where the physical time derivative is dropped the evolution equation for ϕ becomes,

$$\frac{U_{9}^{k+1}-U_{9}^{k}}{\Delta\tau}+\frac{1}{\Omega}\sum_{m}F_{\perp_{9}}^{k}\Delta s=0 \tag{4.28}$$

The implementation aspects in the dual-time stepping approach outlined here which are critical in reducing the divergence errors include the choice of the physical and dual time steps as well as the number of sub-iterations. We choose $\Delta\tau=\Delta t$ for our simulations while the number of iterations is a trade-off between the computational cost and divergence errors. It must be remarked that the divergence errors cannot be avoided in a numerical framework and the ACA does the job of "cleaning" these errors. The ACA is therefore referred to as a variant of "divergence-cleaning" methods and the extent to which the divergence errors decreases will depend on the number of sub-iterations. In Section 4.9, we shall numerically illustrate the need for and importance of the sub-iterations and the dual time-stepping strategy and it suffice to mention here that around 200 sub-iterations are necessary to ensure robust and accurate solutions in 2D MHD simulations in this work.

4.7 Computation of divergence error

In the ACA method, the solenoidality constraint is coupled with the ideal MHD equations through an artificial evolution equation for ϕ as shown in Eq. (2.46).

The flux function for the extra equation is $V_{ref}^2 \nabla \cdot \mathbf{B}$. When Eq. (4.28) converges to steady-state (in pseudo/real time), the temporal part vanishes, implying that the local flux contributions in each cell also tend to zero. Thus $\nabla \cdot \mathbf{B}$ errors can be calculated by summing the numerical flux calculations of the ninth equation over all the faces of the cell. In our computations, we implement the LLF scheme for calculation of the fluxes in the scalar potential (9^{th}) equation. Thus, the magnetic divergence errors for a cell are determined as,

$$(\nabla \cdot \mathbf{B})_c = \frac{1}{V_{ref}^2 \Omega_c} \sum_m \left[\frac{V_{ref}^2}{2} (B_{\perp \mathrm{L}}^{\ m} + B_{\perp \mathrm{R}}^{\ m}) - \frac{1}{2} \lambda_{max} (\phi_\mathrm{R} - \phi_\mathrm{L}) \right] \Delta s^m \qquad (4.29)$$

where the summation is over all faces of the cell c. It is important to realise that the divergence errors cannot be lesser than the algebraic iterative errors that are incurred during the steady-state convergence, either in physical or pseudo time, for the steady and unsteady problems respectively. In all studies to follow, we compute the L_2 and L_∞ norms of the divergence error to evaluate the efficacy of the ACA approach in conjunction with the dual time-stepping strategy.

4.8 Boundary conditions

An important aspect to the solution of hyperbolic conservation laws is the implementation of boundary conditions (BCs). The various BCs encountered in 2D MHD problems in this work include superfast inlet, superfast outlet, perfectly conducting wall and periodic boundary conditions.

Superfast inlet This boundary condition is implemented by constructing a fictitious (or ghost) cell G where the states are defined by,

$$\begin{pmatrix} \rho_G \\ (\rho \mathbf{V})_G \\ \mathbf{B}_G \\ E_G \\ \phi_G \end{pmatrix} = \begin{pmatrix} 2\rho_\infty - \rho_B \\ 2(\rho \mathbf{V})_\infty - (\rho \mathbf{V})_B \\ 2\mathbf{B}_\infty - \mathbf{B}_B \\ 2E_\infty - E_B \\ 2\phi_\infty - \phi_B \end{pmatrix} \qquad (4.30)$$

In the above equation ∞ refers to the freestream conditions and B denotes the cell in the domain shared by the boundary face. The extrapolation of the cell and freestream values defines the state at the ghost cell. The two states at cells B and G are then used in the flux formula to compute the fluxes at the face.

Superfast outlet For the superfast outlet boundary condition, all variables in the cell shared by the face are simply extrapolated to the face except the scalar potential. The latter is given a Dirichlet boundary condition and for all studies in this work we take $\phi = 0$ at the outlet faces.

Perfectly conducting wall This boundary condition is also enforced using the concept of a ghost cell G where the states are obtained as,

$$\begin{aligned}
\rho_G &= \rho_B \\
(\rho u)_G &= (\rho u)_B - 2((\rho \mathbf{V})_B \cdot \mathbf{n}_{BG})(n_x)_{BG} \\
(\rho v)_G &= (\rho v)_B - 2((\rho \mathbf{V})_B \cdot \mathbf{n}_{BG})(n_y)_{BG} \\
(\rho w)_G &= (\rho w)_B - 2((\rho \mathbf{V})_B \cdot \mathbf{n}_{BG})(n_z)_{BG} \\
(B_x)_G &= (B_x)_B - 2(\mathbf{B}_B \cdot \mathbf{n}_{BG})(n_x)_{BG} \\
(B_y)_G &= (B_y)_B - 2(\mathbf{B}_B \cdot \mathbf{n}_{BG})(n_y)_{BG} \\
(B_z)_G &= (B_z)_B - 2(\mathbf{B}_B \cdot \mathbf{n}_{BG})(n_z)_{BG} \\
E_G &= E_B \\
\phi_G &= \phi_B
\end{aligned} \tag{4.31}$$

where $\mathbf{n}_{BG}$ is the outward pointing unit normal of the B–G interface pointing from the boundary cell to the ghost cell. This effectively mirrors the velocity and magnetic fields so that the normal velocity and magnetic field on the boundaries are zero, in a weak sense.

Periodic In case of periodic boundary conditions, one employs the same flux formula as for interior faces, however with both states obtained from cells in the domain. This is best understood by realising that faces with the periodic BC come in pairs. For any face f on an periodic boundary, there exists a paired face $\tilde{f}$. While these faces are indeed physically different, they are essentially the "same face" as far as the boundary condition implementation is concerned. Thus, the state of cells for the faces f and $\tilde{f}$ (which are physically different cells in the domain) are used to compute the fluxes for both the faces. Clearly, the fluxes at the faces f and $\tilde{f}$ are identical, which is essentially dictated by the periodic nature of the boundary condition.

4.9 Results and discussion

The proposed MWPS scheme for 2D MHD flows is tested on different benchmark problems to evaluate its ability to handle complex flow features in MHD flows. These include 2D variants of some 1D problems discussed in Chapter 3 as well as genuinely 2D MHD test cases. The in-house 2D flow solver is based on the finite volume method and can handle both structured and unstructured meshes. A steady MHD problem and several unsteady benchmark tests are simulated to evaluate the performance of the proposed numerical scheme. It must be recalled that the flow solver is nominally second-order in space, which is obtained using linear reconstruction in conjunction with Venkatakrishnan's (VK) limiter. The ACA approach to divergence cleaning is adopted with dual time-stepping to enforce solenoidality constraint $\nabla \cdot \mathbf{B} = 0$ for unsteady problems. The numerical

solutions from the present MHD flow solver are compared with computed results from other researchers to underscore the accuracy and versatility of the MWPS scheme.

4.9.1 Steady magnetic nozzle flow

The first test case is a steady-flow problem from [1] where a fully supersonic flow in a nozzle is considered. For reasons of symmetry, only one half of the domain is considered for computations. The profile of the upper wall is defined by the equation,

$$y(x) = H - I \sin^2\left(\frac{\pi x}{L}\right) \tag{4.32}$$

where $H = 3$, $I = 0.9$ and $L = 9$ are the inlet height, indentation and length of the nozzle, respectively. The superfast plasma at the inlet has $\rho = 1$, $u = 3$, $B_x = 1$ and $P = 1$. The value of V_{ref} is chosen as the inlet velocity itself which therefore equals 3. The ratio of specific heats is $\gamma = 1.4$. The superfast inlet BC is assigned at the left boundary (inlet) while the superfast outlet BC is used for the right boundary (outlet). The top and bottom walls are assumed to be perfectly conducting boundaries.

Since the flow is steady, a first-order temporal discretisation is used with $\Delta t = 10^{-4}$. The limiter is frozen after $2{\times}10^5$ iterations to avoid the convergence hampering (limiter-chatter) problem. The simulation is considered to be converged to steady state when the residual based on total energy $E \leq 10^{-6}$. Simulations are carried out with a structured mesh with 10800 quadrilaterals as well as a triangulated grid with 9084 triangles. These grids have approximately similar resolution, although the triangular mesh may be considered to be marginally coarser as compared to the structured mesh. The fast MHD shock and its reflection from the walls are well-resolved using the MWPS scheme on both meshes as can be seen from Figures 4.3 and 4.4, respectively which show the density contours. Figure 4.5 also shows the density distribution on the walls computed using the MWPS and LLF schemes on the structured mesh. It can be observed that the shock is quite accurately captured by both schemes, although LLF scheme is marginally more diffusive than the MWPS scheme. Figure 4.6 shows the convergence histories for both the schemes, wherein one can observe an oscillatory convergence to steady-state. This maybe attributed to the choice of a Dirichlet BC for the scalar potential and reflection of the $\nabla \cdot \mathbf{B}$ waves from the outlet. We must remark that the convergence was significantly hampered when the limiter was not "frozen". The simulations on unstructured meshes are also equally accurate and the results from the present MHD solver with MWPS scheme on the triangular mesh is compared with those from LLF and Roe scheme in [1] on an unstructured grid with nearly 5000 volumes. It is evident from the wall density distributions shown in Figure 4.7 that the present results are in good

agreement with those obtained using the Roe scheme in [1] with the LLF scheme exhibiting greater diffusion as expected. The residual convergence history for unstructured grids are similar to those of the structured counterpart and is not shown here for sake of brevity. It is also important to investigate the efficacy of the ACA approach in satisfying the solenoidality constraint for this test case. The contours of magnetic divergence are shown in Figure 4.8 and the largest (absolute) divergence errors are 7.46778×10^{-6}. This value is of the same order as the iterative errors (since the steady-state convergence is assumed when the energy residual is 10^{-6} or lower in the L_2 norm) and demonstrates that the ACA approach for steady MHD computations can reduce the divergence errors to values which are comparable to the tolerances set in the convergence criterion.

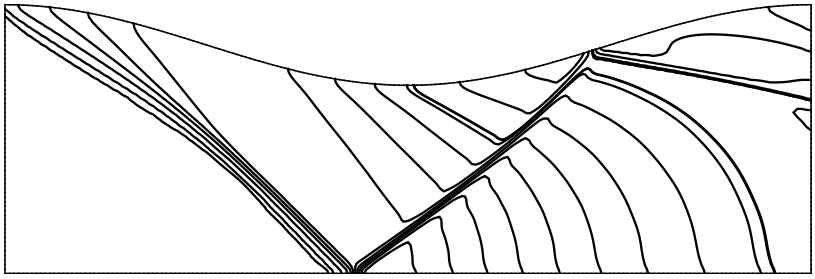

Figure 4.3. Density contours obtained by MWPS scheme for steady magnetic nozzle flow problem on a structured grid of 10800 quadrilaterals (Min: 0.522961, Δ: 0.173, Max: 2.77461)

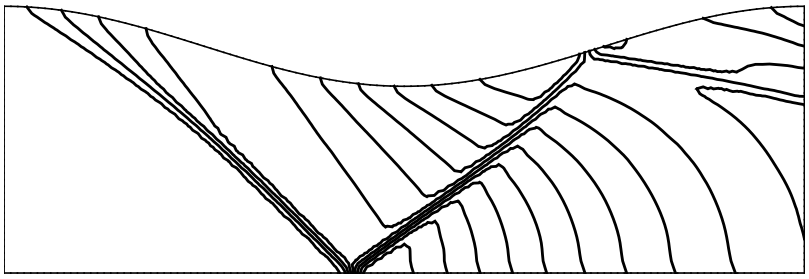

Figure 4.4. Density contours obtained by MWPS scheme for steady magnetic nozzle flow problem on an unstructured grid of 9084 triangles (Min: 0.522961, Δ: 0.173, Max: 2.77461)

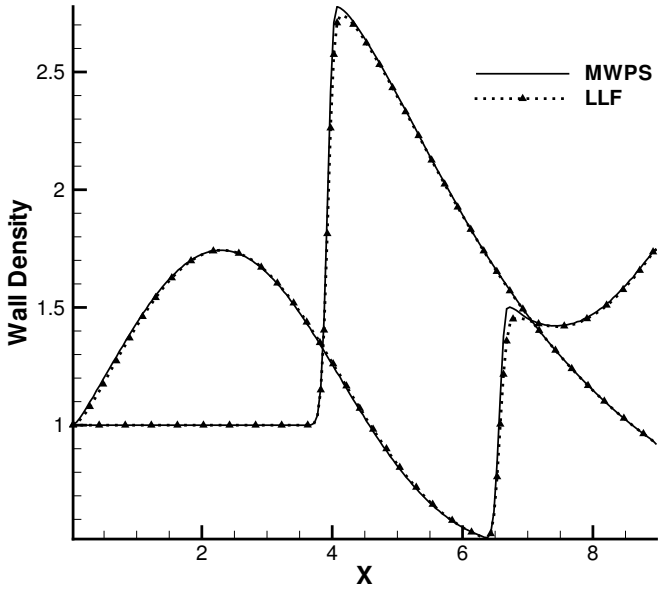

Figure 4.5. Density variations along the top and bottom boundary surfaces by MWPS and LLF schemes for steady magnetic nozzle flow problem obtained on structured grids

4.9.2 *Brio and Wu problem*

We now repeat the Brio and Wu problem, which is a standard 1D test case by carrying out the simulations on a 2D grid. The initial conditions are identical to those in Table 3.1 and we apply superfast outlet BC on all boundaries for this test case. Simulations are carried out on a [0,1]×[0,0.2] domain on a 400×20 uniform structured grid. A time-step of 10^{-4} is considered and simulations are carried out to a final time of 0.1. We choose V_{ref} as 1 and 500 sub-iterations are performed with $\Delta\tau = 10^{-4}$.

The solutions extracted across $y \approx 0.15$ is plotted against the solutions computed by 1D counterpart of the same scheme on a [0,1] domain with 400 points in Figure 4.9. All the five waves are well resolved by MWPS in the 2D simulation including the compound wave as is visible in the density and y-magnetic field variations. Some differences between the 1D and 2D results can be observed though and these are attributed to the divergence errors in the latter case. The variation of x-magnetic field and the distribution of divergence error at the final time along the length of the tube are shown in Figure 4.10. Recall that for the 1D simulation, the magnetic divergence $\nabla \cdot \mathbf{B}$ is identically zero at all times since $\frac{\partial(\cdot)}{\partial y} = \frac{\partial(\cdot)}{\partial z} = 0$ and B_x is constant everywhere. On the other hand B_x

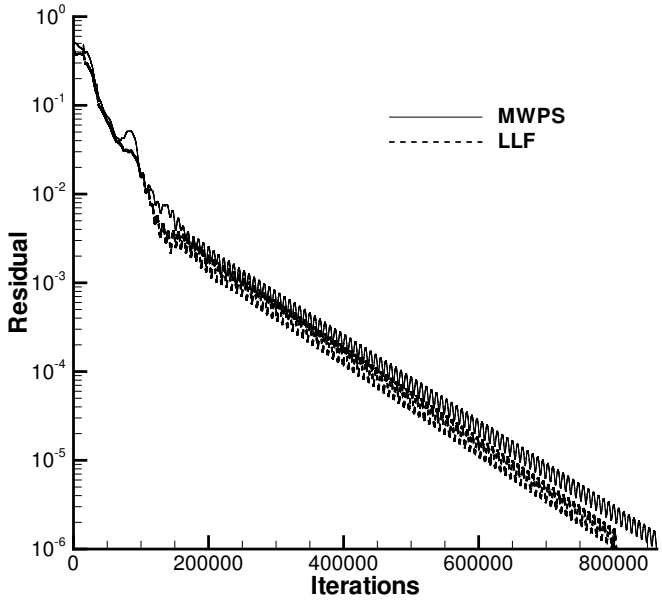

Figure 4.6. Convergence histories of simulations with MWPS and LLF schemes for steady magnetic nozzle flow problem on structured grids

does not remain constant in the 2D case as a consequence of the non-negligible $\nabla \cdot \mathbf{B}$ errors which are of the $\mathbf{O}(10^{-4})$. The solenoidality constraint for the 2D problem is not strongly enforced although the errors are at acceptable levels from a practical simulation viewpoint. Nevertheless, these low values of errors are a result of 500 sub-iterations (pseudo-time steps) at each physical time level. The temporal history of the L_2-norm of divergence error is presented in Figure 4.11 which shows that the use of no sub-iterations incur the highest error. This is not surprising, and use of more number of sub-iterations serve to lower the error levels considerably. One can see that the difference between 200 and 500 sub-iterations is not extremely significant. This can also be visualised in Figure 4.12 where the variation of density and the distribution of divergence error at the final time along the length of the tube are shown. It is clearly observed that there are no discernible differences between the solutions of 200 and 500 sub-iterations but the solution obtained by using no sub-iterations are anomalous and non-physical. This can be attributed to the fact that the divergence errors are significantly high in that case as clearly seen in the distribution of divergence error in Figure 4.12. Therefore we choose to consider 200 sub-iterations in all simulations to follow, unless otherwise specified, as a trade-off between cost and accuracy.

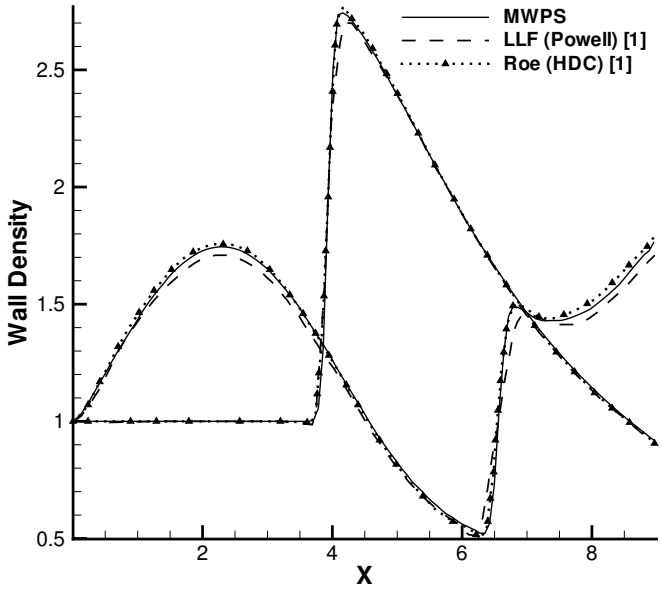

Figure 4.7. Density variations along the top and bottom boundary surfaces computed by MWPS, TVD Rusanov with Powell's source term approach (from Yalim [1]) and TVD Roe (HDC) (from Yalim [1]) schemes for the steady magnetic nozzle flow problem on unstructured grids

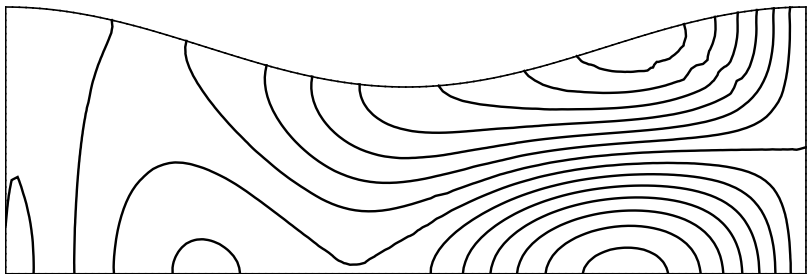

Figure 4.8. $\nabla \cdot \mathbf{B}$ errors over the domain at steady state computed by MWPS scheme for the steady magnetic nozzle flow problem on unstructured grids (Min: -6.58876×10^{-6}, Δ: 1.0, Max: 7.46778×10^{-6})

4.9.3 Shu-Osher MHD problem

As a further test of the efficacy of the 2D MHD solver, we solve a relatively more complex 1D test case in two dimensions. This test is the MHD version of the

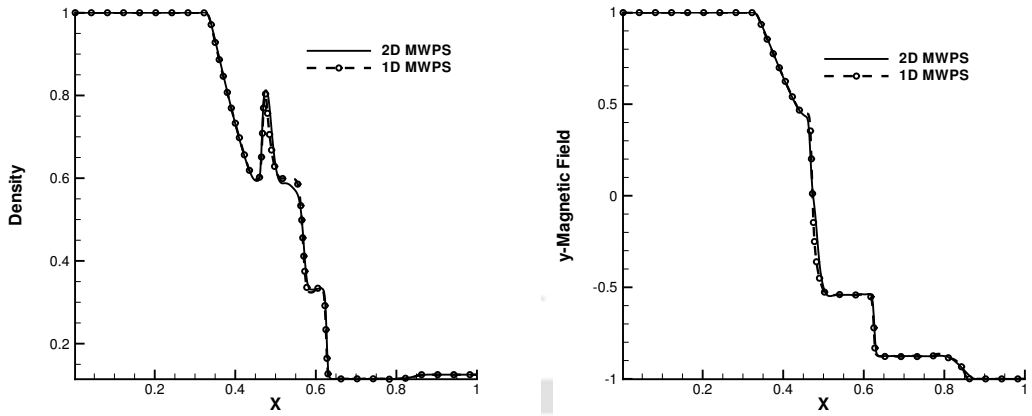

Figure 4.9. Density and B_y variations along the length of the tube at $t = 0.1$ for the Brio and Wu shock tube problem

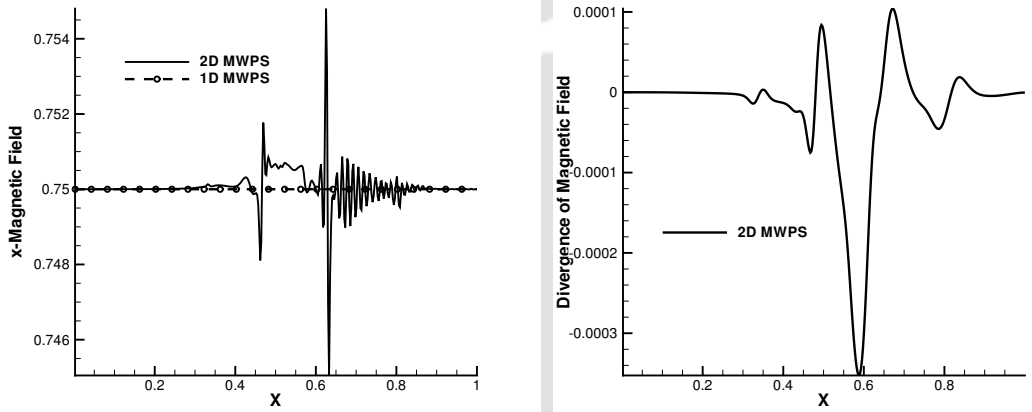

Figure 4.10. B_x and $\nabla \cdot \mathbf{B}$ variations along the length of the tube at $t = 0.1$ for the Brio and Wu shock tube problem

Shu-Osher shock tube problem and is solved on an uniform structured grid of size 3000×30 on a domain of [-5,5]×[0,2]. The initial conditions are summarised in Table 3.1 and describes a sinusoidal density perturbation of $0.2 \sin(5x)$ added downstream of a purely advecting supersonic shock wave, which gives rise to fast oscillations and complex flow features downstream of the shock. The simulations are carried out till $t = 0.6909$ with $\Delta t = \Delta\tau = 10^{-4}$ and V_{ref} is chosen equal to unity. The number of sub-iterations is fixed at 200, following observations in the Brio-Wu shock tube problem and the same boundary conditions as for the Brio-Wu problem are applied here as well.

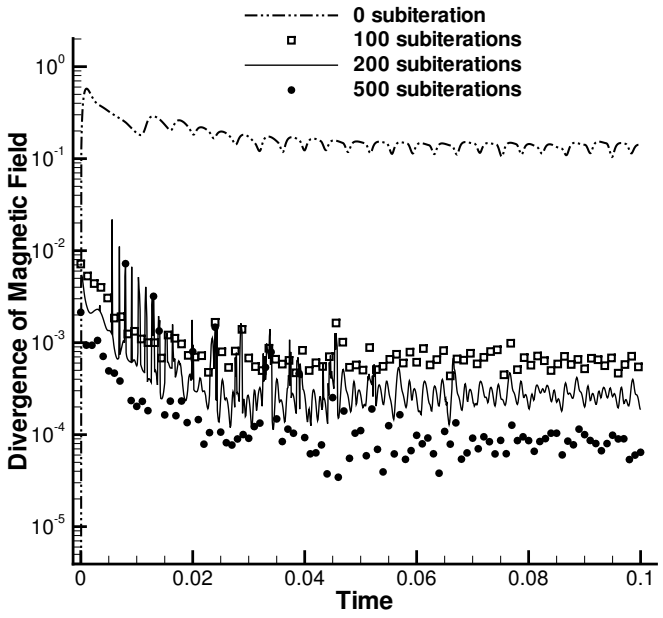

Figure 4.11. L_2-norm of $\nabla \cdot \mathbf{B}$ errors computed using MWPS scheme with different sub-iterations for the Brio and Wu shock tube problem

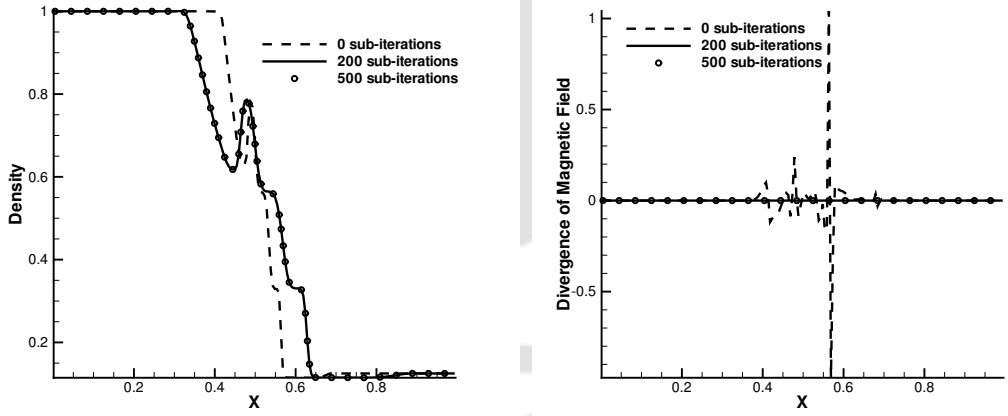

Figure 4.12. Density and $\nabla \cdot \mathbf{B}$ variations along the length of the tube at $t = 0.1$ obtained using 2D MWPS with 0, 200 and 500 sub-iterations for the Brio and Wu shock tube problem

In Figure 4.13 the density profile along the length of the tube obtained from 2D MWPS is plotted against the results obtained by 1D MWPS with 3000 points on the same length and the numerical results from [4]. The plots clearly show that the current scheme resolves the complex and small-scale flow features quite

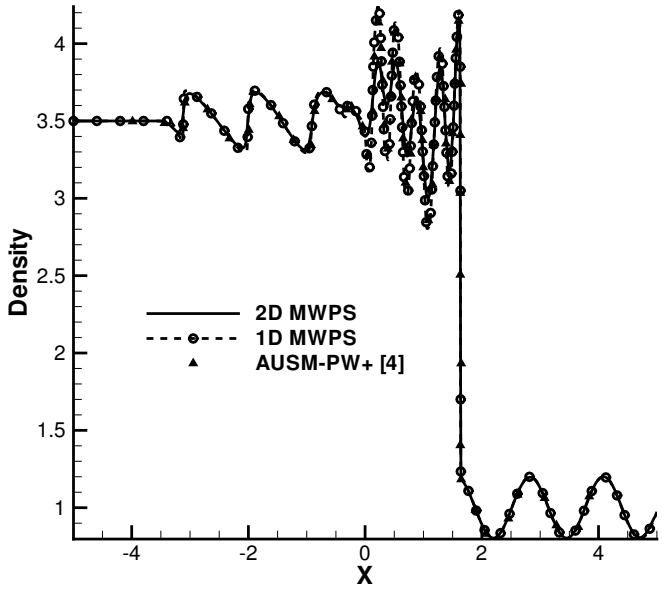

Figure 4.13. Density profile of MHD variant of Shu-Osher test

accurately and the results are in quite good agreement with those reported in [4] using a second-order accurate AUSM-PW+ scheme.

4.9.4 *Orszag-Tang vortex problem*

The first genuine test of the 2D unsteady MHD solver and the divergence cleaning approach is the Orszag-Tang vortex system. This test case, which is a genuinely 2D unsteady MHD problem is a severe turbulence test problem introduced by Orszag and Tang [80] and later extended to the supersonic flows by Picone and Dahlburg [81]. This is also arguably the most common test of MHD flow solvers in open literature [1–4,67,82,83] and the evolution of very complex flow features with interaction of multiple discontinuities make this an interesting and challenging problem. A structured grid of 200×200 in a domain of $[0, 2\pi] \times [0, 2\pi]$ is employed with doubly-periodic boundary conditions for purpose of simulation. Sinusoidal velocity and magnetic fields are superimposed to define a vortex inside the domain which is allowed to develop with time. Evolution of very complex flow features with interaction of multiple discontinuities make this an interesting test case.

The initial conditions inside the domain are,

$$\begin{pmatrix} \rho \\ u \\ v \\ w \\ B_x \\ B_y \\ B_z \\ P \\ \phi \end{pmatrix} = \begin{pmatrix} \gamma^2 \\ -\sin(y) \\ \sin(x) \\ 0 \\ -\sin(y) \\ \sin(2x) \\ 0 \\ \gamma \\ 0 \end{pmatrix} \tag{4.33}$$

with $V_{ref} = \sqrt{2}$, which corresponds to the maximum speed in the initial solution and $\gamma = 5/3$. For this test case, the simulations are carried out up to $t = 3.14$ with $\Delta t = \Delta\tau = 10^{-3}$. The number of sub-iterations is fixed at 200.

The pressure contours at $t = 3.14$ obtained using the MWPS scheme are shown along with those obtained by Yalim [1] in Figure 4.14. The results in [1] are also computed on a uniform structured 200×200 grid using a TVD Rusanov scheme and the comparison shows that the present simulations are able to resolve the complex flow features with reasonable accuracy. This is supported by the quantitative comparison shown in Figure 4.15 where the pressure along the length of the domain at $y = 1.933$ is compared with those obtained using the Roe scheme in [2], AUSM-PW scheme of Xisto et al. [3] and AUSM-PW+ scheme in [4]. We see that there is a reasonable agreement between the results which highlights that the accuracy of the proposed MHD flow solver.

We also demonstrate the importance of divergence cleaning by considering the effect of sub-iterations on divergence errors and numerical solution. The temporal history of divergence errors in the domain (L_2-norm) with and without sub-iterations are plotted in Figure 4.16. While the temporal history is very oscillatory, the use of 200 sub-iterations can be seen to decrease the divergence errors by nearly an order of magnitude. While this does not appear to be a significant reduction, it does have a strong impact on the numerical solution. The pressure contours without sub-iterations are shown in Figure 4.16 and a quick comparison with Figure 4.14 shows that the lack of divergence cleaning leads to a completely different solution which is physically anomalous. Figure 4.17 shows a quantitative comparison of the pressure at y= 1.933 with and without sub-iterations, and this also highlights the fact that numerical solutions without divergence cleaning are indeed spurious. One can conclude that the divergence cleaning effected using the ACA approach is an important facet of the MHD flow solver. Using a small number of sub-iterations (or a complete lack thereof) can cause the divergence errors to accumulate and lead to non-physical solutions and in some cases cause

the numerical simulation to terminate owing to negative pressure/density.

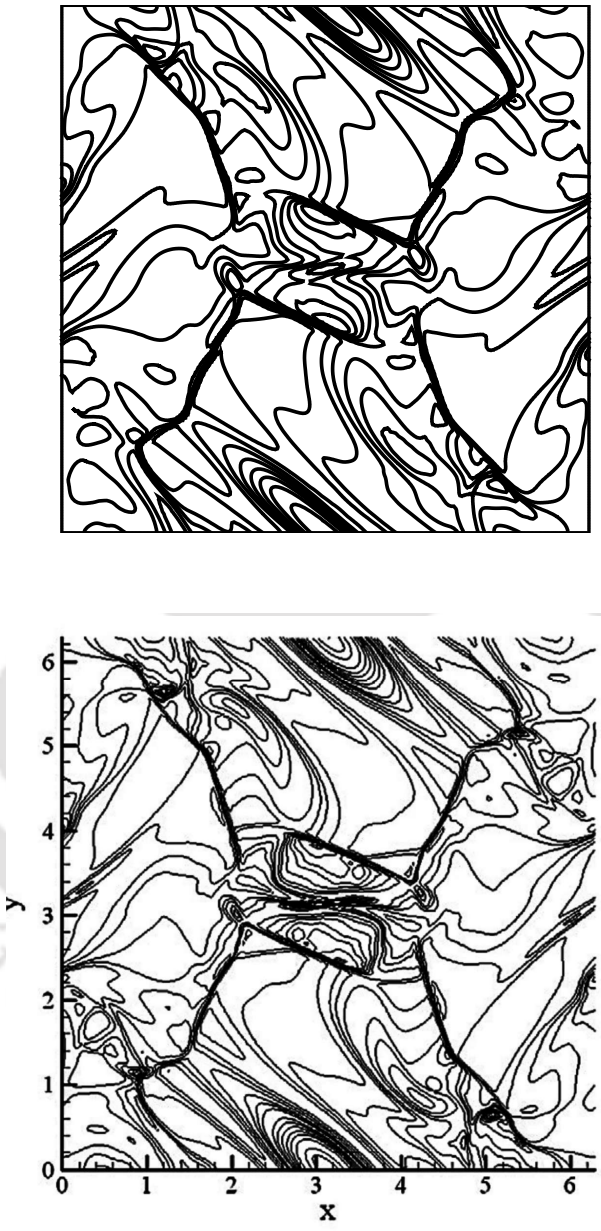

Figure 4.14. Pressure contours computed by MWPS scheme with 200 sub-iterations (Min: 0.490663, Δ: 0.557, Max: 5.50553) (on top) and by TVD Rusanov (HDC) scheme (from Yalim [1]) (bottom) at $t = 3.14$ for the Orszag-Tang vortex problem

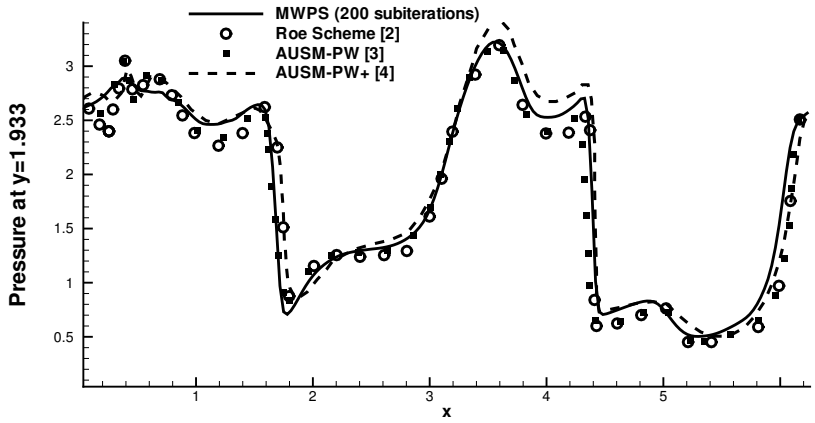

Figure 4.15. Pressure variations at $y = 1.933$ computed by MWPS scheme with 200 sub-iterations, Roe scheme in [2], AUSM-PW scheme in [3] and AUSM-PW+ scheme in [4] at $t = 3.14$ for the Orszag-Tang vortex problem

4.9.5 2D compressible MHD Riemann problem

We now consider the MHD analogue of the 2D Riemann problem which has also been investigated in [35]. We employ both structured grid with a resolution of 200×200 and unstructured grid with 82742 volumes (See Figure 4.18) on a computational domain of size $[0, 1]\times[0, 1]$ for the simulation. The four quadrants for this problem are defined as I: $x > 0.5, y > 0.5$, II: $x < 0.5, y > 0.5$, III: $x < 0.5, y < 0.5$ and IV: $x > 0.5, y < 0.5$ where the initial conditions as given in Table 4.1 are specified. The simulations are carried out till $t = 0.1$ with a time-step of 10^{-4}, $\gamma = 5/3$ and $V_{ref} = 1$. We use 200 sub-iterations per real time-step with a pseudo time-step of $\Delta\tau = 10^{-4}$. Superfast outlet boundary condition is used on all boundaries.

Quad.	ρ	ρu	ρv	ρw	B_x	B_y	B_z	E
I	0.9308	1.4557	-0.4633	0.0575	0.3501	0.9830	0.3050	5.0838
II	1.0304	1.5774	-1.0455	-0.1016	0.3501	0.5078	0.1576	5.7813
III	1.0000	1.7500	-1.0000	0.0000	0.5642	0.5078	0.2539	6.0000
IV	1.8887	0.2334	-1.7422	0.0733	0.5642	0.9830	0.4915	12.999

Table 4.1. Initial states of the 2D MHD Riemann problem

The pressure contours obtained using the MWPS scheme on both structured and unstructured meshes are presented in Figure 4.19. One can see that the primary flow features, although the interaction (at the center of the domain)

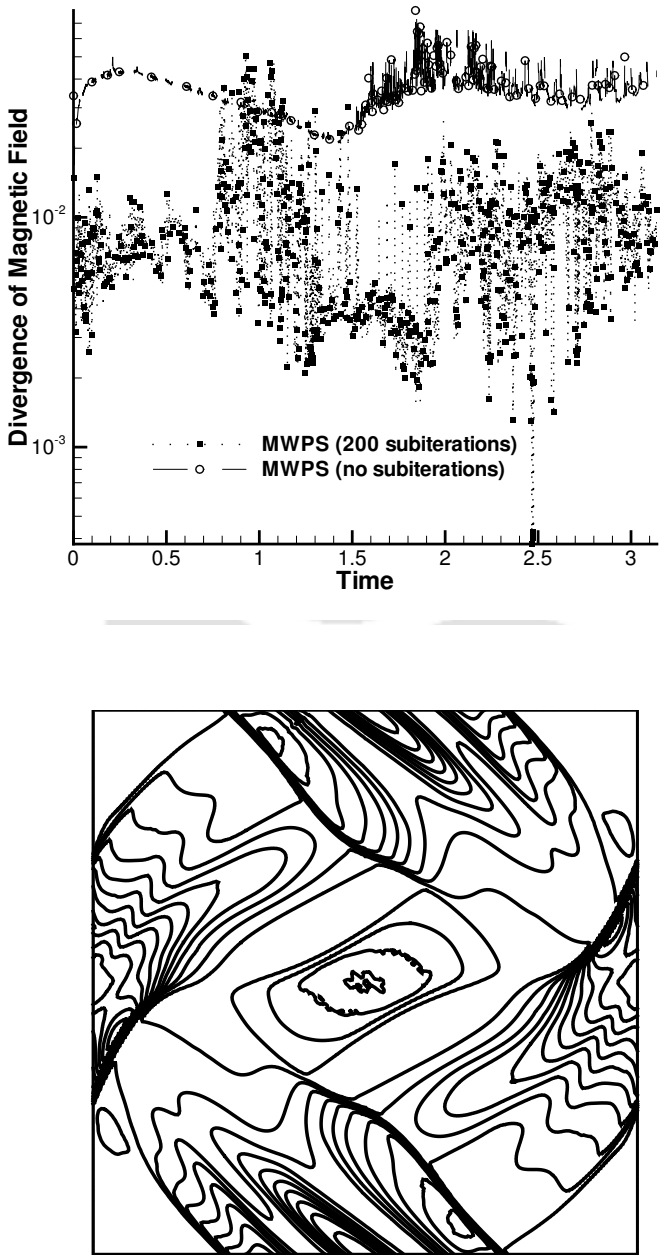

Figure 4.16. Comparison of $\nabla \cdot \mathbf{B}$ (L_2-norm) histories computed by MWPS with 200 sub-iterations and with no sub-iterations (on top) and pressure contours computed by MWPS scheme at $t = 3.14$ without sub-iterations (Min: 0.227564, Δ: 0.40, Max: 6.78285) (bottom) for the Orszag-Tang vortex problem

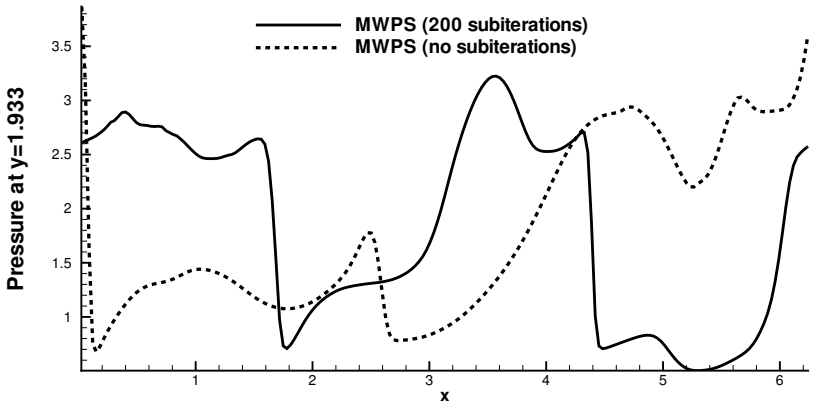

Figure 4.17. Pressure variations at $y = 1.933$ computed by MWPS scheme with 200 sub-iterations and with no sub-iterations at $t = 3.14$ for the Orszag-Tang vortex problem

is not quite well-resolved. A comparison with results in literature show that the genuine multi-dimensionality of this problem warrants a much greater grid resolution and spatially fourth-order accurate (or higher) schemes to accurately resolve the intricate flow features in the interaction zone. The ability of ACA to affect the solenoidality constraint is investigated on both grids by plotting the temporal history and local distribution of divergence errors at $t = 0.1$. The magnetic divergence in the domain for structured and unstructured grids are shown in Figure 4.20. The highest errors are observed on both meshes in the vicinity of the discontinuities, with the errors being much lower in other parts of the domain. The values are non-zero and higher by an order of magnitude on the unstructured mesh when compared with those on the structured mesh. The largest errors in $\nabla \cdot \mathbf{B}$ on the structured mesh are $\mathbf{O}(10^{-3})$. Although they are not extremely small divergence errors, however they suffice for a physically consistent simulation. This is also evident from Figure 4.21 where the temporal histories of the L_2-norms of divergence errors on both meshes are shown to be comparable, although the L_∞-norms are evidently higher on the unstructured mesh. Importantly, the temporal histories also show that the divergence errors remain bounded in time which is important for unsteady problems to ensure that the simulation would not become unstable (due to error accumulation) at large times. To further understand the effect of divergence error levels on the numerical solutions, we compare the density distribution along four sections obtained on both structured and unstructured grids. Figure 4.22 shows the density variation along the sections $x = 0.1$, 0.9 and $y = 0.1$, 0.9 on both meshes. It may be observed that the agreement between the results from structured and unstructured grids is quite good, although there are perceptible oscillations near discontinuities

in the results obtained from unstructured grids. This is likely due to the non-structured nature of the mesh and local non-orthogonality, but it is important to note that the deviations from the results on the structured mesh are quite minimal. These investigations show that the solution accuracy on structured and unstructured grids are comparable and the relatively higher $\nabla \cdot \mathbf{B}$ errors on the latter does not unduly compromise the solution accuracy. The studies therefore demonstrate that the proposed solver is reasonably accurate for 2D unsteady MHD flows on arbitrary polygonal meshes and that the relatively higher levels of divergence errors may be deemed acceptable from viewpoint of solution accuracy.

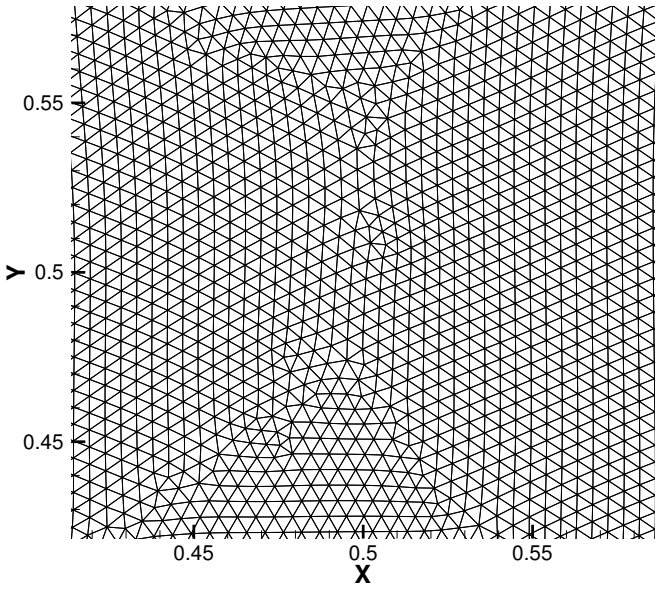

Figure 4.18. Zoomed view of the unstructured mesh used in the 2D MHD Riemann problem computations consisting of a toal of 82742 triangular elements

4.9.6 MHD Rotor problem

The MHD rotor case is a 2D problem where a dense disk of fluid (the rotor) rapidly spins in a lighter fluid (the ambient fluid). We choose an unit square of [0,1]×[0,1] as the computational domain following investigations by other researchers on this problem [1, 67, 82, 84]. The thermal pressure and magnetic fields are uniform throughout the domain with $P = 0.5$, $B_x = 2.5/\sqrt{4\pi}$ and $B_y = B_z = 0$. We assume that a circular disk of fluid of radius $r < r_0$ is rotating about the center (0.5,0.5) and $r_0 = 0.1$. Initially, the disk has $\rho = 10$, $u = -u_0(y-0.5)/r_0$ and $v = u_0(x-0.5)/r_0$. The ambient fluid at $r > r_1 = 0.115$

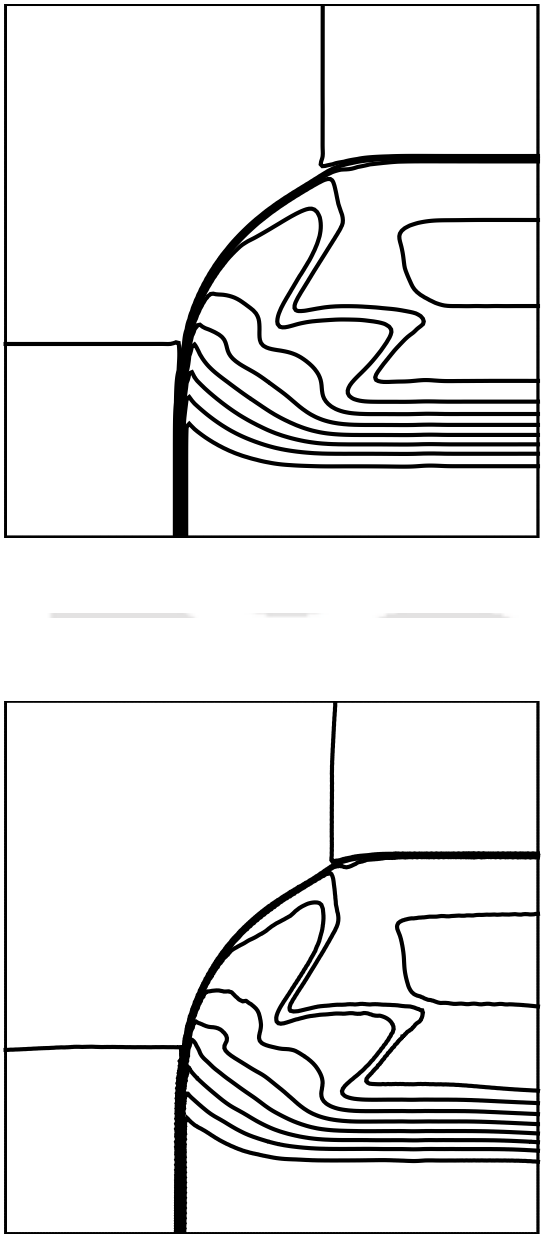

Figure 4.19. Pressure contours at $t = 0.1$ obtained using MWPS scheme on structured (Min: 2.5, Δ: 0.5, Max: 7.5) (on top) and unstructured grids (Min: 2.5, Δ: 0.5, Max: 7.5) (bottom) for the 2D MHD Riemann problem

has $\rho = 1$ and $u = v = w = 0$. The fluid between the rotating and the ambient

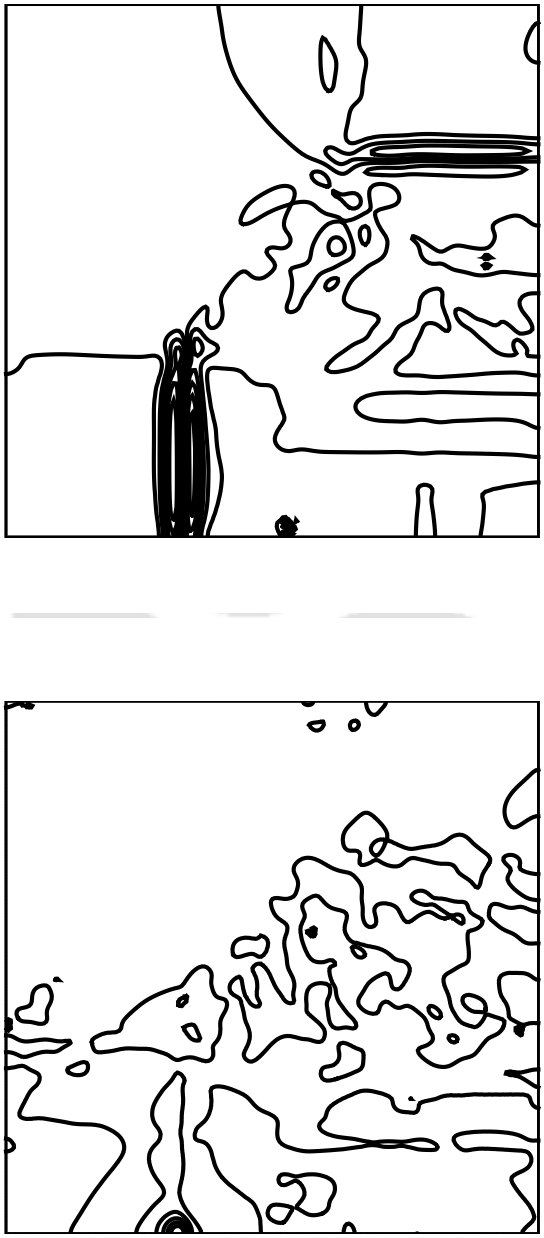

Figure 4.20. $\nabla \cdot \mathbf{B}$ variation inside the domain at $t = 0.1$ computed by MWPS scheme on structured (Min: -0.0025, Δ: 0.0005, Max: 0.0025) (on top) and unstructured (Min: -0.01, Δ: 0.005, Max: 0.02) (bottom) grids for the 2D MHD Riemann problem

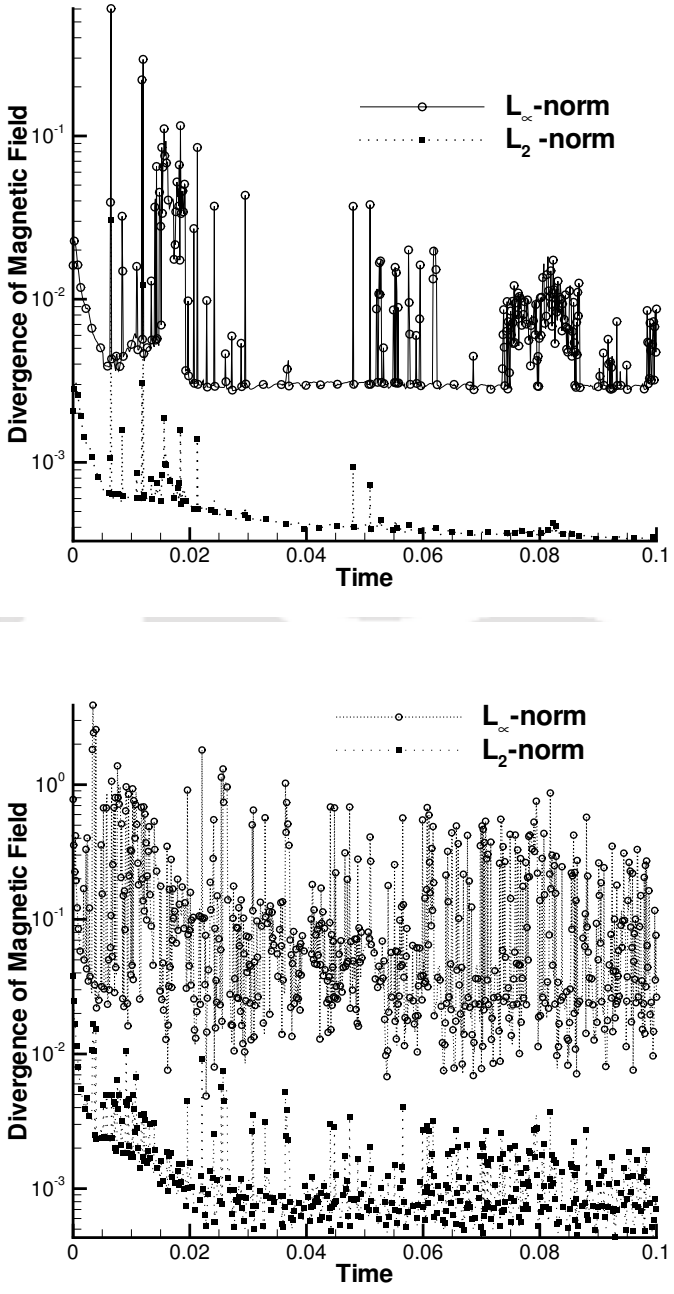

Figure 4.21. $\nabla \cdot \mathbf{B}$ histories computed till $t = 0.1$ by MWPS scheme on structured (on top) and unstructured (bottom) grids for the 2D MHD Riemann problem

fluid at $r_0 < r < r_1$ has linear density and angular speed profiles with $\rho = 1 + 9f$, $u = -fu_0(y - 0.5)/r$ and $v = fu_0(x - 0.5)/r$ where $f = (r_1 - r)/(r_1 - R_0)$ is a

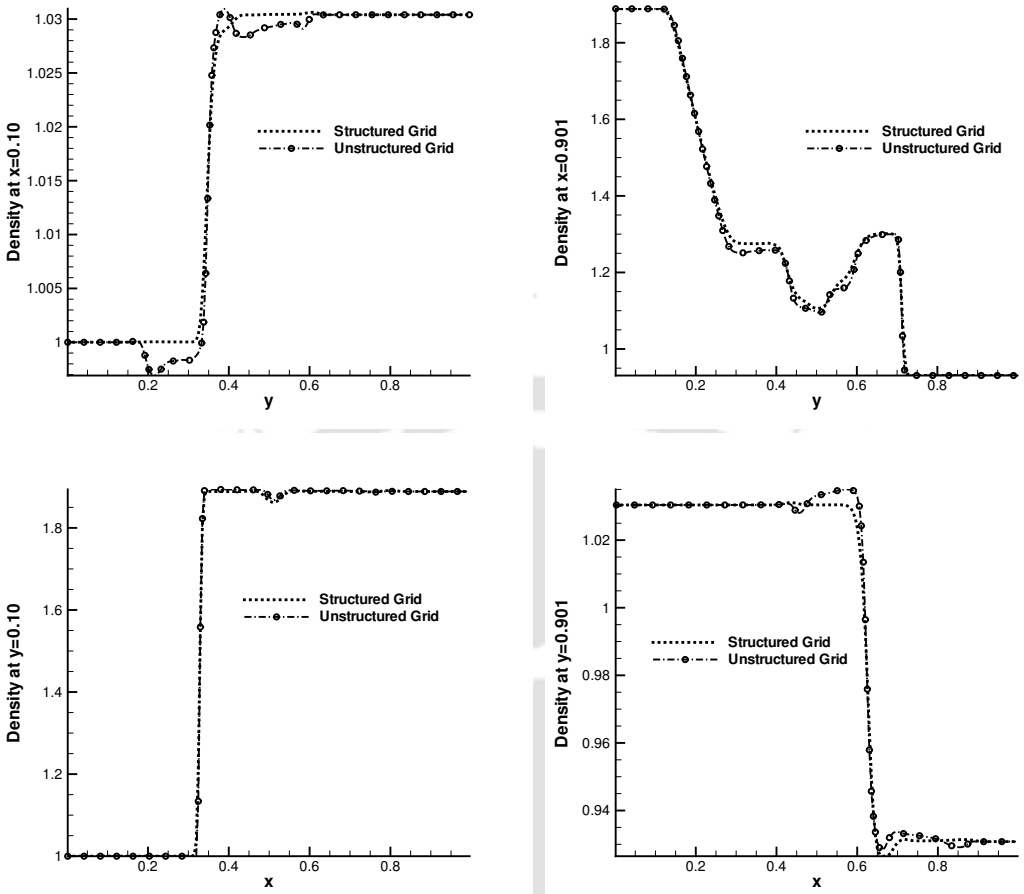

Figure 4.22. Density distribution along four sections computed by MWPS scheme on both structured and unstructured grids for the 2D MHD Riemann problem

"taper" function which ensures linear variation in the variables. No external body forces are applied to the rotor apart from giving an initial spin. We carry out simulations up to $t = 0.295$, with $\Delta t = \Delta\tau = 10^{-3}$ with $V_{ref} = 1$ and $\gamma = 5/3$. Superfast outlet boundary condition are prescribed on all boundaries and 200 sub-iterations are employed for purposes of divergence cleaning. We employ both structured and unstructured grids for these studies. While the structured grid has a resolution of 200×200 the unstructured mesh is composed of 72862 triangles.

The pressure and density contours simulated using the MWPS on the structured grid are shown in Figures 4.23 and 4.24 respectively along with those in [1] which were obtained by TVD Rusanov scheme on a 400×400 structured grid. As the rotor rotates and the flow develops, the magnetic pressure increases which compresses the fluid and results in an oblong shape which is visible in the contour plots. Despite the coarse mesh in the present simulations, the present results

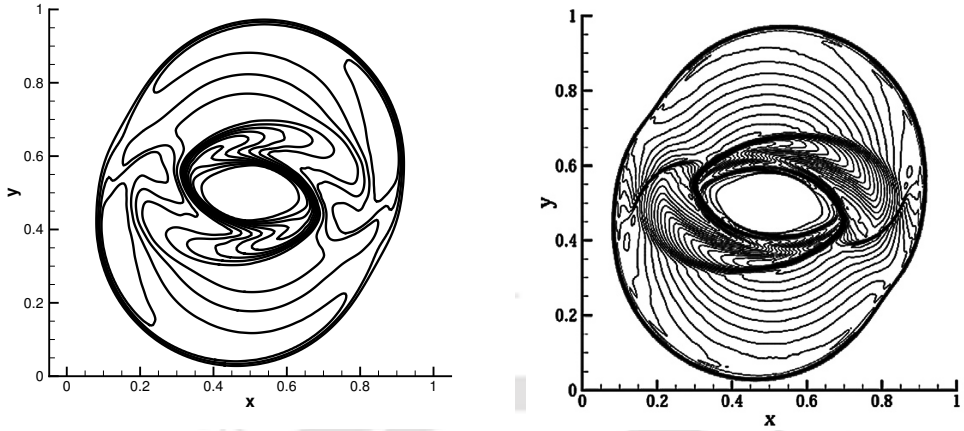

Figure 4.23. Pressure contours at $t = 0.295$ computed by MWPS scheme on structured grids (Min: 0.05, Δ: 0.05, Max: 0.7)(left) and TVD Rusanov (HDC) (from Yalim [1]) (right) for the MHD Rotor problem

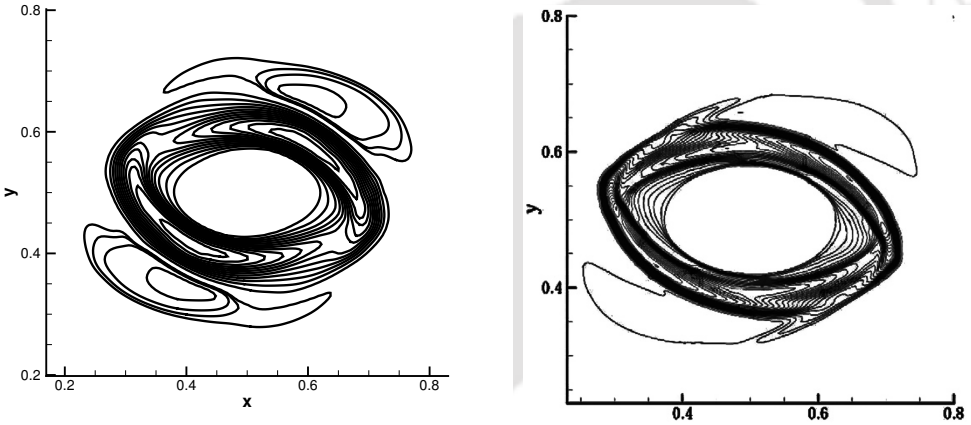

Figure 4.24. Density contours (zoomed view) at $t = 0.295$ computed by MWPS (HDC) scheme on structured grids (Min: 0.855, Δ: 0.5, Max: 7.0) (left) and TVD Rusanov (HDC) (from Yalim [1]) (right) for the MHD Rotor problem

show a fair qualitative agreement with those in [1]. The numerical results on the unstructured mesh are also similar to those obtained on the structured grid as can be seen from Figure 4.25 which shows the pressure and density contours. While we do not plot the divergence errors for this case, we must remark that the divergence errors are $\mathbf{O}(10^{-1})$ both on the structured and unstructured grids for this problem. This test case further highlights the ability of the MWPS scheme to handle complex MHD problems and the ACA approach in minimising numerical errors in magnetic divergence.

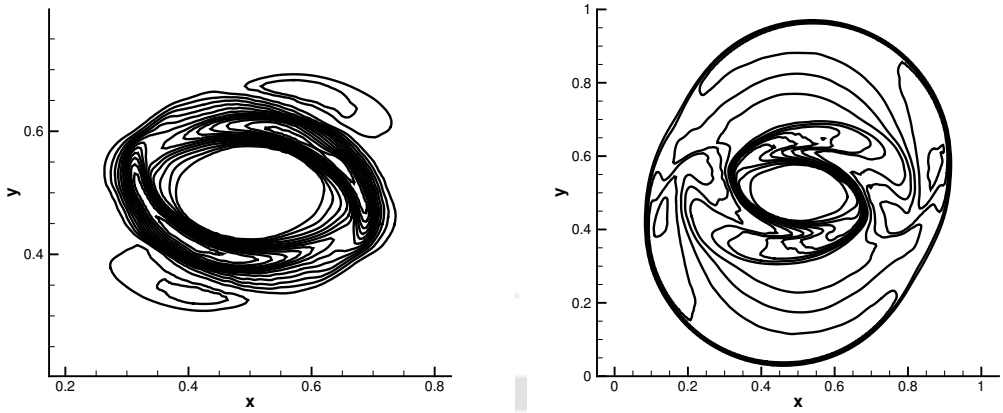

Figure 4.25. Density (zoomed view) (Min: 1.5, Δ: 0.5, Max: 7.5) (left) and pressure (Min: 0.05, Δ: 0.05, Max: 0.75) (right) contours at $t = 0.295$ computed by MWPS scheme on unstructured grid for the MHD Rotor problem

4.9.7 Cloud-shock interaction problem

The cloud-shock interaction problem is a challenging 2D problem where an initially stationary dense cloud interacts with a strong moving shock wave in the presence of an imposed transverse magnetic field. This interaction results in the disruption of the cloud and occurrence of very complex flow phenomena and has also been the subject of numerical studies in the past [4, 67, 85]. We make use of the same computational domain and grids which were employed for the MHD Rotor problem. The initial conditions contain a discontinuity parallel to the y-axis at $x = 0.05$ as shown in Figure 4.26 and are defined in Table 4.2.

	ρ	u	v	w	B_x	B_y	B_z	P	ϕ
Left	3.86859	11.2536	0	0	0	-2.1826182	2.1826182	167.345	0
Right	1.0	0	0	0	0	0.56418958	0.56418958	1	0

Table 4.2. The initial left and right states across a discontinuity parallel to the y-axis at $x = 0.05$ for cloud-shock interaction problem

The discontinuity at $t = 0$ is a combination of a fast shock wave and a rotational discontinuity in B_y. The circular cloud is centered at $(x, y) = (0.25, 0.5)$ with a radius $r = 0.15$, $\rho = 10$, $P = 1$ in hydrostatic equilibrium with the surrounding plasma. The solution is evolved till time $t = 0.06$ with $\Delta t = \Delta\tau = 10^{-4}$ on structured and $\Delta t = \Delta\tau = 10^{-5}$ on unstructured grids, respectively. We choose $\gamma = 5/3$ and $V_{ref} = 1$ with 200 sub-iterations employed in the simulations. All boundaries are prescribed superfast outlet BCs.

Density contours and the magnetic field lines at the final time obtained by the MWPS scheme on the structured grid are shown in Figure 4.27. The results on the unstructured mesh, which are very similar, are depicted in Figure 4.28. The present simulations clearly indicate the different flow features inherent in this problem. One can notice the strong bow shock ahead of the cloud and the re-compression shock at the tail of the cloud is also well resolved. The compression of the frontal area and the elongation of the cloud along the downstream direction, which are visible in other simulations as well [4,67], has also been well reproduced in the present simulations. The divergence errors in the domain at t= 0.06 for simulations on the structured and unstructured meshes are shown in Figure 4.29 and can be deemed acceptable. It must be emphasised that this is a severe MHD test case since the occurrence of negative pressure is not uncommon when the shock and the cloud first come into contact. However, such issues were not encountered in the present investigations using the MWPS scheme and the successful computation of this test case on both structured and unstructured grids is further evidence of the robustness of the proposed scheme and flow solver for multi-dimensional MHD computations.

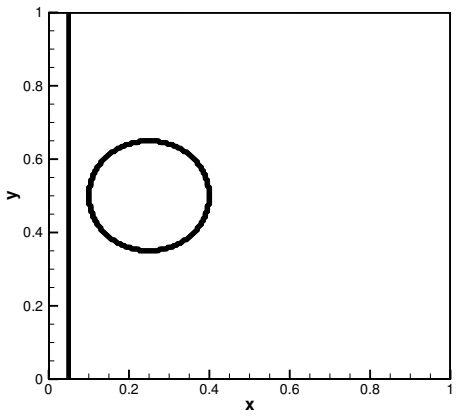

Figure 4.26. Density contours at $t = 0$ of the Cloud-shock interaction problem (Min: 1, Δ: 0.5, Max: 10)

This chapter describes the development and validation of a two-dimensional MHD flow solver. The extension of the MWPS scheme to two dimensions is discussed and while the underlying philosophy remains same as in 1D, the presence of the additional induction equation requires the magnetic flux vector to be split into two parts each of which is treated using a central scheme. The artificial compressibility analogy (ACA) approach is implemented to enforce the solenoidality constraint which is realised through the use of a dual-time stepping strategy. A large number of benchmark problems including two-dimensional counterparts of

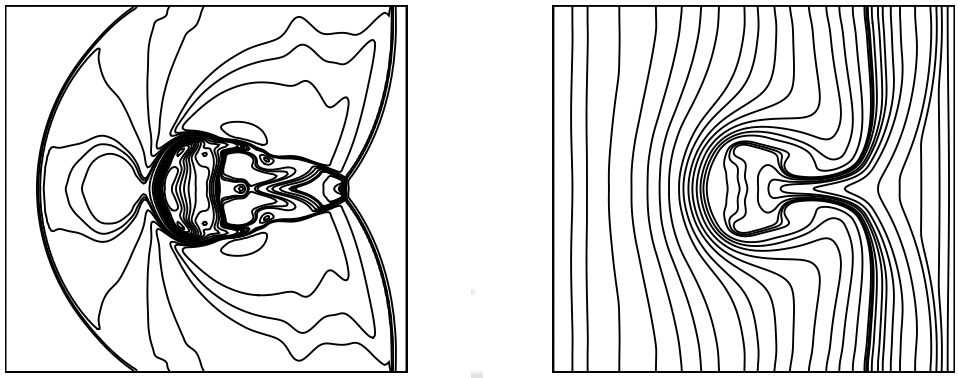

Figure 4.27. Density contours (Min: 2, Δ: 2, Max: 26) (on left) and magnetic field lines (on right) at $t = 0.06$ computed by MWPS scheme on structured grids for the Cloud-shock interaction problem

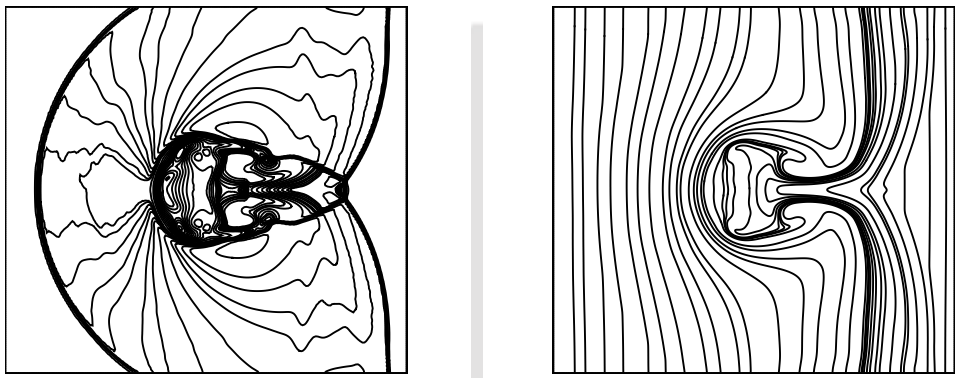

Figure 4.28. Density contours (Min: 2, Δ: 2, Max: 30) (on left) and magnetic field lines (on right) at $t = 0.06$ computed by MWPS scheme on unstructured grids for the Cloud-shock interaction problem

1D problems as well as genuinely two-dimensional MHD flows are simulated to investigate the versatility of the MWPS scheme and the implementation of the ACA approach. Numerical investigations on structured and unstructured meshes reveal that the proposed MHD solver provides an accurate and robust numerical framework for solution of complex MHD problems.

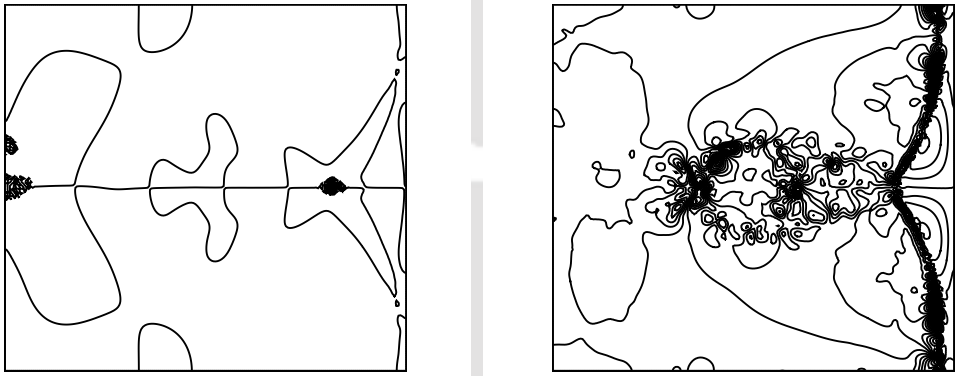

Figure 4.29. $\nabla \cdot \mathbf{B}$ variation inside the domain at $t = 0.06$ computed by MWPS scheme on structured (Min: -0.7, Δ: 0.1, Max: 0.5) (on left) and unstructured (Min: -0.25, Δ: 0.05, Max: 0.25) (on right) grids for the Cloud-shock interaction problem

5

A meshfree framework for one-dimensional ideal MHD

A meshfree framework for numerical simulations of MHD flows is proposed in this chapter. The framework is based on the Upwind Least-Squares Finite Difference Method (LSFD-U) [86] which can handle arbitrary point distributions. As this work is largely of an exploratory nature, we restrict ourselves to using the first-order accurate AUSM scheme in conjunction with explicit Euler time stepping for the studies. We investigate in the context of 1D MHD, the importance of discrete conservation and the role of point distribution and neighbourhood in LSFD-U in achieving a conservative and physically consistent solution. We first introduce the ideas of least-squares reconstruction and its use to formulate the meshfree approach and simulate one-dimensional problems on uniform point distributions. Conservation issues related to meshfree methods on non-uniform point distributions are then highlighted and a simple conservative meshfree approach based on a geometric weighting strategy is discussed.

5.1 Least-squares method for gradient computations

In this section, we shall briefly describe the least-squares approach for gradient estimation. This approach was earlier employed to devise higher-order "limited" schemes in Chapter 3 and shall form the backbone of the meshfree framework to be discussed in the following sections. Consider the 1D point distribution presented in Figure 5.1 where the derivatives of some function $\phi(x)$ are desired at every point. We shall focus on a specific point o for the purposes of discussion

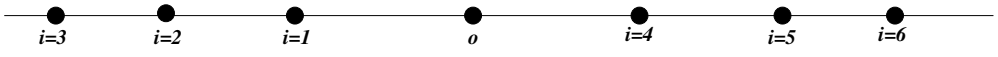

Figure 5.1. Typical 1D point distribution

and choose (without loss of generality) to determine the derivative at that point. One can determine or estimate the function at some point (say i) using the values

of the function and its derivatives at o using a Taylor series expansion,

$$\phi_i^{est} = \phi_o + \frac{\partial \phi}{\partial x}\Big|_o \Delta x_i + \frac{\partial^2 \phi}{\partial x^2}\Big|_o \frac{(\Delta x_i)^2}{2!} + \frac{\partial^3 \phi}{\partial x^3}\Big|_o \frac{(\Delta x_i)^3}{3!} + \cdots \tag{5.1}$$

with $\Delta(\cdot)_i = (\cdot)_i - (\cdot)_o$. It must be realised that while the function values are known at all points, the derivatives are in fact unknown. If we define a neighbourhood of m neighbours for the point o then it is possible to write a truncated Taylor series for each point in this neighbourhood (referred to as i in general) which may be expressed as,

$$\phi_i^{est} \simeq \phi_o + \frac{\partial \phi}{\partial x}\Big|_o \Delta x_i \tag{5.2}$$

We therefore have as many equations as the number of neighbours but only one unknown (for the 1D case) which is $\frac{\partial \phi}{\partial x}|_o$. This leads to an over-determined system and it is possible to obtain this derivative using the least-squares approach, which minimises the sum of squares of the error $E_i = \phi_i - \phi_i^{est}$. This sum may be expressed as,

$$\sum_{i=1}^{m} E_i^2 = \sum_{i=1}^{m} \left[\Delta \phi_i - \frac{\partial \phi}{\partial x}\Big|_o \Delta x_i \right]^2 \tag{5.3}$$

Minimisation of the error leads to a simple closed-form expression for the derivative which reads,

$$\frac{\partial \phi}{\partial x}\Big|_o = \frac{\sum_{i=1}^{m} (\Delta \phi_i \Delta x_i)}{\sum_{i=1}^{m} (\Delta x_i)^2} \tag{5.4}$$

This approach is referred to as unweighted linear-least squares approach. It may be seen that a typical neighbourhood for any point consists of a collection of other points which are not all equally spaced. In such a case, one would desire to "weigh" the contributions of each neighbourhood point differently. This leads to an alternative approach, referred to as the weighted least-squares approach which is popular among the finite volume community for gradient estimation. The expression for the first derivative using this approach reads,

$$\frac{\partial \phi}{\partial x}\Big|_o = \frac{\sum_{i=1}^{m} (w_i \Delta \phi_i \Delta x_i)}{\sum_{i=1}^{m} w_i (\Delta x_i)^2} \tag{5.5}$$

In the solution-dependent weighted least-squares approach the weights appearing in Eq (5.5) are chosen as function of the solution itself, which led to the "limiter" being embedded into the gradient estimation. However, the typical use of the weighted least-squares approach involves the use of geometric weights. A common choice is to use a monotonically decreasing function such as,

$$w_i = \frac{1}{r_i^p} \tag{5.6}$$

where r_i is the distance between point o and its neighbouring points i and the value of exponent p is usually chosen between 1 and 2, although higher values have been reported in literature [86]. The use of such an approach gives more importance to nearer neighbours rather than the farther ones, thereby maintaining the data locality. In the present work, unless otherwise specified we choose $p = 1$ which corresponds to inverse distance weighting. Notice also that the use of unit weights for all points will result in Eq (5.5) reducing to Eq (5.4) which is the unweighted least-squares procedure.

5.2 Upwind least-squares finite difference method

In this section, we shall discuss the salient details of the meshfree framework referred to as upwind least-squares finite difference method (LSFD-U). This methodology, first proposed by Sridar and Balakrishnan [86] is based on combining ideas of upwind schemes inherent to finite volume solvers along with least-squares framework discussed above for a point distribution (rather than a mesh). Starting from the conservative form of the 1D MHD equations one can see that the derivative for the flux vector $\mathbf{F}$ appearing in Eq. (2.12) can be approximated using the weighted least-squares approach as

$$\left.\frac{\partial \mathbf{F}}{\partial x}\right|_o = \frac{\sum_{I=1}^{m} w_I(\Delta \mathbf{F}_I \Delta x_I)}{\sum_{I=1}^{m} w_I(\Delta x_I)^2} \tag{5.7}$$

While the expressions in Eq. (5.7) and Eq. (5.5) appear similar, there is one important distinction that requires mention. In Eq. (5.7) the difference in fluxes (and other associated geometric quantities) are not between two points but rather between the point and an interface denoted as I. This characterises the LSFD-U framework which defines a fictitious interface I between any point and its neighbour and where the fluxes need to be determined. Once $\mathbf{F}_I$ is known, the flux difference $\Delta \mathbf{F}_I = \mathbf{F}_I - \mathbf{F}_i$ can be easily found out, since the solution values and fluxes at all points are available. The calculation of the interface flux (for the fictitious interfaces) is done using any upwinding scheme of choice with the left and right states obtained from the two points sharing the interface. It must be emphasised that the interface which is fictitious is assumed to be located midway between any point and its neighbour. The neighbourhood for any point is a global (*i.e.* direction independent) stencil and does not require the use of one-sided stencils which are necessitated in some other meshfree frameworks [87]. The use of a global stencil alleviates difficulties associated with determining physically relevant neighbours at boundaries which is an advantage for LSFD-U compared with some counterparts particularly in multi-dimensions. We remark further that while any flux scheme with a desired order of accuracy can be employed for interface flux computations, the first-order AUSM scheme is chosen in the present study.

5.3 Validation studies for ideal MHD flows

We carry out studies for a select number of test problems which were previously solved using the finite volume strategy (See Chapter 3) in order to check the correctness of implementation of the algorithm in meshfree solver for MHD problems. We choose an uniform point distribution in all cases with a symmetric neighbourhood stencil of immediate neighbours for every point (one each on the left and right) except for the boundaries which have one-sided neighbours. The test conditions for the problems are same as those discussed in Chapter 3 and summarised in Table 3.1 and will not be repeated here.

5.3.1 Brio and Wu problem

We first simulate the Brio and Wu shock tube problem using the LSFD-U approach. Computations are done on on a domain of unit length having 400 points with $\Delta t = 10^{-4}$ up to a final time of $t = 0.1$. The density and pressure profiles obtained by using LSFD-U together with AUSM flux formula is shown in Figure 5.2. All the flow features are correctly resolved including the compound wave. It must be noticed that since an uniform point distribution is employed for these computations, the results obtained are exactly similar to those obtained by finite volume method.

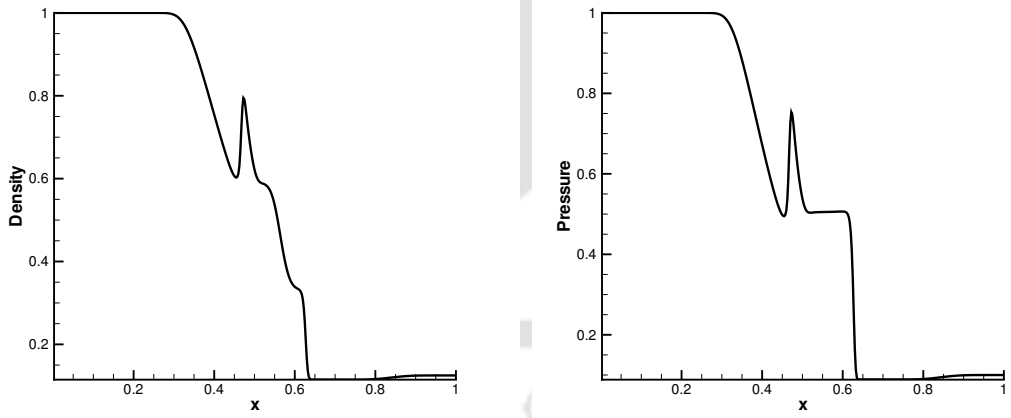

Figure 5.2. Solutions for Brio-Wu problem computed by LSFD-U (AUSM) using a 3-point stencil on uniform point distribution

5.3.2 Ryu and Jones problem 2a

To test the performance of LSFD-U on a more challenging MHD flow problem, we consider the seven-wave test case of Ryu and Jones. Simulations are carried

out with a time step of $\Delta t = 10^{-4}$ till $t = 0.2$ on a domain of unit length with 512 equally spaced points. The meshfree framework successfully captures all the seven waves including the rotational discontinuities, as shown in Figure 5.3.

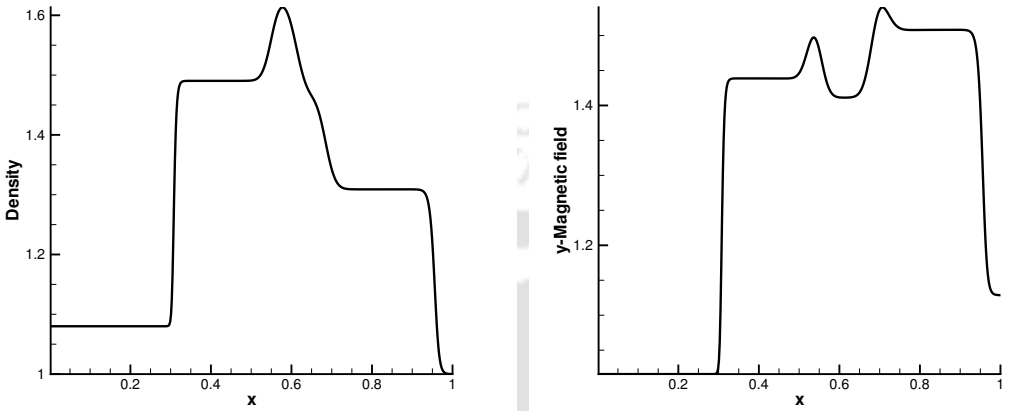

Figure 5.3. Solutions for Ryu-Jones 2a problem computed by LSFD-U (AUSM) using a 3-point stencil on uniform point distribution

5.3.3 *Isolated Alfven wave discontinuity problem*

As a third test, we numerically simulate an isolated Alfvén wave discontinuity across which the y-component of velocity and magnetic field are discontinuous. In this problem 400 points on a [0,1] domain are used for the simulations that are carried out till $t = 0.25$ with a time-step of 10^{-4}. As expected the current meshfree framework does not exactly resolve the isolated stationary Alfvén wave, although it correctly captures the mean location as can be seen from Figure 5.4.

It may be noted that these results are not unexpected and merely serve as a test of correctness of implementation of the LSFD-U solver. On uniform point distributions with a three-point stencil, LSFD-U and FVM are indeed equivalent as will be shown later in this chapter. Consequently, the results obtained above are indistinguishable from the first-order results using FVM (although not shown here for brevity). Nevertheless, this similarity between FVM and LSFD-U is lost in multi-dimensions and also in one-dimensional problems with non-uniform point distributions. Importantly, while FVM is conservative by construction, LSFD-U which works with the "strong" form of the equations does not necessarily guarantee discrete conservation. In the following sections we investigate the requirements for a conservative meshfree approach for 1D problems in MHD with an emphasis on arbitrary point distributions.

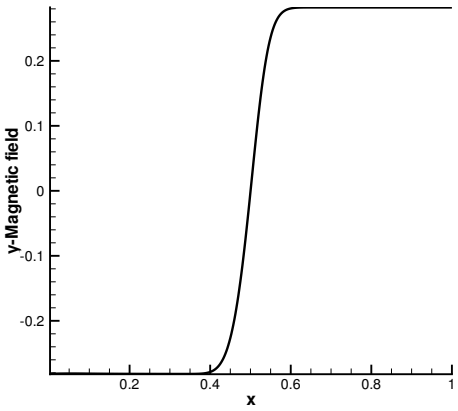

Figure 5.4. y-Magnetic field profile for isolated Alfvén wave discontinuity computed by LSFD-U (AUSM) using a 3-point stencil on uniform point distribution

5.4 On necessary conditions for a conservative approach

The primary reasons for the popularity of finite volume method as the choice of discretisation in fluid-flow problems is its ability to numerically mimic the property of conservation. The importance of discrete conservation assumes greater significance in compressible flow problems involving discontinuities and one can easily show that a lack of discrete conservation get manifested in wrong shock speeds, shock strengths and shock locations. One of the glaring drawbacks of most meshfree schemes pertain to their inability to guarantee discrete conservation. The construction of a general meshfree approach which is conservative in multi-dimensions for MHD equations still remains an open problem of considerable interest. However, the recent studies of Chiu et al. [45] show that one can construct a conservative meshfree framework if care is taken in defining the discrete operators involved in the approach. They propose that any meshfree framework must satisfy two conditions summarised below and referred to herein as CWRJ (Chiu-Wang-Hu-Jameson) conditions.

Let us define the first derivative for the flux vector analogous to the definition in [45] as

$$\Omega_i \frac{\delta \mathbf{F}}{\delta x}\Big|_i = a_{i,i}\mathbf{F}_i + \sum_{I \in S_i} a_{i,I}\mathbf{F}_I \tag{5.8}$$

where $\frac{\delta(\cdot)}{\delta x}$ denotes the discrete derivative operator, Ω_i represents a "fictitious" (or virtual) volume associated with the node i and S_i denotes the neighbourhood stencil. The coefficients $a_{i,i}$ and $a_{i,I}$ are associated with node i and the node-face

pair $i - I$ respectively, where I is the location of the fictitious interface between point i and its neighbouring point j. It must be pointed out that $\frac{\delta \mathbf{F}}{\delta x}\Big|_i$ must be interpreted as the discrete approximation to the continuous flux derivative at point i. The two necessary conditions which are needed to guarantee discrete conservation are the following.

Condition 1 (C1): The coefficients must satisfy the reciprocity criterion. Stated mathematically we have,

$$a_{i,I} = -a_{j,I}, \qquad i \neq j, \qquad j \in S_i \Leftrightarrow i \in S_j \tag{5.9}$$

$$a_{i,i} = 0, \qquad i \notin S_B \tag{5.10}$$

where S_i and S_j refer to the sets of neighbours for the points i and j respectively.

Condition 2 (C2): The coefficients must satisfy the following consistency criterion for all polynomials with a total degree of L where x_i is the co-ordinate of node i and x_I is the co-ordinate of fictitious interface I.

$$a_{i,i}\phi(x_i) + \sum_{I \in S_i} a_{i,I}\phi(x_I) = \Omega_i \frac{\delta \phi(x_i)}{\delta x} \tag{5.11}$$

The condition C1 demands that the neighbourhood stencil should be such that if i is a neighbour of j, then j should necessarily be a neighbour of i. One can achieve this with a little care by choosing a "symmetric" neighbourhood. This means that for any point we choose equal number of neighbouring points both on the left and right (in one dimension) although the neighbours need not *necessarily* be equidistant from the point under consideration. Any "asymmetric" neighbourhood indeed would clearly violate the C1 condition. However, it must also be remarked that a mere reciprocal neighbourhood does not mean that C1 would be satisfied, as we shall demonstrate later in this chapter. The condition C2 is purely a statement of consistency and along with C1 show how meshfree frameworks can satisfy local and global conservation at the discrete level. This however depends on how the coefficients $a_{i,I}$ are derived for each point distribution and Chiu et al. have described strategies to obtain these coefficients in a generalised framework that shows superior discrete conservation properties. It is evident from Section 5.3 that FVM results are identical to LSFD-U on uniform meshes and conservation is therefore guaranteed. In the following section, we show that the finite volume method on a general non-uniform mesh satisfies C1 but not C2. This leads us to marginally modify the C2 condition and the results then apply equally well to uniform and non-uniform meshes or point distributions. Since FVM is based on ideas of the weak (or integral form) and is conservative by construction, one can then argue that any meshfree framework that satisfies the C1/C2 conditions would behave similarly and consequently mimic the discrete conservation properties of the FVM.

5.5 Finite volume method and the C1/C2 conditions

We shall study the finite volume method in the framework of the conditions discussed above in one-dimension. In this case, the volume appearing in Eq. (5.8) is no longer virtual and represents a true volume bounded by the true faces. For the purpose of discussion, we specifically consider a non-uniform mesh as shown in Figure 5.5 which is typical of a stretched mesh. It may be noted that the node i refers to the cell center for which $i + 1/2$ and $i - 1/2$ denote the cell faces. Following the finite volume method, we would then have for point i, where the values need to be interpreted as the cell-averaged value lumped at the centroid, the following expression for the flux derivative.

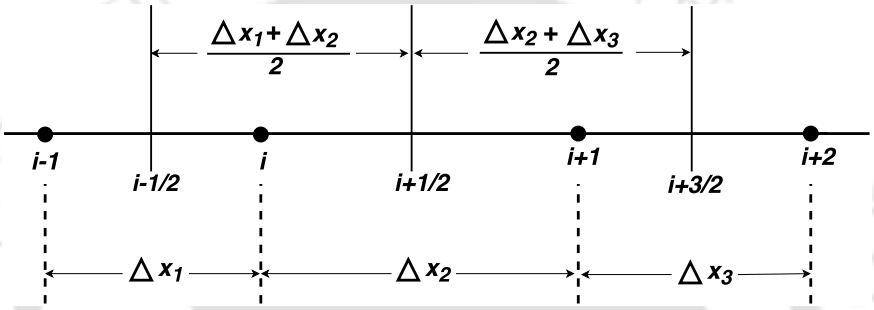

Figure 5.5. Typical non-uniform grid

$$\left.\frac{\delta \mathbf{F}}{\delta x}\right|_i = \frac{\mathbf{F}_{i+\frac{1}{2}} - \mathbf{F}_{i-\frac{1}{2}}}{\frac{\Delta x_1 + \Delta x_2}{2}} \tag{5.12}$$

Similarly, we can write the flux derivative for for point $i+1$ as,

$$\left.\frac{\delta \mathbf{F}}{\delta x}\right|_{i+1} = \frac{\mathbf{F}_{i+\frac{3}{2}} - \mathbf{F}_{i+\frac{1}{2}}}{\frac{\Delta x_2 + \Delta x_3}{2}} \tag{5.13}$$

Comparing Eq. (5.12) with Eq. (5.8) one can show that,

$$a_{i,i+\frac{1}{2}} = 1, \quad a_{i,i-\frac{1}{2}} = -1, \quad a_{i,i} = 0 \tag{5.14}$$

On similar lines, it follows from Eqs. (5.13) and (5.8) that,

$$a_{i+1,i+\frac{3}{2}} = 1, \quad a_{i+1,i+\frac{1}{2}} = -1, \quad a_{i+1,i+1} = 0 \tag{5.15}$$

It is therefore easy to see that,

$$a_{i,i+\frac{1}{2}} = -a_{i+1,i+\frac{1}{2}} \tag{5.16}$$

These relations show that the reciprocity condition C1 is satisfied in FVM. Furthermore, every face is indeed necessarily shared by two neighbours, which is

implicit in the construction of the finite volume approach.

To check for C2, let us first consider two different polynomials viz. $\phi(x) = 1$ and $\phi(x) = x$. The first is a constant function while the second is representative of a linear function. For the zero-order polynomial we have,

$$\Omega_i \frac{\delta\phi(x_i)}{\delta x} = 0 \tag{5.17}$$

On the other hand we also get,

$$a_{i,i}\phi(x_i) + \sum_{I \in S_i} a_{i,I}\phi(x_I) = a_{i,i} + a_{i,i+\frac{1}{2}} + a_{i,i-\frac{1}{2}} = 0 + 1 - 1 = 0. \tag{5.18}$$

It follows from Eqs. (5.17) and (5.18) that the consistency condition is satisfied for $L = 0$. Repeating this exercise for the first-order polynomial, we have

$$\Omega_i \frac{\delta\phi(x_i)}{\delta x} = \Omega_i \tag{5.19}$$

and

$$a_{i,i}\phi(x_i) + \sum_{I \in S_i} a_{i,I}\phi(x_I) = a_{i,i}x_i + a_{i,i+\frac{1}{2}}x_{i+\frac{1}{2}} + a_{i,i-\frac{1}{2}}x_{i-\frac{1}{2}} \tag{5.20}$$

Employing Eq. (5.14) in Eq. (5.20) and simplifying gives

$$x_{i+\frac{1}{2}} - x_{i-\frac{1}{2}} = \Omega_i \tag{5.21}$$

This shows that the condition C2 is also satisfied by the finite volume method for $L = 1$. However, for a second-order polynomial defined by $\phi(x) = x^2$, one can see that

$$\Omega_i \frac{\delta\phi(x_i)}{\delta x} = \Omega_i(2x_i) \tag{5.22}$$

and

$$a_{i,i}\phi(x_i) + \sum_{I \in S_i} a_{i,I}\phi(x_I) = a_{i,i}x_i^2 + a_{i,i+\frac{1}{2}}x_{i+\frac{1}{2}}^2 + a_{i,i-\frac{1}{2}}x_{i-\frac{1}{2}}^2 \tag{5.23}$$

After substituting the values of the coefficients one obtains

$$a_{i,i}x_i^2 + a_{i,i+\frac{1}{2}}x_{i+\frac{1}{2}}^2 + a_{i,i-\frac{1}{2}}x_{i-\frac{1}{2}}^2 = x_{i+\frac{1}{2}}^2 - x_{i-\frac{1}{2}}^2 \tag{5.24}$$

We can write the above equation as

$$x_{i+\frac{1}{2}}^2 - x_{i-\frac{1}{2}}^2 = (x_{i+\frac{1}{2}} + x_{i-\frac{1}{2}})(x_{i+\frac{1}{2}} - x_{i-\frac{1}{2}}) = 2\left(\frac{x_{i+\frac{1}{2}} + x_{i-\frac{1}{2}}}{2}\right)\Omega_i \tag{5.25}$$

It must be emphasised here that

$$2\left(\frac{x_{i+\frac{1}{2}} + x_{i-\frac{1}{2}}}{2}\right)\Omega_i = \Omega_i(2x_i) \tag{5.26}$$

only in the case of uniform point distributions. Thus we can conclude that C2 condition is not valid for non-uniform grid/point distribution if we include polynomials of degree two. Clearly, this is a violation of the C2 condition, which arises because the centroids of the finite volumes do not coincide with the nodal points themselves on a generic non-uniform mesh. However, the finite volume method is known to be conservative by construction and we therefore modify the condition C2 to include polynomials of only degree one or lesser. The revised C2 condition therefore applies only to polynomials of degree $L \leq 1$. This is a less general consistency criterion than the one originally proposed in the CWHJ conditions, but allows us to treat the meshfree and finite volume frameworks by the same yardstick. We now discuss the dependence of the neighbourhood in LSFD-U framework on C1/C2 conditions in the following section with the C2 condition as modified above.

5.6 LSFD-U and the C1/C2 conditions

The LSFD-U framework is now applied to the same non-uniform point distribution in Figure 5.5 to understand if the method can preserve discrete conservation. There are two important aspects inherent in the expression for the flux derivative in Eq. (5.7) that needs to be investigated in this regard. The first is the role of weights and the second is the neighbourhood stencil for every point. We begin by considering the unweighted LSFD-U with a non-uniform point distribution. We assume two neighbours (one on either side, but unequally spaced) for each node except in the boundaries. We remark that the effect of boundaries are not considered herein, since for typical 1-D problems it is fair to assume an exact BC or periodic BCs. For a 3-point stencil on the non-uniform point distribution, the flux derivative in Eq. (5.7) (employing unit weights to reduce the formula to unweighted LSFD-U) simplifies as,

$$\left.\frac{\delta \mathbf{F}}{\delta x}\right|_i = \frac{(\mathbf{F}_{i+\frac{1}{2}} - \mathbf{F}_i)(\frac{\Delta x_2}{2}) + (\mathbf{F}_{i-\frac{1}{2}} - \mathbf{F}_i)(-\frac{\Delta x_1}{2})}{(\frac{\Delta x_1}{2})^2 + (\frac{\Delta x_2}{2})^2} \tag{5.27}$$

The "virtual" volume bounded between the "fictitious" faces is,

$$\Omega_i = \frac{\Delta x_1 + \Delta x_2}{2} \tag{5.28}$$

and therefore one can obtain after algebraic manipulations

$$\Omega_i \left.\frac{\delta \mathbf{F}}{\delta x}\right|_i = \frac{\Delta x_2(\Delta x_1 + \Delta x_2)}{\Delta x_1^2 + \Delta x_2^2}\mathbf{F}_{i+\frac{1}{2}} - \frac{\Delta x_1(\Delta x_1 + \Delta x_2)}{\Delta x_1^2 + \Delta x_2^2}\mathbf{F}_{i-\frac{1}{2}} + \frac{\Delta x_1^2 - \Delta x_2^2}{\Delta x_1^2 + \Delta x_2^2}\mathbf{F}_i. \tag{5.29}$$

We have

$$a_{i,i+\frac{1}{2}} = \frac{\Delta x_2(\Delta x_1 + \Delta x_2)}{\Delta x_1^2 + \Delta x_2^2}, \quad a_{i,i-\frac{1}{2}} = -\frac{\Delta x_1(\Delta x_1 + \Delta x_2)}{\Delta x_1^2 + \Delta x_2^2}, \quad a_{i,i} = \frac{\Delta x_1^2 - \Delta x_2^2}{\Delta x_1^2 + \Delta x_2^2} \neq 0$$

Clearly one can see that the diagonal coefficient $a_{i,i}$ is non-zero which violates condition C1. It must therefore be emphasised that the reciprocity condition C1 is more stringent than having a "symmetric" neighbourhood. While the latter is necessary for C1 to be satisfied, the present study shows that it is not a sufficient condition. For the unweighted LSFD-U with a 3-point stencil (two symmetric neighbours), the C1 condition is indeed not satisfied. One can show that a similar result may be arrived for "asymmetric" neighbourhoods (say a 4-point stencil) as well. Furthermore, we do not bother to investigate condition C2 for the unweighted LSFD-U, since the violation of any of the C1/C2 conditions amounts to a lack of conservation. It must be remarked that the results on other non-uniform distributions are indeed similar and the present choice suffices to highlight the lack of conservation (in terms of violation of C1/C2) of the unweighted LSFD-U.

We now proceed to study the effect of suitable weights on the ability of LSFD-U to satisfy C1/C2 conditions. While there are several possible choices, we simply choose a geometric weight as below.

$$w_I = \frac{1}{|\Delta x_I|} \tag{5.30}$$

This choice is common in least-squares approaches and is referred to as Inverse Distance Weighting (IDW) where $|\Delta x_I|$ refers to the absolute distance between point i and the fictitious interface I associated with its neighbour j. It can then be shown that the flux derivative for this choice of weights becomes,

$$\frac{\delta \mathbf{F}}{\delta x}\Big|_i = \frac{(\mathbf{F}_{i+\frac{1}{2}} - \mathbf{F}_i)(\frac{\Delta x_2}{2})|\frac{2}{\Delta x_2}| + (\mathbf{F}_{i-\frac{1}{2}} - \mathbf{F}_i)(-\frac{\Delta x_1}{2})|-\frac{2}{\Delta x_1}|}{(\frac{\Delta x_1}{2})^2|\frac{2}{\Delta x_1}| + (\frac{\Delta x_2}{2})^2|-\frac{2}{\Delta x_2}|} \tag{5.31}$$

On algebraic simplifications this reduces to,

$$\frac{\delta \mathbf{F}}{\delta x}\Big|_i = \frac{\mathbf{F}_{i+\frac{1}{2}} - \mathbf{F}_{i-\frac{1}{2}}}{\frac{\Delta x_1 + \Delta x_2}{2}} \tag{5.32}$$

which is interestingly the same expression as obtained in Eq. (5.12) for the finite volume method. Clearly, the choice of IDW reduces the LSFD-U approach to an equivalent finite volume approach. Furthermore, the latter obeys C1/C2 and is conservative and it therefore follows that the weighted LSFD-U would mimic these properties. It can be seen with a little effort that the use of two neighbours in the LSFD-U framework would mean that every point appears as a neighbour exactly twice. Thus, the "fictitious" interface would participate in flux computations exactly twice as well, just like the cell faces in FVM where each face is shared by exactly two cells. The use of IDW as a geometric weighting technique then effectively transforms the non-uniform mesh into a uniform one and it is then not difficult to see how conservation gets enforced. It is however

more interesting to see what would happen if a different neighbourhood (from Figure 5.6) involving 4-point and 5-point stencils are chosen. For these cases, the expressions would reduce to,

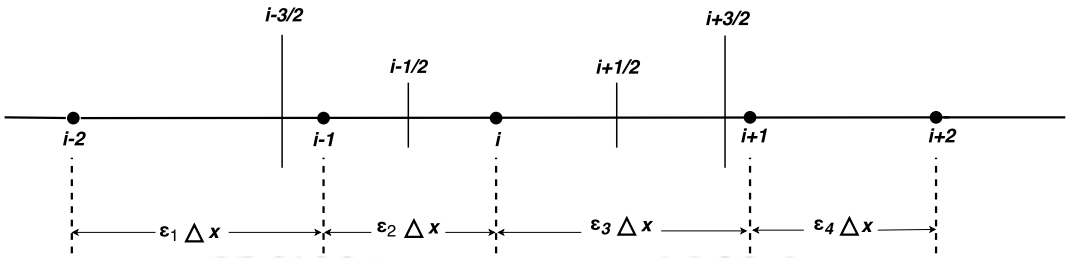

Figure 5.6. 5-point stencil on 1D non-uniform point distribution

$$\frac{\delta \mathbf{F}}{\delta x}\Big|_i = \frac{(\mathbf{F}_{i+\frac{1}{2}} + \mathbf{F}_{i+\frac{3}{2}}) - (\mathbf{F}_{i-\frac{1}{2}} + \mathbf{F}_i)}{\frac{\epsilon_2 \Delta x}{2} + \epsilon_3 \Delta x + \frac{\epsilon_4 \Delta x}{2}} \tag{5.33}$$

$$\frac{\delta \mathbf{F}}{\delta x}\Big|_i = \frac{(\mathbf{F}_{i+\frac{1}{2}} + \mathbf{F}_{i+\frac{3}{2}}) - (\mathbf{F}_{i-\frac{1}{2}} + \mathbf{F}_{i-\frac{3}{2}})}{\frac{\epsilon_1 \Delta x}{2} + \epsilon_2 \Delta x + \epsilon_3 \Delta x + \frac{\epsilon_4 \Delta x}{2}} \tag{5.34}$$

Even for a one-dimensional case, it is obvious that further simplifications cannot convert the expression to an "equivalent" finite volume expression. In particular, for these cases, the "virtual" volumes now overlap unlike for the 3-point stencil where they are non-overlapping (as also for FVM). Nevertheless, for the 4-point stencil which has two neighbours on the right and one neighbour on the left, the "symmetry" of the neighbourhood stencil is itself violated which would mean that C1 condition would not be satisfied. In contrast, the 5-point stencil (with two neighbours on either side) maintains a "symmetric" neighbourhood. Numerical experiments in Section 5.7 show that the weighted LSFD-U does show discrete conservation with a "symmetric" neighbourhood while "asymmetric" neighbourhoods lead to a non-conservative solution. Although these results are limited to only one-dimensional problems, it must be remarked that this surprisingly simple result which states that inverse-distance weights can make LSFD-U discretely conservative on non-uniform meshes, has never been previously reported. Furthermore, this result appears to be applicable to all "symmetric" neighbourhoods on non-uniform point distributions, as will be numerically demonstrated, despite the theoretical arguments being only limited to a 3-point stencil. Unlike the approach outlined in Chiu et al. where the coefficients $a_{i,j}$ are evaluated using a specific procedure, our results indicate that a simple geometric weighting in conjunction with LSFD-U approach and a "symmetric" neighbourhood could also be a discretely conservative meshless framework.

5.7 Investigations on discrete conservation

We shall numerically investigate the unweighted and weighted LSFD-U scheme on different non-uniform point distributions to highlight the role of neighbourhood symmetry and geometric weighting on the numerical solutions. The first-order accurate AUSM scheme with explicit Euler time-stepping is employed for all studies and three different problems viz. Sod shock-tube problem, Brio-Wu problem and the Ryu and Jones problem-2a are investigated on three different non-uniform point distributions. These test cases have been previously described at length in Chapter 3 and in this section we only provide additional details relevant to the meshfree framework employed in the simulations.

5.7.1 Sod shock tube problem

As a first test case, we consider the hydrodynamic shock tube problem. We choose a point distribution with the distance between adjacent points alternating between two values Δx_1 and Δx_2. We choose $\Delta x_1 = (1-\epsilon)L/n$ and $\Delta x_2 = (1+\epsilon)L/n$, where L is the length of the tube, n is the total number of points and ϵ is considered to be 0.2, so that the point distribution is indeed quite non-uniform. Such a checkerboard pattern of point distribution is quite unnatural, but is chosen herein to explore the issue of discrete conservation. Simulations are carried out on a [0,1] domain with 400 points and a time step of $\Delta t = 10^{-4}$. The density and pressure profiles at $t = 0.1$ are shown in Figure 5.7. It must be mentioned that a 3-point stencil is chosen in this study, with the neighbours chosen one each on either side. We observe that results from unweighted LSFD-U shows deviations from those obtained using FVM. A closer look shows that while there are discrepancies in the locations of discontinuities as well as rarefaction, one can notice that the shock location is clearly distinct from that computed by FVM. The results from the weighted LSFD-U are however in agreement with those of the FVM and hence give the right shock location. This supports the theoretical arguments in the earlier sections pertaining to conservation and also proves that a "symmetric" neighbourhood does not necessarily suffice for discrete conservation in the LSFD-U framework.

5.7.2 Brio and Wu problem

We now consider the MHD analogue of the above problem on a grid generated by an exponential stretching function. We use a stretching function which maps the unit interval onto itself so as to cluster points more densely in certain regions. This function is,

$$x(u) = \frac{e^{\beta u} - 1}{e^{\beta} - 1}, \tag{5.35}$$

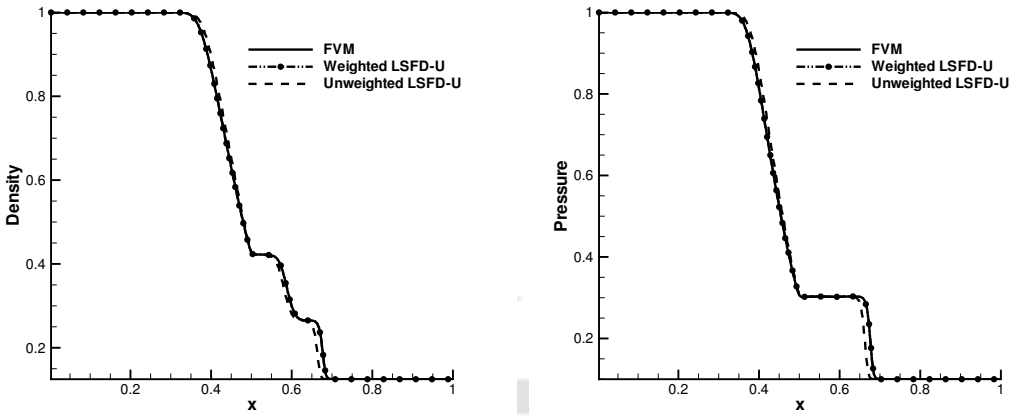

Figure 5.7. Solutions for Sod shock tube problem using a 3-point stencil on a checkerboard pattern of point distribution

and defines the point distribution for this study. The parameter $\beta > 0$ is chosen to control the extent of the stretching. We have varied the number of points on the unit length by varying β with $1 \leq \beta \leq 3$. Our aim is to use a refined point distribution in the regions of shocks and other discontinuities while applying a coarser point distribution in regions of smooth flow. We again choose a "symmetric" neighbourhood where every point has two neighbours, one on the left and one on the right, to calculate the flux gradient. Numerical solutions obtained for 400 points on a domain of unit length and $\Delta t = 10^{-4}$ are shown at $t = 0.1$ in Figure 5.8. These solutions reinforce the lack of conservation with a "symmetric" neighbourhood when unweighted LSFD-U is used for MHD problems. In particular, one can see that the compound wave is displaced compared with the finite volume solutions and these are clear from the density and magnetic field distributions. The weighted LSFD-U with inverse distance weights is however conservative and shows results that are in excellent agreement with those from FVM.

5.7.3 Ryu and Jones problem 2a

We focus our studies for this test case on 4- and 5-point stencils to investigate the discrete conservation property of LSFD-U. In a 4-point stencil, the neighbourhood has three neighbours with two on the left and one on the right. A 5-point stencil has a "symmetric" neighbourhood with two neighbours each on either side. We must emphasise again that the "symmetry" of the neighbourhood refers to equal number of neighbours on either sides of any point and not to their physical locations. In these studies, we employ an uniform point distribution for simulations with the 4-point stencil while a non-uniform point distribution

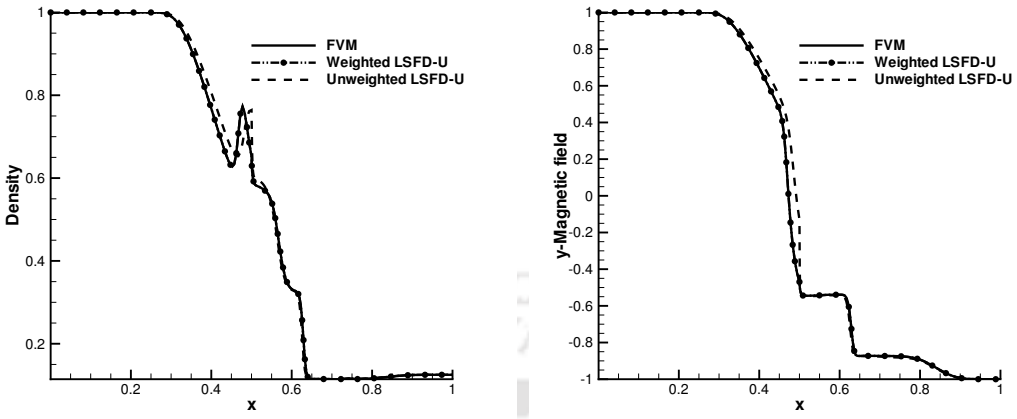

Figure 5.8. Solutions for Brio Wu shock tube problem using a 3-point stencil on an exponentially stretched grid

generated using the hyperbolic tangent function given by

$$x(u) = 1 + \frac{\tanh\left(\delta(u-1)/2\right)}{\tanh(\delta/2)}, \tag{5.36}$$

is used for simulations with the 5-point stencil. In the above function δ is used to control the extent of the stretching. For computations on 5-point stencil, we choose the length of the domain as unity with varying the value of β between 3 and 5 to generate a non-uniform point distribution with 512 nodes. Simulations are carried out with a time step of $\Delta t = 10^{-4}$ up to $t = 0.2$. One can see from the results in Figure 5.9 that the weighted LSFD-U results agree well with the FVM results, while the unweighted LSFD-U shows discrepancies, especially in the location of the fast shock. A closer look shows that the weighted LSFD-U and FVM results do not overlap on one another; rather, the two are in excellent agreement giving correct average locations for discontinuities, although the meshfree results appear to be marginally more diffusive. This observation is also interesting because unlike on a 3-point stencil, it is not possible to reduce the expressions for flux derivatives for weighted LSFD-U to those similar for FVM on a 5-point stencil. Despite the non-overlapping nature of the "virtual" volumes in the case of a 5-point stencil, the use of geometric weighting is able to reproduce the FVM results on this non-uniform point distribution, which highlights that the weighted LSFD-U is discretely conservative. On the contrary, with the 4-point stencil, the "asymmetry" of the nieghbourhood clearly makes both the weighted and unweighted LSFD-U non-conservative even on an uniform point distribution as demonstrated in Figure 5.10. It is therefore evident that the "symmetry" of the neighbourhood plays a major role in enforcing discrete conservation although it would still necessitate the use of inverse distance weighting on non-uniform

point distributions to achieve this result. Although not shown here, it is easy to see that the unweighted LSFD-U with a 5-point stencil on an uniform point distribution would also be conservative, whereas the weighted LSFD-U with a 4-point stencil on the same point distribution is non-conservative.

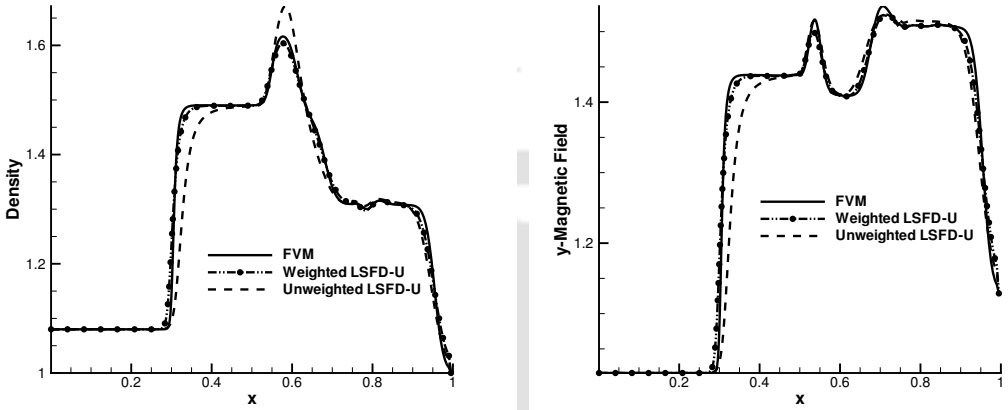

Figure 5.9. Solutions for Ryu and Jones problem 2a using a 5-point stencil on a tangentially stretched grid

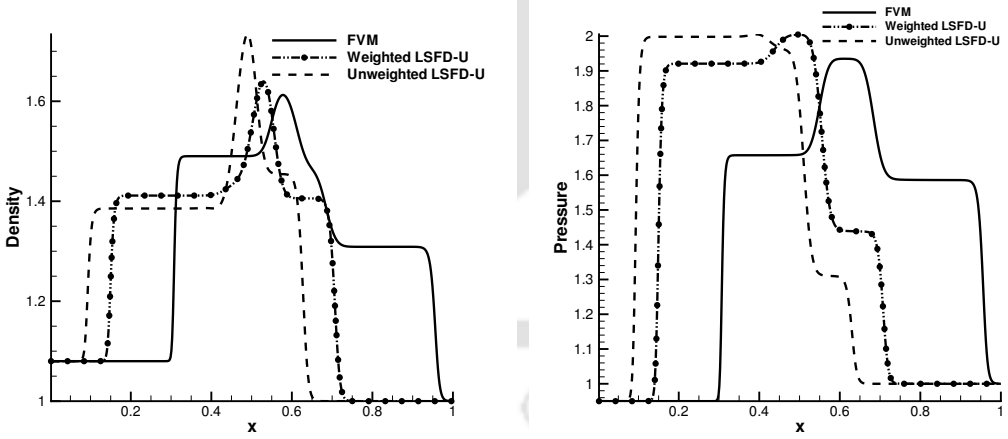

Figure 5.10. Solutions for Ryu and Jones problem 2a using a 4-point stencil on a uniform grid

The above studies show that one needs to employ "symmetric" neighbourhoods and inverse-distance weighted LSFD-U on non-uniform point distributions to achieve discrete conservation. The numerical results show that a lack of either of these could lead to varying levels of conservation errors for MHD problems.

While the use of inverse distance weighting in least-squares approaches has been a common practice for a long time, its use to enforce discrete conservation in meshfree frameworks is a new observation. Importantly, we also link these observations to a pair of necessary conditions that can help form guidelines for a more general conservative LSFD-U framework. The results from these studies, although of a limited nature, can help pave the way for developing discretely conservative meshfree framerworks in multi-dimensions.

To summarise, in this chapter we propose a meshfree framework for numerical simulations of ideal MHD flows. The framework is based on the Least-Squares-Based Upwind Finite Difference method (LSFD-U), which employs a global stencil as opposed to one-sided stencil on any arbitrary point distribution. A first-order AUSM scheme is used to compute the fluxes at the fictitious interfaces along with explicit Euler method for time-marching. The LSFD-U approach, with and without weights, is shown to be conservative on an uniform distribution with a "symmetric" neighbourhood. On non-uniform point distributions, the use of inverse-distance weighting along with a "symmetric" neighbourhood is necessary to enforce discrete conservation. The importance of neighbourhood stencil and weighting on discrete conservation are numerically highlighted by solving three different shock tube problems on differently generated non-uniform point distributions.

6

Conclusions and Future Scope

The work embodied in this thesis discusses developments of flow solvers in finite volume and meshfree frameworks for ideal MHD. The novel aspects of the finite volume flow solver include the construction of a new flux scheme based on wave-particle splitting in one- and two-dimensions, investigations of a hyperbolic divergence cleaning approach on structured and unstructured meshes for enforcing solenoidality constraint on the magnetic field and devising a conservative meshfree framework for 1D MHD on arbitrary point distributions. We summarise the salient contributions of this thesis below.

1. A new numerical flux splitting scheme exploiting wave-particle behaviour has been developed for MHD flows. This scheme, referred to as the Magneto-acoustic Wave Particle Splitting (MWPS) scheme, is an extension of the Acoustic Flux Vector Splitting (AFVS) scheme for ideal MHD. However, the non-homogeneity of the fluxes, non-convexity of the system of equations of ideal MHD, and the associated physics logically suggest a tripartite numerical treatment of the flux vector. Accordingly, a three-way decomposition of the flux vector is effected for separate numerical treatment through simple upwinding, flux-vector splitting and 'central-differencing'. The resulting flux formula is convenient to program and the computational cost is relatively low.

2. The regulation of numerical diffusion to strike a balance between accuracy and stability is important for any numerical scheme. The MWPS scheme, by construction, inherently allows explicit but automatic limiting of numerical diffusion based on the jumps in Mach number and density. This allows the implementation of a more accurate first-order MWPS scheme for MHD flows. The second-order accurate MWPS scheme has also been devised and implemented in the present study by employing the ideas of limited linear reconstruction. While a solution-dependent weighted least squares approach has been adopted for this purpose in 1D, higher-order accuracy in 2D is realised using the Venkatakarishnan slope limiter in conjunction with Green-Gauss reconstruction of gradients. The second-order MWPS scheme is numerically demonstrated to be a good trade-off between

accuracy and stability for a range of MHD problems even without the use of the additional dissipation regulation mechanisms.

3. The solenoidality criterion for the magnetic field must necessarily be enforced in MHD simulations at the discrete level. While it is identically satisfied in 1D, a technique based on artificial compressibility analogy (ACA) is generally necessary to satisfy this constraint in 2D. For steady problems, the extent to which the constraint is satisfied, is of the order of the steady-state residual. However, the use of an explicit dual-time-stepping approach for unsteady flows with a fixed number of sub-iterations means that the divergence errors are not necessarily machine zero at the end of every physical time step. The numerical experiments have shown that 200 sub-iterations suffice in most cases and that the errors are acceptable since they lead to physically consistent and accurate solutions. Our investigations also demonstrate that the violation of the solenoidality constraint at each time step for unsteady flows leads to spurious numerical solutions and strong violation of flow physics.

4. The MWPS scheme has been implemented in an in-house compressible MHD flow solver which is based on the finite volume framework. Numerical studies have been carried out on several canonical and benchmark problems in one- and two-dimensions, with the latter studies carried out on both structured and unstructured grids. The second-order MWPS scheme is found to be quite accurate and robust, and is comparable to the AUSM scheme for many problems and superior to it for some cases such as the low β problem where the AUSM scheme fails to produce a physical result. The MWPS scheme has also been compared with a class of central schemes where the superiority of the former is visible for cases with low thermal pressures, although isolated discontinuities cannot be exactly resolved owing to the "residual" numerical dissipation inherent in the MWPS scheme. The studies provide conclusive evidence that the proposed MWPS scheme is a promising alternative to central schemes and other wave-particle splitting schemes for MHD.

5. The thesis also investigates a meshfree least-squares-based approach, namely, LSFD-U for computing 1D ideal MHD flows. This is essentially a finite-difference method applied to a cloud of points that need not be arranged in any particular pattern as needed in FVM or conventional FDM. However, such a method suffers from the problem of lack of discrete conservation. This is a long outstanding problem that is defying solution till date. Researchers usually use a densely clustered collection of points to circumvent this issue and very few attempts have been made to address the core problem directly by formulating a set of rules, fulfilment of which would lead to

discrete conservation. This thesis makes a first attempt to address this important issue albeit in one-dimension. We show that the meshfree approach is equivalent to the finite volume method on uniform point distribution with a "symmetric" neighbourhood, which consists of a stencil containing equal number of points on either side of the point concerned. We highlight that even for an uniform distribution of points, discrete conservation cannot be obtained if the difference stencil is "unsymmetric"- containing unequal number of points on either side. The problem is shown to be further exacerbated and erroneous solutions are obtained if the point distribution is non-uniform and the difference stencil remains "unsymmteric". We propose a set of criteria to obtain a conservative meshfree framework and show that the use of inverse-distance weights with a "symmetric" stencil could fulfil these criteria thereby leading to a discretely conservative scheme on any arbitrary distribution of points. The theoretical arguments are supported by numerical studies which also show that the choice of a "symmetric" neighbourhood is critical in developing a conservative meshfree scheme which gives physically correct locations and strength of discontinuities in MHD flows. Though this issue has not been explored and resolved for multi-dimensions in the thesis, the present work makes significant progress in one-dimension. We believe the present effort is an important stepping stone in the long-continuing quest for a conservative meshfree scheme and hope that it will facilitate the development of a conservative meshless approaches for multi-dimensional MHD in the future.

Scope for future work

While the work in this thesis largely fulfils the objectives laid down in the beginning, it also provides ample scope and opportunities for several improvements in the future. While several avenues of future research can be envisaged, some of the possible directions are briefly outlined below.

1. The numerical diffusion is a delicate trade-off between accuracy and robustness. The MWPS scheme does have options to regulate numerical diffusion, and optimisation of the regulating mechanisms with an aim to develop optimally-diffusive flux schemes would improve the performance even in case of spatially first-order-accurate solvers.

2. Developing entropy-stable finite volume schemes for ideal MHD would help in ensuring a robust and accurate solution approach for challenging problems such as the strong blast case and those where strong discontinuities and/or large magnetic fields are involved.

3. Despite the thesis describing the implementation of a robust, generic and accurate MHD flow solver for 2D flows, the higher magnitude of magnetic divergence error in 2D unsteady problems remains a major concern especially on unstructured grids. While we did not observe physically anomalous solutions in our present studies, it is desirable to evolve a numerical framework that can lead to very low $\nabla \cdot \mathbf{B}$ errors in domains with arbitrary polygonal meshes which therefore satisfies the discrete solenoidality constraint. This may be possible through the use of an implicit discretisation as also in [1] or by adopting a completely different divergence cleaning approach or even hybridising some of the existing techniques for divergence cleaning.

4. The thesis has extensively studied problems in ideal MHD and it is possible to extend the numerical framework herein to study resistive MHD where the effects of fluid viscosity and electrical resistivity are suitably accounted for.

5. It is also desirable to extend the compressible ideal MHD flow solver to three dimensions in conjunction with a good divergence cleaning approach. Considering the wide range of applications in aerospace industry, such a flow solver could be an useful design tool for primary investigations for MHD flows.

6. Extending the conservative meshfree approach to higher dimensions poses a non-trivial and challenging problem with additional difficulties in satisfying the solenoidality constraint on the magnetic field at every node in a cloud of points. The discrete conservation seems possible to be mimicked using the inverse distance weighting on non-uniform Cartesian point distributions possibly with the help of a dimensional-splitting approach, although thorough investigations in this direction are deemed necessary to verify this claim.

A
Appendix

A.1 Eigen-structure of the flux Jacobian $\mathbf{A}^p$ for 1D MWPS

The flux Jacobian of the pressure fluxes $\mathbf{F}^p$ is

$$\mathbf{A}^p = \frac{\partial \mathbf{F}^p}{\partial \mathbf{U}}$$

which may be evaluated as,

$$\mathbf{A}^p = \begin{bmatrix} 0 & 0 & 0 & 0 & 0 & 0 & 0 \\ \frac{\gamma-1}{2}V^2 & -(\gamma-1)u & -(\gamma-1)v & -(\gamma-1)w & 0 & 0 & (\gamma-1) \\ 0 & 0 & 0 & 0 & 0 & 0 & 0 \\ 0 & 0 & 0 & 0 & 0 & 0 & 0 \\ 0 & 0 & 0 & 0 & 0 & 0 & 0 \\ 0 & 0 & 0 & 0 & 0 & 0 & 0 \\ a^p_{71} & a^p_{72} & -(\gamma-1)uv & -(\gamma-1)uw & 0 & 0 & (\gamma-1)u \end{bmatrix}$$

where,

$$a^p_{71} = -\frac{Pu}{\rho} + \frac{\gamma-1}{2}uV^2 - \frac{\gamma-1}{2}\frac{B^2 u}{\rho}$$

$$a^p_{72} = \frac{P}{\rho} + \frac{\gamma-1}{2}\frac{B^2}{\rho} - (\gamma-1)u^2$$

The matrix of eigenvalues for this Jacobian is,

$$\mathbf{\Lambda}^p = \begin{bmatrix} 0 & 0 & 0 & 0 & 0 & 0 & 0 \\ 0 & 0 & 0 & 0 & 0 & 0 & 0 \\ 0 & 0 & 0 & 0 & 0 & 0 & 0 \\ 0 & 0 & 0 & 0 & 0 & 0 & 0 \\ 0 & 0 & 0 & 0 & 0 & 0 & 0 \\ 0 & 0 & 0 & 0 & 0 & -\sqrt{\frac{\gamma-1}{\gamma}}a^* & 0 \\ 0 & 0 & 0 & 0 & 0 & 0 & \sqrt{\frac{\gamma-1}{\gamma}}a^* \end{bmatrix}$$

A.2 Eigen-structure of the flux Jacobian A^m for 1D MWPS

The flux Jacobian of the magnetic fluxes $\mathbf{F}^m$ is

$$\mathbf{A}^m = \frac{\partial \mathbf{F}^m}{\partial \mathbf{U}} \tag{A.1}$$

and is determined as,

$$\mathbf{A}^m = \begin{bmatrix} 0 & 0 & 0 & 0 & 0 & 0 & 0 \\ 0 & 0 & 0 & 0 & (2-\gamma)B_y & (2-\gamma)B_z & 0 \\ 0 & 0 & 0 & 0 & -B_x & 0 & 0 \\ 0 & 0 & 0 & 0 & 0 & -B_x & 0 \\ \frac{vB_x}{\rho} & 0 & -\frac{B_x}{\rho} & 0 & 0 & 0 & 0 \\ \frac{wB_x}{\rho} & 0 & 0 & -\frac{B_x}{\rho} & 0 & 0 & 0 \\ a^m_{71} & a^m_{72} & -\frac{B_xB_y}{\rho} & -\frac{B_xB_z}{\rho} & a^m_{75} & a^m_{76} & 0 \end{bmatrix}$$

where,

$$a^m_{71} = -(1-\frac{\gamma}{2})\frac{uB^2}{\rho} + \frac{B_x}{\rho}(uB_x + vB_y + wB_z)$$

$$a^m_{72} = (1-\frac{\gamma}{2})\frac{B^2}{\rho} - \frac{B_x^2}{\rho}$$

$$a^m_{75} = (2-\gamma)uB_y - vB_x$$

$$a^m_{76} = (2-\gamma)uB_z - wB_x$$

We remark that this Jacobian is a defective matrix as a result of which it cannot be diagonalised. The matrix of eigenvalues is given by,

$$\mathbf{\Lambda}^m = \begin{bmatrix} 0 & 0 & 0 & 0 & 0 & 0 & 0 \\ 0 & 0 & 0 & 0 & 0 & 0 & 0 \\ 0 & 0 & 0 & 0 & 0 & 0 & 0 \\ 0 & 0 & 0 & -\frac{B_x}{\sqrt{\rho}} & 0 & 0 & 0 \\ 0 & 0 & 0 & 0 & -\frac{B_x}{\sqrt{\rho}} & 0 & 0 \\ 0 & 0 & 0 & 0 & 0 & \frac{B_x}{\sqrt{\rho}} & 0 \\ 0 & 0 & 0 & 0 & 0 & 0 & \frac{B_x}{\sqrt{\rho}} \end{bmatrix}$$

A.3 Discontinuities in MHD and jumps in primitive variables

Table A.1 gives a comprehensive overview of the possible discontinuities in MHD flows and the jumps of different variables across them. A ✓ denotes that the

Type of discontinuity	ρ	u	v	w	B_y	B_z	P
Fast shock	✓	✓	✓	–	✓(+)	–	✓
Switch-on fast shock	✓	✓	✓	–	✓(+)	–	✓
Slow shock	✓	✓	✓	–	✓(–)	–	✓
Switch-off slow shock	✓	✓	✓	–	✓(–)	–	✓
Tangential discontinuity	✓	–	✓	–	✓	✓	✓
Magnetosonic shock	✓	✓	–	–	✓	✓	✓
Rotational discontinuity	–	–	✓	✓	✓	✓	–
Hydrodynamic shock	✓	✓	✓	✓	–	–	✓

Table A.1. Discontinuities in MHD and jumps in different primitive variables across them. For the switch-on and switch-off shocks, the y-magnetic field is zero in the pre- and post-shock regions respectively.

property jumps across the discontinuity with the $(+)$ and $(-)$ signs indicative of whether the property increases or decreases through the jump. This table also serves as a quick reference for researchers in identifying the type of discontinuity based on the spatial variation of the properties of interest, even in multi-dimensional flows.

A.4 Numerical diffusion of the 1D MWPS scheme

In order to understand the structure of numerical diffusion inherent in the second-order MWPS scheme employed for simulations in this study, we first consider the simpler problem of diffusion from the first-order scheme. The maximum possible numerical diffusion from the MWPS scheme occurs when it is implemented as a first-order scheme with values of ϕ and ψ everywhere being unity. For the isolated discontinuity test cases, the diffusion terms become,

$$D_1 = \sqrt{\frac{\gamma-1}{\gamma}}\left(a_L^*\rho_L - a_R^*\rho_R\right) - \frac{1}{2}S\left(\rho_R - \rho_L\right)$$

$$D_2 = \sqrt{\frac{\gamma-1}{\gamma}}\left(a_L^*\rho_L u_L - a_R^*\rho_R u_R\right) - \frac{1}{2}S\left(\rho_R u_R - \rho_L u_L\right)$$

$$D_3 = \sqrt{\frac{\gamma-1}{\gamma}}\left(a_L^*\rho_L v_L - a_R^*\rho_R v_R\right) - \frac{1}{2}S\left(\rho_R v_R - \rho_L v_L\right)$$

$$D_4 = \sqrt{\frac{\gamma-1}{\gamma}}\left(a_L^*\rho_L w_L - a_R^*\rho_R w_R\right) - \frac{1}{2}S\left(\rho_R w_R - \rho_L w_L\right)$$

$$D_5 = \sqrt{\frac{\gamma-1}{\gamma}}\left(a_L^* B_{yL} - a_R^* B_{yR}\right) - \frac{1}{2}S\left(B_{yR} - B_{yL}\right)$$

$$D_6 = \sqrt{\frac{\gamma-1}{\gamma}}\left(a_L^* B_{zL} - a_R^* B_{zR}\right) - \frac{1}{2}S\left(B_{zR} - B_{zL}\right)$$

$$D_7 = \frac{1}{2\sqrt{\gamma(\gamma-1)}}\left(P_L a_L^* - P_R a_R^*\right) + \frac{1}{2}\sqrt{\frac{\gamma-1}{\gamma}}\left(a_L^*\rho_L V_L^2 - a_R^*\rho_R V_R^2\right) + \frac{1}{4}\sqrt{\frac{\gamma-1}{\gamma}}\left(B_L^2 a_L^* - B_R^2 a_R^*\right) - \frac{1}{2}S\left(E_R - E_L\right)$$

where, $S = \max\left(\frac{B_x}{\sqrt{\rho_L}}, \frac{B_x}{\sqrt{\rho_R}}\right)$. It is easy to see that D_1 and D_7 are the only non-zero terms for the contact discontinuity problem whereas for the Alfvén wave discontinuity problem, all terms except D_3 and D_5 are identically zero. The use of a solution-dependent weighted least squares reconstruction, which makes the scheme second-order accurate, introduces just enough "anti-diffusion" into the scheme such that the net numerical diffusion (which is lowered) is sufficient to capture the discontinuities reasonably accurately (although not exactly) without compromising the stability and positivity preservation characteristics of the flow solver.

A.5 Eigen-structure of the flux Jacobian $\mathbf{A}_\perp^p$ for 2D MWPS

The flux Jacobian of the pressure fluxes $\mathbf{F}_\perp^p$ is

$$\mathbf{A}_\perp^p = \frac{\partial \mathbf{F}_\perp^p}{\partial \mathbf{U}}$$

which may be evaluated as,

$$\mathbf{A}_\perp^p = \begin{bmatrix} 0 & 0 & 0 & 0 & 0 & 0 & 0 & 0 \\ \frac{\gamma-1}{2}V^2 n_x & -(\gamma-1)un_x & -(\gamma-1)vn_x & -(\gamma-1)wn_x & 0 & 0 & 0 & (\gamma-1)n_x \\ \frac{\gamma-1}{2}V^2 n_y & -(\gamma-1)un_y & -(\gamma-1)vn_y & -(\gamma-1)wn_y & 0 & 0 & 0 & (\gamma-1)n_y \\ 0 & 0 & 0 & 0 & 0 & 0 & 0 & 0 \\ 0 & 0 & 0 & 0 & 0 & 0 & 0 & 0 \\ 0 & 0 & 0 & 0 & 0 & 0 & 0 & 0 \\ 0 & 0 & 0 & 0 & 0 & 0 & 0 & 0 \\ a_{\perp 81}^{\ p} & a_{\perp 82}^{\ p} & a_{\perp 83}^{\ p} & -(\gamma-1)wu_\perp & 0 & 0 & 0 & (\gamma-1)u_\perp \end{bmatrix}$$

where,

$$a_{\perp 81}^{\ p} = -\frac{Pu_\perp}{\rho} + \frac{\gamma-1}{2}V^2 u_\perp - \frac{\gamma-1}{2}\frac{B^2 u_\perp}{\rho}$$

$$a_{\perp 82}^{\ p} = \frac{Pn_x}{\rho} + \frac{\gamma-1}{2}\frac{B^2 n_x}{\rho} - (\gamma-1)uu_\perp$$

$$a_{\perp 83}^{\ p} = \frac{Pn_y}{\rho} + \frac{\gamma-1}{2}\frac{B^2 n_y}{\rho} - (\gamma-1)vu_\perp$$

The matrix of eigenvalues for this Jacobian is,

$$\mathbf{\Lambda}_{\perp}^{p} = \begin{bmatrix} 0 & 0 & 0 & 0 & 0 & 0 & 0 & 0 \\ 0 & 0 & 0 & 0 & 0 & 0 & 0 & 0 \\ 0 & 0 & 0 & 0 & 0 & 0 & 0 & 0 \\ 0 & 0 & 0 & 0 & 0 & 0 & 0 & 0 \\ 0 & 0 & 0 & 0 & 0 & 0 & 0 & 0 \\ 0 & 0 & 0 & 0 & 0 & 0 & 0 & 0 \\ 0 & 0 & 0 & 0 & 0 & 0 & -\sqrt{\frac{\gamma-1}{\gamma}}a^{*} & 0 \\ 0 & 0 & 0 & 0 & 0 & 0 & 0 & \sqrt{\frac{\gamma-1}{\gamma}}a^{*} \end{bmatrix}$$

A.6 Eigen-structure of the flux Jacobians $\mathbf{A}_{\perp 1}^{\ m}$ and $\mathbf{A}_{\perp 2}^{\ m}$ for 2D MWPS

The flux Jacobian of the magnetic fluxes $\mathbf{F}_{\perp 1}^{\ m}$ is

$$\mathbf{A}_{\perp 1}^{\ m} = \frac{\partial \mathbf{F}_{\perp 1}^{\ m}}{\partial \mathbf{U}} \tag{A.2}$$

and is determined as,

$$\mathbf{A}_{\perp 1}^{\ m} = \begin{bmatrix} 0 & 0 & 0 & 0 & 0 & 0 & 0 & 0 \\ 0 & 0 & 0 & 0 & a_{\perp 25}^{\ m} & a_{\perp 26}^{\ m} & (2-\gamma)B_z n_x & 0 \\ 0 & 0 & 0 & 0 & a_{\perp 35}^{\ m} & a_{\perp 36}^{\ m} & (2-\gamma)B_z n_y & 0 \\ 0 & 0 & 0 & 0 & -B_z n_x & -B_z n_y & -B_{\perp} & \\ 0 & 0 & 0 & 0 & 0 & 0 & 0 & 0 \\ 0 & 0 & 0 & 0 & 0 & 0 & 0 & 0 \\ \frac{wB_{\perp}}{\rho} & 0 & 0 & -\frac{B_{\perp}}{\rho} & -wn_x & -wn_y & 0 & 0 \\ a_{\perp 81}^{\ m} & a_{\perp 82}^{\ m} & a_{\perp 83}^{\ m} & -\frac{B_{\perp}B_z}{\rho} & a_{\perp 85}^{\ m} & a_{\perp 86}^{\ m} & a_{\perp 87}^{\ m} & 0 \end{bmatrix}$$

where,

$$a_{\perp 25}^{\ m} = -\gamma B_x n_x - B_y n_y$$

$$a_{\perp 26}^{\ m} = (2-\gamma)B_y n_x - B_x n_y$$

$$a_{\perp 35}^{\ m} = (2-\gamma)B_x n_y - B_y n_x$$

$$a_{\perp 36}^{\ m} = -\gamma B_y n_y - B_x n_x$$

$$a_{\perp 81}^{\ m} = -(1-\frac{\gamma}{2})\frac{u_{\perp}B^2}{\rho} + \frac{B_{\perp}}{\rho}(uB_x + vB_y + wB_z)$$

$$a_{\perp 82}^{m} = (1 - \frac{\gamma}{2})\frac{B^2 n_x}{\rho} - \frac{B_x B_\perp}{\rho}$$

$$a_{\perp 83}^{m} = (1 - \frac{\gamma}{2})\frac{B^2 n_y}{\rho} - \frac{B_y B_\perp}{\rho}$$

$$a_{\perp 85}^{m} = (2-\gamma)u_\perp B_x - uB_\perp - (uB_x + vB_y + wB_z)n_x$$

$$a_{\perp 86}^{m} = (2-\gamma)u_\perp B_y - vB_\perp - (uB_x + vB_y + wB_z)n_y$$

$$a_{\perp 87}^{m} = (2-\gamma)u_\perp B_z - wB_\perp$$

We remark that this Jacobian is a defective matrix as a result of which it cannot be diagonalised. The matrix of eigenvalues is given by,

$$\mathbf{\Lambda}_{\perp 1}^{m} = \begin{bmatrix} 0 & 0 & 0 & 0 & 0 & 0 & 0 & 0 \\ 0 & 0 & 0 & 0 & 0 & 0 & 0 & 0 \\ 0 & 0 & 0 & 0 & 0 & 0 & 0 & 0 \\ 0 & 0 & 0 & 0 & 0 & 0 & 0 & 0 \\ 0 & 0 & 0 & 0 & 0 & 0 & 0 & 0 \\ 0 & 0 & 0 & 0 & 0 & 0 & 0 & 0 \\ 0 & 0 & 0 & 0 & 0 & 0 & -\frac{B_\perp}{\sqrt{\rho}} & 0 \\ 0 & 0 & 0 & 0 & 0 & 0 & 0 & \frac{B_\perp}{\sqrt{\rho}} \end{bmatrix}.$$

The flux Jacobian of the magnetic fluxes $\mathbf{F}_{\perp 2}^{m}$ is

$$\mathbf{A}_{\perp 2}^{m} = \frac{\partial \mathbf{F}_{\perp 2}^{m}}{\partial \mathbf{U}} \tag{A.3}$$

which is determined as,

$$\mathbf{A}_{\perp 2}^{m} = \begin{bmatrix} 0 & 0 & 0 & 0 & 0 & 0 & 0 & 0 \\ 0 & 0 & 0 & 0 & 0 & 0 & 0 & 0 \\ 0 & 0 & 0 & 0 & 0 & 0 & 0 & 0 \\ 0 & 0 & 0 & 0 & 0 & 0 & 0 & 0 \\ \frac{uB_\perp}{\rho} & -\frac{B_\perp}{\rho} & 0 & 0 & -un_x & -un_y & 0 & 0 \\ \frac{vB_\perp}{\rho} & 0 & -\frac{B_\perp}{\rho} & 0 & -vn_x & -vn_y & 0 & 0 \\ 0 & 0 & 0 & 0 & 0 & 0 & 0 & 0 \\ 0 & 0 & 0 & 0 & 0 & 0 & 0 & 0 \end{bmatrix}$$

The matrix of eigenvalues is given by,

$$\mathbf{\Lambda}_{\perp 2}^{m} = \begin{bmatrix} 0 & 0 & 0 & 0 & 0 & 0 & 0 & 0 \\ 0 & 0 & 0 & 0 & 0 & 0 & 0 & 0 \\ 0 & 0 & 0 & 0 & 0 & 0 & 0 & 0 \\ 0 & 0 & 0 & 0 & 0 & 0 & 0 & 0 \\ 0 & 0 & 0 & 0 & 0 & 0 & 0 & 0 \\ 0 & 0 & 0 & 0 & 0 & 0 & 0 & 0 \\ 0 & 0 & 0 & 0 & 0 & 0 & 0 & 0 \\ 0 & 0 & 0 & 0 & 0 & 0 & 0 & -u_{\perp} \end{bmatrix}$$

A.7 Sample MATHEMATICA scripts to determine eigenvalues of $\mathbf{A}_{\perp}^{p}$ and pressure fluxes for 2D MWPS

We provide below a sample script using MATHEMATICA [77] to compute the eigen-structure of $\mathbf{A}_{\perp}^{p}$ and the corresponding pressure fluxes for 2D MWPS.

Denoting the flux Jacobian $\mathbf{A}_{\perp}^{p}$ as AA,

$AA = \{\{0,0,0,0,0,0,0,0\},$
$\{((g-1)/2)*(u^2+v^2+w^2)*nx, -(g-1)*u*nx, -(g-1)*v*nx, -(g-1)*w*nx, 0, 0, 0, (g-1)*nx\},$
$\{((g-1)/2)*(u^2+v^2+w^2)*ny, -(g-1)*u*ny, -(g-1)*v*ny, -(g-1)*w*ny, 0, 0, 0, (g-1)*ny\},$
$\{0,0,0,0,0,0,0,0\},$
$\{0,0,0,0,0,0,0,0\},$
$\{0,0,0,0,0,0,0,0\},$
$\{0,0,0,0,0,0,0,0\},$
$\{(g-1)*((-u*E/r+u*(u^2+v^2+w^2))*nx+(-v*E/r+v*(u^2+v^2+w^2))*ny), (g-1)*(E*nx/r-(3*u^2+v^2+w^2)*nx/2-u*v*ny), (g-1)*(E*ny/r-(u^2+3*v^2+w^2)*ny/2-u*v*nx), -(g-1)*(u*w*nx+v*w*ny), 0, 0, 0, (g-1)*(u*nx+v*ny)\}\};$

BB = Eigenvalues[AA]

$\{0,0,0,0,0,0,-4Sqrt[2]Sqrt[nx^2+ny^2](-(1/(8r^3))+g/(8r^3))r^(5/2)Sqrt[2E-ru^2-rv^2-rw^2], 4Sqrt[2]Sqrt[nx^2+ny^2](-(1/(8r^3))+g/(8r^3))r^(5/2)Sqrt[2E-ru^2-rv^2-rw^2]\}$

Simplify[%]

$\{0,0,0,0,0,0,-(((-1+g)Sqrt[nx^2+ny^2]Sqrt[2E-r(u^2+v^2+w^2)])/(Sqrt[2]Sqrt[r])), ((-1+g)Sqrt[nx^2+ny^2]Sqrt[2E-r(u^2+v^2+w^2)])/(Sqrt[2]Sqrt[r])\}$

$\mathbf{\Lambda}_{\perp}^{p}{}^{+}$ is put as

```
PP = {{Sqrt[((g - 1)/g)]*P*a, 0, 0, 0, 0, 0, 0, 0},
{0, Sqrt[((g - 1)/g)]*P*a, 0, 0, 0, 0, 0, 0},
{0, 0, Sqrt[((g - 1)/g)]*P*a, 0, 0, 0, 0, 0},
{0, 0, 0, Sqrt[((g - 1)/g)]*P*a, 0, 0, 0, 0},
{0, 0, 0, 0, Sqrt[((g - 1)/g)]*P*a, 0, 0, 0},
{0, 0, 0, 0, 0, Sqrt[((g - 1)/g)]*P*a, 0, 0},
{0, 0, 0, 0, 0, 0, 0, 0},
{0, 0, 0, 0, 0, 0, 0, Sqrt[((g - 1)/g)]*a}};

CC = Eigenvectors[AA]; DD = Transpose[CC]; EE = Inverse[DD];

GG = {r, r*u, r*v, r*w, Bx, By, Bz, Q}; FF = DD.PP.EE.GG

Simplify[%]
```

$$
\begin{aligned}
&\{-aSqrt[(-1+g)/g]Pr,\\
&-((aSqrt[(-1+g)/g]Sqrt[r](2Sqrt[2]Sqrt[nx^2+ny^2]PSqrt[r]uSqrt[2Q-r(u^2+\\
&v^2+w^2)]+nx(-2Q+r(u^2+v^2+w^2))))/(2Sqrt[2]Sqrt[nx^2+ny^2]Sqrt[2Q-r(u^2+\\
&v^2+w^2)])),\\
&-((aSqrt[(-1+g)/g]Sqrt[r](2Sqrt[2]Sqrt[nx^2+ny^2]PSqrt[r]vSqrt[2Q-r(u^2+\\
&v^2+w^2)]+ny(-2Q+r(u^2+v^2+w^2))))/(2Sqrt[2]Sqrt[nx^2+ny^2]Sqrt[2Q-r(u^2+\\
&v^2+w^2)])),\\
&-aSqrt[(-1+g)/g]Prw,\\
&-aBxSqrt[(-1+g)/g]P,\\
&-aBySqrt[(-1+g)/g]P,\\
&-aBzSqrt[(-1+g)/g]P,\\
&-((aSqrt[(-1+g)/g](2nxSqrt[r]u(-2Q+r(u^2+v^2+w^2))+2nySqrt[r]v(-2Q+\\
&r(u^2+v^2+w^2))+Sqrt[2]Sqrt[nx^2+ny^2]Sqrt[2Q-r(u^2+v^2+w^2)](2Q+(-1+\\
&2P)r(u^2+v^2+w^2))))/(4Sqrt[2]Sqrt[nx^2+ny^2]Sqrt[2Q-r(u^2+v^2+w^2)]))\}
\end{aligned}
$$

The above expression gives the positive part of the pressure fluxes and the negative part may be obtained in a similar fashion. One can also employ similar scripts (involving symbolic manipulation) to obtain the eigen-structure of the magnetic flux Jacobians as well.

References

[1] M. S. Yalim, D. V. Abeele, A. Lani, T. Quintino, and H. Deconinck, "A finite volume implicit time integration method for solving the equations of ideal magnetohydrodynamics for the hyperbolic divergence cleaning approach," *Journal of Computational Physics*, vol. 230, no. 15, pp. 6136–6154, 2011.

[2] T. Miyoshi and K. Kusano, "A multi-state HLL approximate Riemann solver for ideal magnetohydrodynamics," *Journal of Computational Physics*, vol. 208, no. 1, pp. 315–344, 2005.

[3] C. M. Xisto, J. C. Páscoa, and P. J. Oliveira, "A pressure-based method with AUSM-type fluxes for MHD flows at arbitrary Mach numbers," *International Journal for Numerical Methods in Fluids*, vol. 72, no. 11, pp. 1165–1182, 2013.

[4] R. Balasubramanian and K. Anandhanarayanan, "An Ideal Magnetohydrodynamics Solver with Artificial Compressibility Analogy Divergence-Cleaning," in *C.F.D. Symposium 2014, Banglore, India*, 2014.

[5] M. Brio and C. C. Wu, "An upwind differencing scheme for the equations of ideal magnetohydrodynamics," *Journal of Computational Physics*, vol. 75, no. 2, pp. 400–422, 1988.

[6] A. L. Zachary and P. Colella, "A higher-order Godunov method for the equations of ideal magnetohydrodynamics," *Journal of Computational Physics*, vol. 99, no. 2, pp. 341–347, 1992.

[7] W. Dai and P. R. Woodward, "An approximate Riemann solver for ideal magnetohydrodynamics," *Journal of Computational Physics*, vol. 111, no. 2, pp. 354–372, 1994.

[8] D. Ryu and T. W. Jones, "Numerical magnetohydrodynamics in astrophysics: Algorithm and tests for one-dimensional flow," *The Astrophysical Journal*, vol. 442, pp. 228–258, 1995.

[9] P. L. Roe and D. S. Balsara, "Notes on the eigensystem of magnetohydrodynamics," *SIAM Journal on Applied Mathematics*, vol. 56, no. 1, pp. 57–67, 1996.

[10] P. Cargo and G. Gallice, "Roe matrices for ideal MHD and systematic construction of Roe matrices for systems of conservation laws," *Journal of Computational Physics*, vol. 136, no. 2, pp. 446–466, 1997.

[11] D. S. Balsara, "Linearized Formulation of the Riemann Problem for Adiabatic and Isothermal Magnetohydrodynamics," *The Astrophysical Journal Supplement Series*, vol. 116, no. 1, p. 119, 1998.

[12] V. Honkkila and P. Janhunen, "HLLC solver for ideal relativistic MHD," *Journal of Computational Physics*, vol. 223, no. 2, pp. 643–656, 2007.

[13] K. F. Gurski, "An HLLC-type approximate Riemann solver for ideal magnetohydrodynamics," *SIAM Journal on Scientific Computing*, vol. 25, no. 6, pp. 2165–2187, 2004.

[14] S. Li, "An HLLC Riemann solver for magneto-hydrodynamics," *Journal of Computational Physics*, vol. 203, no. 1, pp. 344–357, 2005.

[15] D. S. Balsara, "Multidimensional HLLE Riemann solver: Application to Euler and magnetohydrodynamic flows," *Journal of Computational Physics*, vol. 229, no. 6, pp. 1970–1993, 2010.

[16] D. S. Balsara, "A two-dimensional HLLC Riemann solver for conservation laws: Application to Euler and magnetohydrodynamic flows," *Journal of Computational Physics*, vol. 231, no. 22, pp. 7476–7503, 2012.

[17] D. S. Balsara, "Multidimensional Riemann problem with self-similar internal structure. Part I–Application to hyperbolic conservation laws on structured meshes," *Journal of Computational Physics*, vol. 277, pp. 163–200, 2014.

[18] D. S. Balsara, "Three dimensional HLL Riemann solver for conservation laws on structured meshes; Application to Euler and magnetohydrodynamic flows," *Journal of Computational Physics*, vol. 295, pp. 1–23, 2015.

[19] D. S. Balsara, G. I. Montecinos, and E. F. Toro, "Exploring Various Flux Vector Splittings for the Magnetohydrodynamic System," *Journal of Computational Physics*, vol. 311, pp. 1–21, 2016.

[20] M. S. Liou and C. J. Steffen, "A new flux splitting scheme," *Journal of Computational Physics*, vol. 107, no. 1, pp. 23–39, 1993.

[21] G. C. Zha and E. Bilgen, "Numerical solutions of Euler equations by using a new flux vector splitting scheme," *International Journal for Numerical Methods in Fluids*, vol. 17, no. 2, pp. 115–144, 1993.

[22] D. W. Halt and R. K. Agarwal, "A novel algorithm for the solution of compressible Euler equations in wave/particle split (WPS) form," in *AIAA Computational Fluid Dynamics Conference, 11th, Orlando, FL*, p. 1993, 1993.

[23] A. Jameson, "Artificial diffusion, upwind biasing, limiters and their effect on accuracy and multigrid convergence in transonic and hypersonic flows," in *AIAA, Computational Fluid Dynamics Conference, 11th, Orlando, FL*, 1993.

[24] N. Balakrishnan and S. M. Deshpande, "New upwind method exploiting the wave-particle behaviour of fluid flow," *CFD Journal*, vol. 3, no. 4, pp. 433–446, 1995.

[25] R. K. Agarwal, J. Augustinus, and D. W. Halt, "A Comparative Study of Advection Upwind Split (AUSM) and Wave/Particle Split (WPS) Schemes for Fluid and MHD Flows," in *AIAA 30th Plasmadynamics and Lasers Conference. Norfolk, VA: AIAA Paper*, pp. 99–3613, 1999.

[26] S. H. Han, J. I. Lee, and K. H. Kim, "Accurate and robust pressure weight advection upstream splitting method for magnetohydrodynamics equations," *AIAA Journal*, vol. 47, no. 4, pp. 970–981, 2009.

[27] K. H. Kim, J. H. Lee, and O. H. Rho, "An improvement of AUSM schemes by introducing the pressure-based weight functions," *Computers & fluids*, vol. 27, no. 3, pp. 311–346, 1998.

[28] Y. Shen, G. Zha, and M. A. Huerta, "E-CUSP scheme for the equations of ideal magnetohydrodynamics with high order WENO scheme," *Journal of Computational Physics*, vol. 231, no. 19, pp. 6233–6247, 2012.

[29] A. Kurganov and E. Tadmor, "New High-Resolution Central Schemes for Nonlinear Conservation Laws and Convection–Diffusion Equations," *Journal of Computational Physics*, vol. 160, no. 1, pp. 241–282, 2000.

[30] A. Susanto, L. Ivan, H. De Sterck, and C. P. T. Groth, "High-order central ENO finite-volume scheme for ideal MHD," *Journal of Computational Physics*, vol. 250, pp. 141–164, 2013.

[31] S. Jaisankar and S. V. R. Rao, "A central Rankine–Hugoniot solver for hyperbolic conservation laws," *Journal of Computational Physics*, vol. 228, no. 3, pp. 770–798, 2009.

[32] J. U. Brackbill and D. Barnes, "The effect of nonzero $\nabla \cdot \mathbf{B}$ on the numerical solution of the magnetohydrodynamic equations," *Journal of Computational Physics*, vol. 35, no. 3, pp. 426–430, 1980.

[33] C. R. Evans and J. F. Hawley, "Simulation of magnetohydrodynamic flows-a constrained transport method," *The Astrophysical Journal*, vol. 332, pp. 659–677, 1988.

[34] K. G. Powell, "An approximate Riemann solver for magnetohydrodynamics (that works in more than one dimension)," *ICASE Report*, vol. 9424, 1994.

[35] A. Dedner, F. Kemm, D. Kröner, C.-D. Munz, T. Schnitzer, and M. Wesenberg, "Hyperbolic divergence cleaning for the MHD equations," *Journal of Computational Physics*, vol. 175, no. 2, pp. 645–673, 2002.

[36] A. J. Chorin, "A numerical method for solving incompressible viscous flow problems," *Journal of Computational Physics*, vol. 135, no. 2, pp. 118–125, 1997.

[37] J. U. Brackbill, "FLIP MHD: A particle-in-cell method for magnetohydrodynamics," *Journal of Computational Physics*, vol. 96, no. 1, pp. 163–192, 1991.

[38] F. Jiang, M. S. A. Oliveira, and A. C. M. Sousa, "SPH simulation of transition to turbulence for planar shear flow subjected to a streamwise magnetic field," *Journal of Computational Physics*, vol. 217, no. 2, pp. 485–501, 2006.

[39] S. L. L. Verardi, J. M. Machado, and Y. Shiyou, "The application of interpolating MLS approximations to the analysis of MHD flows," *Finite Elements in Analysis and Design*, vol. 39, no. 12, pp. 1173–1187, 2003.

[40] R. Bhargava and S. Singh, "Numerical simulation of unsteady MHD flow and heat transfer of a second grade fluid with viscous dissipation and Joule heating using meshfree approach," *World Academy of Science, Eng. and Tech*, vol. 67, pp. 1043–1049, 2012.

[41] G. C. Bourantas, E. D. Skouras, V. C. Loukopoulos, and G. C. Nikiforidis, "An accurate, stable and efficient domain-type meshless method for the solution of MHD flow problems," *Journal of Computational Physics*, vol. 228, no. 21, pp. 8135–8160, 2009.

[42] M. Dehghan and D. Mirzaei, "Meshless local boundary integral equation (LBIE) method for the unsteady magnetohydrodynamic (MHD) flow in rectangular and circular pipes," *Computer Physics Communications*, vol. 180, no. 9, pp. 1458–1466, 2009.

[43] M. Dehghan and D. Mirzaei, "Meshless local Petrov–Galerkin (MLPG) method for the unsteady magnetohydrodynamic (MHD) flow through pipe with arbitrary wall conductivity," *Applied Numerical Mathematics*, vol. 59, no. 5, pp. 1043–1058, 2009.

[44] M. Dehghan and R. Salehi, "A meshfree weak-strong (MWS) form method for the unsteady magnetohydrodynamic (MHD) flow in pipe with arbitrary wall conductivity," *Computational Mechanics*, vol. 52, no. 6, pp. 1445–1462, 2013.

[45] E. Kwan-yu Chiu, Q. Wang, R. Hu, and A. Jameson, "A conservative mesh-free scheme and generalized framework for conservation laws," *SIAM Journal on Scientific Computing*, vol. 34, no. 6, pp. A2896–A2916, 2012.

[46] P. Suchde, J. Kuhnert, S. Schröder, and A. Klar, "A flux conserving meshfree method for conservation laws," *International Journal for Numerical Methods in Engineering*, 2017.

[47] J. M. Stone and M. L. Norman, "ZEUS-2D: A radiation magnetohydrodynamics code for astrophysical flows in two space dimensions. I-The hydrodynamic algorithms and tests.," *The Astrophysical Journal Supplement Series*, vol. 80, pp. 753–790, 1992.

[48] J. M. Stone, D. Mihalas, and M. L. Norman, "ZEUS-2D: A radiation magnetohydrodynamics code for astrophysical flows in two space dimensions. III-The radiation hydrodynamic algorithms and tests," *The Astrophysical Journal Supplement Series*, vol. 80, pp. 819–845, 1992.

[49] J. M. Stone, T. A. Gardiner, P. Teuben, J. F. Hawley, and J. B. Simon, "Athena: a new code for astrophysical MHD," *The Astrophysical Journal Supplement Series*, vol. 178, no. 1, p. 137, 2008.

[50] D. S. Balsara and C.-W. Shu, "Monotonicity preserving weighted essentially non-oscillatory schemes with increasingly high order of accuracy," *Journal of Computational Physics*, vol. 160, no. 2, pp. 405–452, 2000.

[51] A. Lani, T. Quintino, D. Kimpe, H. Deconinck, S. Vandewalle, and S. Poedts, "The COOLFluiD framework: design solutions for high performance object oriented scientific computing software," in *International Conference on Computational Science*, pp. 279–286, Springer, 2005.

[52] D. Kimpe, A. Lani, T. Quintino, S. Poedts, and S. Vandewalle, "The COOLFluiD parallel architecture," *Lecture notes in computer science*, vol. 3666, p. 520, 2005.

[53] G. Tóth, "A general code for modeling MHD flows on parallel computers: Versatile advection code," *Astrophysical Letters and Communications*, vol. 34, p. 245, 1996.

[54] K. G. Powell, P. L. Roe, T. J. Linde, T. I. Gombosi, and D. L. De Zeeuw, "A solution-adaptive upwind scheme for ideal magnetohydrodynamics," *Journal of Computational Physics*, vol. 154, no. 2, pp. 284–309, 1999.

[55] U. Ziegler, "A central-constrained transport scheme for ideal magnetohydrodynamics," *Journal of Computational Physics*, vol. 196, no. 2, pp. 393–416, 2004.

[56] R. Balasubramanian and K. Anandhanarayanan, "Compressible Euler/Reynolds Averaged Navier-Stokes Solver," *DRDO Science Spectrum*, pp. 219–226, March 2009.

[57] R. Balasubramanian and K. Anandhanarayanan, "Viscous computations for complex flight vehicles using CERANS with wall function," *Computational Fluid Dynamics Journal*, vol. 16, no. 4, p. 386, 2008.

[58] R. Balasubramanian, K. Anandhanarayanan, R. Krishnamurthy, and D. Chakraborty, "Mitigation of shock-induced flow separation using magnetohydrodynamic flow control," *Sādhanā*, vol. 42, no. 3, pp. 379–390, 2017.

[59] R. Balasubramanian, K. Anandhanarayanan, R. Krishnamurthy, and D. Chakraborty, "Magnetohydrodynamic flow control of hypersonic blunt body flowfield involving real gas effects," in *C.F.D. Symposium 2016, Banglore, India*, p. 80, 2016.

[60] A. Jeffrey and T. Taniuti, *Non-Linear Wave Propagation With Applications to Physics and Magnetohydrodynamics*, vol. 9. Elsevier, 2000.

[61] H. De Sterck, B. Low, and S. Poedts, "Complex magnetohydrodynamic bow shock topology in field-aligned low-β flow around a perfectly conducting cylinder," *Physics of Plasmas*, vol. 5, no. 11, pp. 4015–4027, 1998.

[62] J. P. Freidberg, *Ideal magnetohydrodynamics*. Plenum Press, New York, NY, 1987.

[63] K. Yee, "Numerical solution of initial boundary value problems involving Maxwell's equations in isotropic media," *IEEE Transactions on Antennas and Propagation*, vol. 14, no. 3, pp. 302–307, 1966.

[64] S. Brecht, J. Lyon, J. Fedder, and K. Hain, "A simulation study of east-west imf effects on the magnetosphere," *Geophysical Research Letters*, vol. 8, no. 4, pp. 397–400, 1981.

[65] C. R. DeVore, "Flux-corrected transport techniques for multidimensional compressible magnetohydrodynamics," *Journal of Computational Physics*, vol. 92, no. 1, pp. 142–160, 1991.

[66] D. S. Balsara, "Second-order-accurate schemes for magnetohydrodynamics with divergence-free reconstruction," *The Astrophysical Journal Supplement Series*, vol. 151, no. 1, p. 149, 2004.

[67] J. A. Rossmanith, "An unstaggered, high-resolution constrained transport method for magnetohydrodynamic flows," *SIAM Journal on Scientific Computing*, vol. 28, no. 5, pp. 1766–1797, 2006.

[68] P. Janhunen, "A positive conservative method for magnetohydrodynamics based on HLL and Roe methods," *Journal of Computational Physics*, vol. 160, no. 2, pp. 649–661, 2000.

[69] A. Jameson, W. Schmidt, and E. Turkel, "Numerical solutions of the Euler equations by finite volume methods using Runge–Kutta time-stepping schemes," *AIAA Paper*, vol. 1259, 1981.

[70] J. C. Mandal and J. Subramanian, "On the link between weighted least-squares and limiters used in higher-order reconstructions for finite volume computations of hyperbolic equations," *Applied Numerical Mathematics*, vol. 58, no. 5, pp. 705–725, 2008.

[71] S. Jaisankar and S. V. R. Rao, "Diffusion regulation for Euler solvers," *Journal of Computational Physics*, vol. 221, no. 2, pp. 577–599, 2007.

[72] G. A. Sod, "A survey of several finite difference methods for systems of nonlinear hyperbolic conservation laws," *Journal of Computational Physics*, vol. 27, no. 1, pp. 1–31, 1978.

[73] K. Waagan, "A positive MUSCL-Hancock scheme for ideal magnetohydrodynamics," *Journal of Computational Physics*, vol. 228, no. 23, pp. 8609–8626, 2009.

[74] P. Havlík and R. Liska, "Comparison of Several Finite Difference Methods for Magnetohydrodynamics in 1D and 2D," *Hyperbolic Problems: Theory, Numerics, Applications*, pp. 585–592, 2008.

[75] M. Aftosmis, D. Gaitonde, and T. S. Tavares, "Behavior of linear reconstruction techniques on unstructured meshes," *AIAA Journal*, vol. 33, no. 11, pp. 2038–2049, 1995.

[76] F. Bouchut, C. Klingenberg, and K. Waagan, "A multiwave approximate Riemann solver for ideal MHD based on relaxation II: numerical implementation with 3 and 5 waves," *Numerische Mathematik*, vol. 115, no. 4, pp. 647–679, 2010.

[77] W. R. Inc., "Mathematica, Version 10.0." Champaign, IL, 2014.

[78] T. J. Barth and P. O. Frederickson, "Higher order solution of the euler equations on unstructured grids using quadratic reconstruction," *AIAA Paper*, vol. 90, p. 0013, 1990.

[79] T. J. Barth, *Numerical aspects of computing viscous high Reynolds number flows on unstructured meshes*. American Institute of Aeronautics and Astronautics, 1991.

[80] S. A. Orszag and C.-M. Tang, "Small-scale structure of two-dimensional magnetohydrodynamic turbulence," *Journal of Fluid Mechanics*, vol. 90, no. 01, pp. 129–143, 1979.

[81] J. M. Picone and R. B. Dahlburg, "Evolution of the orszag–tang vortex system in a compressible medium. ii. supersonic flow," *Physics of Fluids B: Plasma Physics*, vol. 3, no. 1, pp. 29–44, 1991.

[82] G. Tóth, "The $\nabla \cdot \mathbf{B} = \mathbf{0}$ constraint in shock-capturing magnetohydrodynamics codes," *Journal of Computational Physics*, vol. 161, no. 2, pp. 605–652, 2000.

[83] A. L. Zachary, A. Malagoli, and P. Colella, "A higher-order godunov method for multidimensional ideal magnetohydrodynamics," *SIAM Journal on Scientific Computing*, vol. 15, no. 2, pp. 263–284, 1994.

[84] D. S. Balsara and D. S. Spicer, "A staggered mesh algorithm using high order godunov fluxes to ensure solenoidal magnetic fields in magnetohydrodynamic simulations," *Journal of Computational Physics*, vol. 149, no. 2, pp. 270–292, 1999.

[85] M. S. Yalim, *An Artificial Compressibility Analogy Approach for Compressible Ideal MHD*. PhD thesis, The von Karman Institute for Fluid Dynamics, 2008.

[86] D. Sridar and N. Balakrishnan, "An upwind finite difference scheme for meshless solvers," *Journal of Computational Physics*, vol. 189, no. 1, pp. 1–29, 2003.

[87] A. K. Ghosh, *Robust Least Squares Kinetic Upwind Method For Inviscid Compressible Flows*. PhD thesis, Department of Aerospace Engineering, Indian Institute of Science, 1996.

List of publications

Journals:

1. Kalpajyoti Borah, Ganesh Natarajan and Anoop K. Dass, "A novel second-order flux splitting for ideal magnetohydrodynamics," *Journal of Computational Physics*, vol. 313, pp. 159-180, 2016.

2. Kalpajyoti Borah, Ganesh Natarajan and Anoop K. Dass, "Investigation of discrete conservation of least-squares meshfree framework for ideal magnetohydrodynamics," Communicated to *Computers & Fluids*.

3. Kalpajyoti Borah, Ganesh Natarajan and Anoop K. Dass, "Extending Magneto-acoustic Wave Particle Splitting (MWPS) scheme for two-dimensional simulations of ideal magnetohydrodynamics flows," Manuscript under preparation.

Book Chapter:

1. Kalpajyoti Borah, Ganesh Natarajan and Anoop K. Dass, "A meshfree framework for ideal magnetohydrodynamics," *Fluid Mechanics and Fluid Power-Contemporary Research, Lecture Notes in Mechanical Engineering*, ISBN: 978-81-322-2741-4, pp. 1595-1605, 2017.

Conferences:

1. Kalpajyoti Borah, Ganesh Natarajan and Anoop K. Dass, "A meshfree framework for ideal magnetohydrodynamics," *5^{th} International and 41^{st} National Conference on Fluid Mechanics and Fluid Power (FMFP 2014)*, IIT Kanpur, India, December 12–14, 2014.

2. Kalpajyoti Borah, Ganesh Natarajan and Anoop K. Dass, "A conservative meshfree framework for one-dimensional ideal magnetohydrodynamics," *17^{th} Annual CFD Symposium*, NAL Bangalore, India, August 11–12, 2015.

3. Kalpajyoti Borah, Ganesh Natarajan and Anoop K. Dass, "Optimally-dissipative wave-particle splitting scheme for ideal magnetohydrodynamics," *XXVII IUPAP Conference on Computational Physics*, IIT Guwahati, India, December 2–5, 2015.